Electronic properties and microstructure of nanoparticulate silicon systems for diode applications

Ulrich P. Männl

Thesis presented for the degree of

DOCTOR OF PHILOSOPHY

In the Department of Physics

Faculty of Science

UNIVERSITY OF CAPE TOWN

October 2014

To raise new questions, new possibilities, to regard old problems from a new angle, requires creative imagination and marks real advances in science.

-A. Einstein

Contents

Abstract

In printed electronics the use of semiconducting silicon nanoparticles allows more than the simple printing of conductive materials. It gives the possibility of fabricating robust and inexpensive, active components. This work presents the design, fabrication, and characterization of Schottky barrier diodes using silicon nanoparticulate composites. Within this work it could be shown, that silicon nanoparticles produced by high energy milling can be used to replace the pigment in water-based graphic inks, which on curing have unique semiconducting properties, arising from the transport of charge through a percolation network of crystalline silicon nanoparticles. In this thesis scanning electron microscopy (SEM), high-resolution transmission electron microscopy (HRTEM), Raman spectroscopy, and mid-infrared scanning near-field optical microscopy (IR s-SNOM) were employed to investigate the micro-scale as well as the meso-scale structure of the printed particle networks and, more importantly the structure of the interface between particles. A close contact between lattice planes of different particles was observed, without the presence of a thick intervening oxide layer.

Altogether, the results presented in this thesis suggest that highly doped silicon nanoparticles produced by high energy milling are suitable to be used for Schottky barrier diodes fabricated by screen printing. The saturation current of the diodes was about $0.11\mu A$ for reverse bias voltages up to $5V$ with an ideality factor of 10.6, and rectification ratios of approximately 10^4 were observed.

1 Introduction

Over the last three decades printed electronics has arisen as a new sector in the electronics landscape. The great interest in developing new electronics applications is driving research and development in this area, from the investigation of new materials, development of new devices to the incorporation of these devices into functional applications. To achieve these demands, it is necessary to replace traditional electronics in existing products [1–3]. Modern microelectronic devices with fast switching times and high processor capabilities fulfill the required interconnect bandwidth [4] to achieve energy efficiency, integration density, and information throughput in high-performance computing systems [5]. However, this technology does not meet the new requirements for electronics to be more lightweight, transparent and even mechanical flexibility which is required for modern, everyday electronic devices [6].
The application of printing as a fully additive process, in which the material giving functionality is deposited in the correct pattern on a substrate is not a new concept in electronics fabrication. Already in 1903 Hanson introduced printing of conductive metal patterns on insulating substrates [7] which was followed by the development of the ubiquitous printed circuit board (PCB) [8]. Modern conductive inks are mainly based on silver and other metal flake, but newer developments include also silver and copper nanoparticles [9, 10] as well as graphene [11–13] and carbon nanotubes [14]. In addition to the high conductivity of these printed conductors, they allow the production of transparent electronics as well [15, 16].
To realize fully printed electronics, besides resistors and capacitors, devices like transistors and diodes also need to be printed, which in turn requires a printable semiconductor. The integration of novel semiconducting materials into devices has been challenging, but developments in transfer printing and solution-based printing now allow these materials to be incorporated into large-area electronics [17–19].

Crucial for the development of active printed layers are new materials like printed organic semiconductors [1, 20–22], metal oxide semiconductors such as ZnO [23, 24], ITO [25, 26], graphene [27] and reduced graphene oxide thin films which are used as flexible and transparent applications [19, 27]. Today screen printing is also used for organic electronic devices based on π-conjugated polymers [28] and organic-based solar cells [29].

In printed electronics the use of effectively the most significant semiconductor material silicon is also desirable, since it is available in great amounts and available in high purity [30]. Recent developments have shown the possibility of using a solution-processed silicon precursors to produce thin film transistors by ink-jet printing of cyclopentasilane [31]. However, unlike nanoparticle based inks this approach has the disadvantage that it needs thermal post-processing up to $800°C$. In addition the electrical properties of surface functionalized silicon nanoparticles are studied intensively. So far, the application of these nanoparticles has achieved only a small advance and such stabilizing molecules need to be further modified in a desired way for specific purposes, which are defined by the respective applications, e.g., in optoelectronics or in sensor elements [30].

The utilization of nanoparticles in functional inks is closely linked to the study of binders and solvents in order to achieve printable properties. It has been shown that the use of ethyl cellulose as an organic binder is crucial for the performance of ZnO films [32] and TiO_2 paste [33] used in dye-sensitized photovoltaic cells. The material combination presented in this work, inks with nanoparticles using the two most promising binder materials, soluble cellulose based polymers and an acrylic screen printing base [35, 36], opens new avenues for printing onto a large variety of substrates. Designed for a fully screen printable process without any post-processing steps, the materials are suitable for devices such as field effect transistors [37, 38] and large area negative temperature coefficient thermistors [39]. Furthermore these inks allow printing on paper substrates which are considered as potential substrates for the development of low-cost flexible electronics [40].

Besides transistors, diodes are a crucial component in printed electronics. Modern Schottky barrier and heterojunction theory can be applied to the assessment of

wide band gap oxide semi-conductor interfaces as contacts and rectifiers [41]. This was recently reviewed from a charge transfer, energy band diagram perspective [41], which could be realized using indium tin oxide [42]. Recent developments have also shown the ability to produce silicon Schottky diodes on flexible substrates by the transfer method [43].

To date, the successful production of high quality diodes by direct screen printing of silicon nanoparticles has not been reported. This thesis mainly focuses on characterising and producing silicon nanoparticle based, fully printed diodes on flexible and low-temperature substrates using screen printing. Furthermore, silicon nanoparticles and layers of printed silicon nanoparticles are investigated with the binder influencing the properties of the device, as well as the use of other material systems necessary to form a diode heterostructure. Chapter 2 briefly introduces screen printing and also touches on silicon nanoparticles. A review of p-n junctions and Schottky diodes is given at the end of this chapter. Experimental methods used to fabricate the diodes, starting from production of the silicon nanoparticles, preparing functional inks and printing these inks with the desired structures will be discussed in detail in chapter chapter 3. Furthermore the experimental methods used to investigate the micro and nanostructure of the printed layers will be given here. The research findings and discussion of the morphology and microstructure of silicon nanoparticles will be presented in chapter 4, followed by the presentation of the results obtained by investigating the printed silicon layers in chapter chapter 5. The analysis of the research findings concerning the fully printed diodes is elucidated in chapter 6, and the pertinent conclusions stated in chapter 7.

2 Background

This chapter reviews the theoretical background for this thesis. Firstly, printed electronics will be introduced as a new area in the electronics landscape. A brief description of silicon and nanoparticles will follow. At the end of this chapter the theory of both the p-n junction and metal-semiconductor junctions will be given in detail.

2.1 Printed electronics

Over the last few decades a highly innovative fusion of three technological areas - microelectronics, chemistry and printing - led to the development of printed electronics as a newly established research area [9] in the electronics landscape. The high interest in developing electronic circuitry that is more lightweight, mechanically more robust and even flexible is driving research in this area. To achieve certain demands, in for example displays of mobile appliances, it is necessary to replace traditional electronics in existing products [1]. Although well established, high integration microelectronics fabrication can support electronic devices with gate-lenth scaling down to less then 20nm, in order to enhance their performance by reducing contact and series resistance [45, 82] it is, for example, not able to address the demands on flexibility or large areas. Novel materials on the nanoscale, which are solution processable, open intriguing capabilities for developments in these areas [46].

A major milestone for circuitry was the production of conductive metal patterns on dielectric substrates introduced by Hanson in 1903 [7], which was followed by a large variety of methods for producing printed circuits such as chemical or physical

vapor-deposition [8]. This development preceded printed electronics in introducing into the already existing high integration of microelectronics and display technology, processes and materials which make electronic devices more lightweight, robust and mechanically flexible [6]. Nowadays polymer thick film (PTF) screen printing is an easy and low cost method of producing electrical circuitry [47].

The use of conducting and semiconducting nanoparticles in functional printing inks for circuitry is motivated by the fact that nanoparticles already have all the required electrical and optical properties, and can be used as simple building blocks to form complex structures at a small scale [48, 49]. An example of this development is the production of printed antennas that can be used for radio-frequency identification (RFID), wireless local area networks (WLAN) [50] and even wireless sensor networks [51]. Graphite inks are occasionally used as a low cost alternative to silver, but their higher resistivity makes them more suitable for printing resistors. However newer forms of carbon, such as nanotubes [14] and graphene [42] are being explored for production of both conducting tracks and coatings, especially in applications where a high transparency is required [52].

The realisation of fully printed electronic solutions also requires printable semiconductors to form basic electronic components: e.g. diodes and transistors. In this context early successes were achieved with hole conducting polymer semiconductors [53]. In 2000 this development was honoured by the fact that the Nobel Prize was jointly awarded to Alan J. Heeger, Alan G. MacDiarmid and Hideki Shirakawa *for the discovery and development of conductive polymers*. Recently, electron conducting polymer materials which can be printed have been developed [54], thus overcoming both the challenge of making insoluble semiconducting polymers and oligomers printable by functionalising the molecules, and of achieving sufficiently high mobilities of the charge carriers [55, 56]. On the other hand, the use of nanoparticles in functional printing inks is a new trend, for example, printing of semiconducting metal oxide nanoparticles containing inks shows promising results [32, 33]. However, not only the characteristics of the particles but the other components in the ink, like the binder and solvent, as well as the deposition process and the substrate influence the behaviour of the printed layer [57]. There are two contrary requirements for ink

applied in screen printing. One is that the ink should flow to remove mesh marks and surface imperfections. On the other hand, ink should not flow excessively since this leads to expansion of the width of lines [34].
Silicon's dominance in conventional electronics stems not only from its semiconducting properties but also from its band gap of about 1.1 eV, which is more favourable than the high band gaps of most oxide semiconductors, because it allows thermal excitation of charge carriers without saturation, making the material a good semiconductor at ambient temperatures. The band gap is also in the range of the separation of most atomic energy levels, allowing a good coupling of either the conduction band or valence band to most metals for contacts. In addition the energy quantum of visible light is in the same range allowing its use in photovoltaic applications and light sensing. It is therefore an intriguing challenge of printed electronics to print semiconducting materials at ambient temperatures on flexible substrates using silicon nanoparticles. Various printing techniques are available for use in printed electronics which are mainly divided in roll-to-roll and sheet based approaches, which includes screen printing, inkjet printing, stamping, transfer printing or nanoimprinting and gravure printing [58]. Only screen printing with nanoparticle based inks will further be described in detail because these form the basis for the diodes, which are discussed in this work.

2.2 Silicon nanoparticles and silicon inks

2.2.1 Silicon

By mass silicon (from Latin: silex, hard stone or flint) is the eighth most common element in the universe. It rarely occurs as a pure free element in nature but is widely distributed as silicates or silicon dioxide (silica) in the earth´s crust [59, 60]. Silicon is a group four element and hence tetravalent. The valence electrons form a covalent bond with the neighbouring atoms, meaning that electron pairs are shared between them as shown in Fig. 2.1(a). Silicon crystallizes in a face-centered cubic bravais lattice with a basis of two atoms at $\{(0,0,0),(1/4,1/4,1/4)\}$ as shown in Fig.

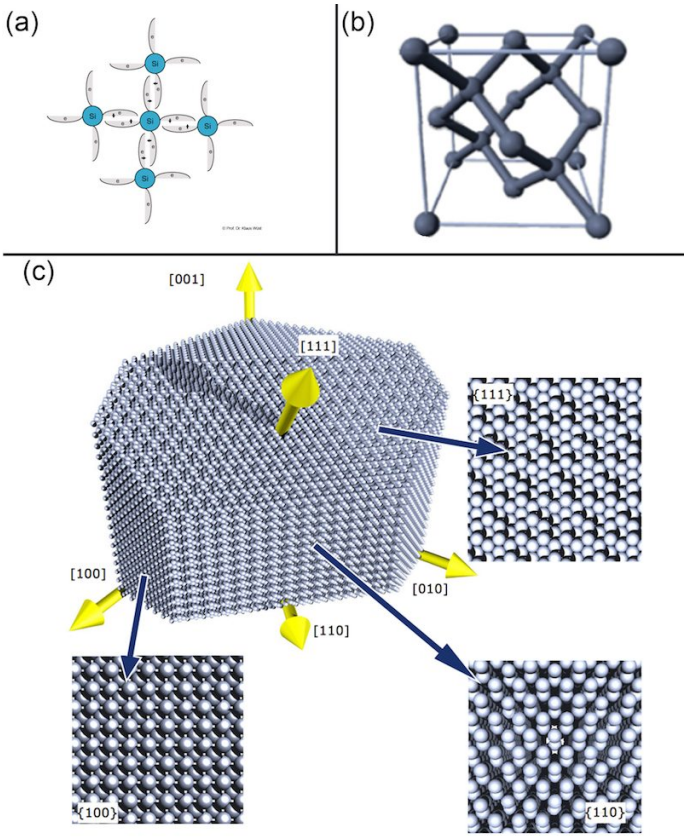

Figure 2.1: *Two dimensional representation of the diamond cubic crystal structure. Silicon has four valence electron who participate in the formation of a chemical bond [61].* ***b*** *Silicon crystallizes in a diamond cubic crystal structure [62],* ***(c)*** *the crystal structure of silicon with the high stability of the <111>-surfaces allows the realisation of conducting silicon nanoparticles [63]*

2.1(b). Due to silicon's crystal structure, the <111> -surface is the lowest energy surface [64] and therefore has the highest stability (i.e. it is the preferred cleavage plane [64], see Fig. 2.1(c)), which is used within this work to produce stable and electrical active, oxygen terminated silicon nanoparticle surfaces.

For large scale production, silicon dioxide (SiO_2) is conventionally reduced to metallurgical grade silicon by a carbothermal reduction ($SiO_2 + 2C \rightarrow Si + 2CO$), in which the oxygen is removed by a heterogeneous–homogeneous reaction sequence [65, 66]. The production of electronic grade silicon from metallurgical grade qualities needs a reduction of impurities by at least 5 orders of magnitude, hence further refinement is achieved by different chemical and physical processes such as the NEDO (New Energy and Industrial Technology Development Organization) melt-purification pro-

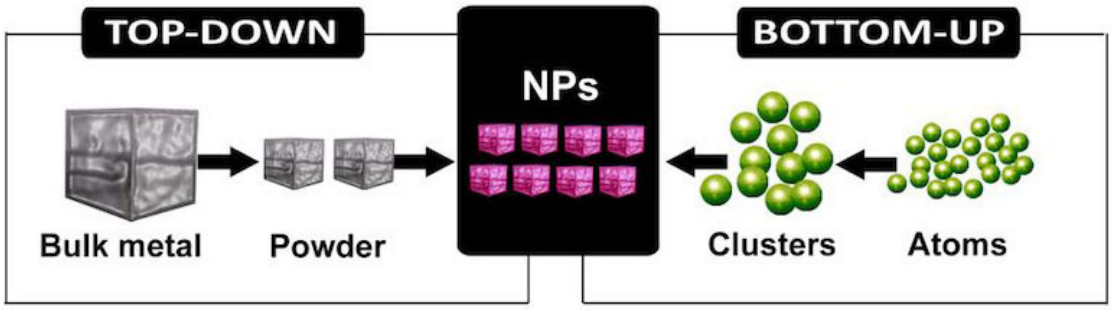

Figure 2.2: *Scheme of Top-Down and Bottom-Up approaches to the synthesis of nanoparticles (NP´s) [68].*

cess [65, 67]. According to the production process and purity, silicon is classified in different purities. The least pure is Si_{mg} (metallurgical grade, 98–99%), followed by Si_{sg} (solar grade, <0.01% impurity) and Si_{eg} (electronic grade, impurities less than 1 ppb).

2.2.2 Silicon nanoparticles

Two distinct strategies, often referred to as 'bottom-up' and 'top-down' fabrication (schematically shown in Fig. 2.2), have been used to create structures with nanometre (i.e., 1-100nm) sizes [68]. In the former, nanoscale materials are assembled from smaller molecular and atomic components. Here, nano-structured materials can be synthesized or designed layer by layer [69]. Different routes are now available for the preparation of silicon nanoparticles using bottom up processes. Primary particles with a size in the order of 10nm can be produced in liquid phase by the precipitation of nanoparticles from a solution as a result of a reaction or decomposition from a liquid silane based precursor [31, 70]. Passivation of the resulting nanoparticle, using hydrogen and alkyl groups, is necessary to curb recrystallisation and agglomeration [71, 72]. Using this technique, clean, passivated crystalline nanoparticles and nanowires were produced by Korgel et al. [70, 73, 74]. These particles had an average diameter of 10nm and 39.3nm respectively with a thick capping layer [73, 74]. Kauzlarich et al. [75] showed the production of nanometre-sized silicon particles

by ultrasonic dispersion of thin sections of porous silicon (PS) in organic solvents. The larger aggregates ranged in size from 20 to 50nm and were made up of smaller crystallites with diameters of 2-10nm. Monodisperse crystallites ranged in size from 2-10nm. All the particles had a surface layer of amorphous SiO_2 [75]. The main problem of the liquid phase methods described here is that there is only little control over the size distribution and surface modification of the nanoparticles.

Bottom-up processes that rely on the pyrolysis of silane by an energy source such as a laser or plasma are alternatives which are more size selective. This approach provides the possibility of producing amorphous, poly- or even single crystalline silicon nanoparticles with variable doping levels [76, 77, 79]. Different energy sources can be used for the decomposition of a gaseous precursor [77, 78]. The energy will induce chemical reactions in the gas phase resulting in gas phase nucleation of particles [77, 78]. To produce silicon nanoparticles with a diameter around 10 nm or less, hot wire chemical vapour synthesis (HWCVS) can be used. Scriba et al. [79] recently produced doped, electrical active silicon nanoparticles by HWCVS using a mixture of monosilane and diborane or phosphine. The particles produced were monocrystalline with an average diameter of 22nm, with shapes ranging from a perfect octahedron to those with varying degrees of truncation of this basic shape [79].

In contrast, top-down methods involve simple methods of breaking down bulk materials into nanoparticles, for example by milling [80]. For the production of silicon nanoparticles by (the top-down process) chemical etching can also be utilized as well. Recently Swihart et al. [81] presented that Si-rich suboxide particles can be employed as a starting material for Si nanoparticles. This method employs an etching process, combining HF/HNO_3 or HF/H_2O_2 with sonication to remove the oxide and to reduce the size of the particles. Using this method silicon nanoparticles with the average diameters of 1.9-2.4 nm could be produced [81]. After prolonged ultrasonication in water, the Si nanoparticles showed strong blue photoluminescence [81, 82]. Metal assisted chemical etching (MacEtch) is a recently developed anisotropic wet etching method that is capable of producing high aspect ratio semiconductor nanostructures from patterned metal film [83, 84]. Hadjersi et al. [85] used MacEtch using $K_2Cr_2O_7$ as an oxidizing agent to produce photoluminescent porous silicon layers on highly

resistive p-type silicon. They showed that for an etching time of 30 seconds the surface of the silicon is dominated by a high density of channels (macropores) of about 100nm diameter that penetrate into the bulk of the silicon [85]. Silicon nanoparticles can also be produced by ablation of bulk material using a spark discharge [86]. Here a high voltage gas break-down is repeatedly induced between two electrodes of the desired material. Usually, the energy stored in a capacitor is released into the discharge very rapidly, resulting in very high temperatures (typically 20,000 K) [86–89]. Interaction of the high temperature plasma with the electrode surfaces results in evaporation of the electrode material. As the discharge dies out, the vapour cloud cools very rapidly, first through adiabatic expansion and radiation and then by thermal conduction. The extremely high cooling rates result in a high concentration of very small particles of rather narrow size distribution [87–89]. Vons et al. [87–89] showed that pure and oxidised uniformly sized, crystalline silicon nanoparticles with a primary particle diameter of 3–5 nm can be produced.

Laser ablation is another top-down method for the production of silicon nanoparticles. With this technique irradiates a target which is immersed in a liquid such as water, hexane, toluene or inert gas [90, 91]. The bulk material will evaporate or sublimate into nanoparticles which will then be dispersed in the fluid. Umezu et al. [90] used pulsed laser ablation in a silicon target placed in liquid environment to yield a colloid of silicon nano-crystallites. The primary particles averaged 3nm, and the aggregate particles had diameters of the order of 10nm. Yoshida et al. [91] reported nanometer sized silicon crystallites prepared by excimer laserablation in a constant pressure inert gas atmosphere. The size of the particles was about 3nm and the size distribution of the Si particles depended on the pressure of the inert gas.

Mechanical milling is a process which is routinely used in powder metallurgy and in the mineral processing industry [92]. Silicon as a brittle feedstock is fractured and attrited progressively resulting in nanometre sized, polydispersed particles with a disperse log normal size distribution and a size about 80nm can be achieved [35, 37, 80, 92, 94]. The microstructure, morphology, size distribution, and level of contamination of the resulting nanoparticles are related to the choice of mill and its process variables. The main concern in the case of silicon nanoparticles intended for electronic applications

is the oxidation of the particles used. Härting et al. [35–39, 93, 95] managed to produce silicon nanoparticles which are not necessarily free of oxygen, but contain a disordered monolayer of silicon sub-oxide which permits charge transport.

2.2.3 Silicon inks

In order to produce high performance devices using silicon as semiconductor, it is inevitable that the materials utilized form a continuous silicon layer, which allows charge transport throughout the layer. Traditionally this is achieved by direct deposition of a compact layer, for example by chemical vapour deposition. Mueller et al. [98] first grew silicon films in 1964 by the pyrolytic decomposition of SiH_4 (silane) and H_2 mixtures on single crystal sapphire at temperatures of 1050°C to 1200°C. The silicon film produced showed a mobility of 135cm^2/Vs [98].
In a similar approach, cyclopentasilane is a known compound that is liquid at ambient temperatures and can be pyrolised to form silicon films with useful electrical properties [104]. Other printable precursors can be produced by the controlled polymerization of hydrosilanes compound as well as alkyl- and arylsilanes to produce soluble silicon polymers [101, 102]. After spin coating or printing the ink (optionally with simultaneous or immediately subsequent UV irradiation) and forming an oligo- and/or polysilane film, curing the ink formed an amorphous, hydrogenated silicon film [101–103]. The curing step generally comprises heating the printed ink or layer to a temperature of at least about 200°C [101]. Amir Mashkoori (CEO and chairman of Kovio) reported a mobility of 80 cm^2/Vs of the silicon films produced [102]. Shimoda et al. [104] demonstrated the solution processing of a silicon thin-film using a liquid silane-based precursor. Using liquid cyclopentasilane (Si_5H_{10}), polycrystalline silicon (poly-Si) films were prepared by both spin-coating and ink-jet printing. The films had mobilities of 108 cm^2/Vs [104]. Another method for printing silicon using a solution processable silicon precursor was reported by Brotherton et al. [105]. However, high mobilities were only reported after laser crystallization.
Silicon films can also be produced by the deposition of silicon nanomaterials, including nanoparticles and nanowires. Most research has focused on the quality of

the base material, with very few approaches leading to what can be described as a printable ink. For example Garnett et al. [99] developed a chemical vapor deposition (CVD) synthesis based process to grow high-quality single-crystalline, size-controlled, epitaxial silicon nanowires (Si NW) with average diameters of about 11.3 nm from silicon wafers, from various sized Pt catalysts. For the production of the Si NWs a Pt nanoparticle solution was drop-cast on the silicon surface and after 20s it was rinsed with isopropy alcohol. Si NWs were grown in an atmospheric pressure CVD system for 2–30 min where the carrier gas (10% H2/Ar) bubbled through liquid silicon tetrachloride ($SiCl_4$). For boron doped Si NWs, Boron trichloride (BCl_3) gas was used. The nanowires were sonicated off the substrate, drop-cast onto a chip containing prepatterned metal electrodes and connected via standard electron-beam lithography. The mobility of the reported silicon film was 28 cm^2/Vs [99].
Rogers et al. [96] also presented a silicon film with good electrical properties (mobilities of about 190 cm^2/Vs) using silicon ribbons in thin film type transistors formed on plastic substrates [96]. This process uses etched trenches with controlled rippled structures defined on the sidewalls, together with angled evaporation of masking materials and anisotropic wet etching of the silicon, to produce multilayer stacks of ribbons with uniform thicknesses and lithographically defined lengths and widths. Ribbons with thicknesses between tens and hundreds of nanometers and lengths of up to several centimeters, could be produced. A transfer printing process, using a soft rubber stamp enabled the layer by layer transfer of organized arrays of such ribbons to form devices [96, 97].
Scott Ferguson (NanoGram Vice President) has announced the successful fabrication of a silicon thin film with a carrier mobility of 2.0 cm^2/Vs using a printable ink containing silicon nanoparticles (produced by a laser pyrolysis based process) which was deposited by laser reactive deposition [106].
Generally therefore, the production of these silicon films from nanostructured materials is technically very complex, but Härting and Britton et al. [37, 109] developed a screen printable ink using silicon nanoparticles with an average diameter of about 80nm, produced by high energy milling. Silicon films and devices produced by screen printing using these materials do not need any post processing steps such as sintering

and showed mobilities up to 100 cm^2/Vs [37, 109]. This is the ink which was used in this study.

2.3 Diodes

Diodes are part of the group of non-linear electronic devices. In this case non-linear means, that the current through the diode is a non-linear function of the voltage applied (i.e. $c \cdot I(V) \neq I(c \cdot V)$). Furthermore diodes have low resistance (ideally zero) for forward bias and very high (ideally infinite) resistance for reverse bias. Because of their asymmetric conductance, diodes are mainly used for rectifying and switching in electronic circuitry [111]. The main type of diodes are the following:

- p-n junction diodes
- Schottky diodes
- Zener diodes
- Esaki- or Tunnel diodes
- Light-emitting diodes
- Photodiodes

Since this project mainly focuses on the production and characterisation of Schottky diodes, in this chapter only p-n junction and Schottky diodes will be discussed briefly, whereas p-n junction diodes will be discussed in comparison with the Schottky diodes. The functioning of other types of diodes is based on the same physical laws, but they are made from other materials, doping levels etcetera, therefore they can be considered as a special case which will not be discussed.

2.3.1 p-n junction diodes

Only few electronic components, e.g. varistors and thermistors, can be constructed from homogenous semiconductors. For most devices a difference in material properties is needed. The simplest electrical component in terms of structure is a semiconductor diode, made of a p-n junction. The main feature of a p-n junction is the interface between an n-type and a p-type semiconductor forming the junction [112], as seen in Fig. 2.3. At the left-hand side of Fig. 2.3 the p-type semiconductor is doped with electron acceptors, and the right-hand side of the junction is n-type doped with electron donors. Directly at the junction recombination of the carriers occurs, where holes flow by diffusion from the p-type material into the n-type material, while electrons flow in the opposite direction from the n-type material into the p-type material. As a result a carrier concentration gradient across the junction is

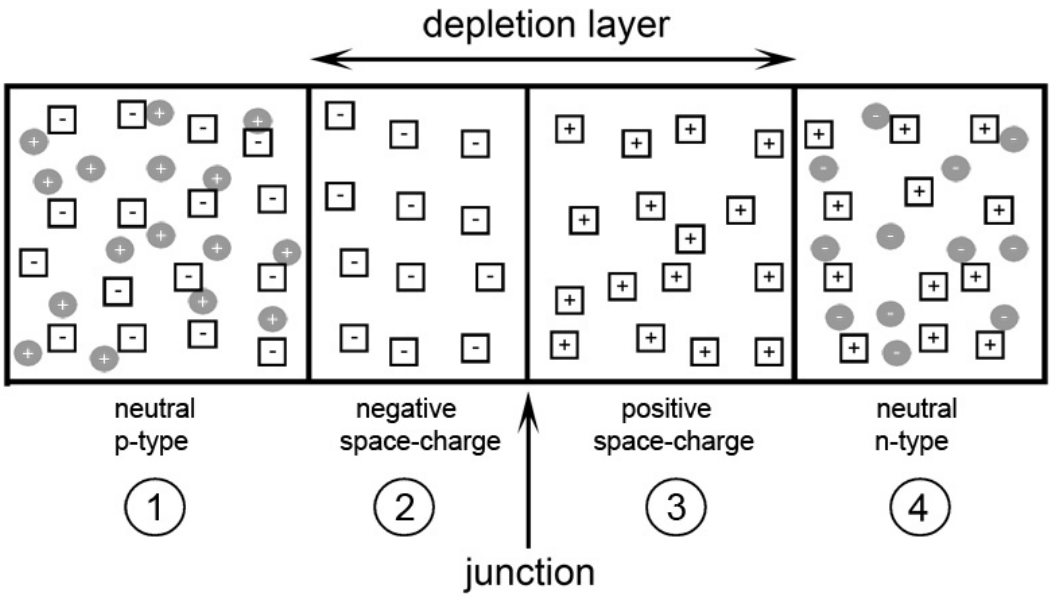

Figure 2.3: *Model of a semiconductor p-n junction. Squares: ion cores of electron donors and electron acceptors respectively; circles: mobile carriers (electrons and holes) [112].*

introduced, forming a depletion layer (indicated with the double arrow in Fig. 2.3). Far away from the junction the n-type and the p-type semiconductors are neutral. The simple model shown in Fig. 2.3 shows the four different zones, distinguishable by

their free carrier concentration, formed around the p-n junction. The sharp change of electron- and hole-concentration leads to a diffusion current into these regions. However, this current is compensated by the drift current caused by the electric field formed in the depletion region. This electric field can be described as a built in potential difference over the junction [112].

p-n junction without applied external field

The relation between carrier density and strength of the electric field is given by Gauss´s Law [112]:

$$\rho = \nabla \cdot \vec{D}. \tag{2.1}$$

With $\vec{D}$ being the electric displacement field, this Maxwell´s equation shows that charge is the source of displacement current in dielectrics. If applied to a semiconductor diode the charge density is only dependent on the distance x from the junction ($\rho(x) = \frac{dD}{dx}$). The electric displacement can be written in terms of the electric field in the case of linear material as $\vec{D} = \epsilon\epsilon_0\vec{\mathscr{E}}$. Using this, equation 2.1 can be written as [112]

$$\rho(x) = \epsilon\epsilon_0 \frac{d\mathscr{E}(x)}{dx}, \tag{2.2}$$

where ϵ and ϵ_0 are the relative permittivity of the material and the vacuum permittivity respectively. Integration of Eq. 2.2 yields the strength of the electric field [112]

$$\mathscr{E}(x) = \frac{1}{\epsilon\epsilon_0} \int \rho(x)\, dx. \tag{2.3}$$

Using this, the potential distribution in the p-n junction without applied external field, known as the diffusion potential, can be determined. The electric field strength $\mathscr{E}(x)$ can be calculated, using equation 2.3 and integrating the carrier density in the four areas, defined in Fig. 2.3. Following another integration the electric potential $V(x) = -\int \mathscr{E}(x)dx$ can be obtained [112]. The overall potential between neutral areas, left (① in Fig. 2.3) and the right (④ in Fig. 2.3) is given by [112]

$$V_D \equiv \frac{e}{2\epsilon\epsilon_0}(N_D x_n^2 + N_A x_p^2), \tag{2.4}$$

where N_A and N_D are the acceptor and donor concentrations respectively, x_n and x_p are the width of the depletion regions in the n-type and the p-type semiconductor respectively, and V_D is the so called diffusion potential. As mentioned previously the areas to the left and to the right of the p-n junction must be neutral, hence the carrier concentrations left and right of the junction have to scale according to the doping concentration:

$$N_A x_p = N_D x_n. \tag{2.5}$$

Therefore the width of the depletion region is dependent on the doping concentration of the semiconductor material used. Bringing this into Eq. 2.4, a relationship between x_p and V_D, and x_n and V_D respectively can be established. Hence the widths of the left and right side of the depletion region can be calculated with [112]:

$$x_n^2 = \frac{2\epsilon\epsilon_0 V_D}{e} \frac{N_A}{N_D N_A + N_D^2}, \qquad \text{and} \qquad x_p^2 = \frac{2\epsilon\epsilon_0 V_D}{e} \frac{N_D}{N_D N_A + N_A^2}. \tag{2.6}$$

where e is the elementary charge. Addition of x_p and x_n gives the width b of the depletion layer in the equilibrium state with no applied external voltage (see Fig. 2.4(a)) [112]:

$$\boxed{b = \sqrt{\frac{2\epsilon\epsilon_0}{e}} \sqrt{\frac{N_D + N_A}{N_D N_A}} \sqrt{V_D}} \tag{2.7}$$

However equation 2.7 cannot be used to calculate b because V_D is not yet known. Therefore, a way to calculate the diffusion potential is needed that can be calculated from the basic properties (i.e. doping concentrations) of the materials forming the p-n junction.

To solve equation 2.2 it was assumed so far that there are no free carriers within the depletion region. However it is clear, that due to a concentration gradient, there is a flow of charge into the depletion layer in which electrons and holes will balance each other [113]. Taking this into account the total charge in equation 2.2 depends not only on the donor and acceptor concentrations, but also on the number of free electrons $n(x)$ and holes $p(x)$ leading to

$$\rho(x) = e(N_D(x) - N_A(x) + p(x) - n(x)). \tag{2.8}$$

In the left, neutral region of the p-doped semiconductor (① in Fig. 2.3), the hole concentration is equal to the acceptor concentration $p = N_A$. Using the electron concentration n_0 and the law of mass action we obtain [112] $n_0 = \frac{n_i^2}{N_A}$. Similarly, using $n = N_D$ for the neutral region of the n-doped semiconductor (④ in Fig. 2.3) we obtain $p_0 = \frac{n_i^2}{N_D}$. The net current consists of two contributions, one induced by the field (caused by $\mathscr{E}(x)$) and the other from diffusion (due to a concentration gradient of the carriers), and can therefore be described as [112]

$$j_e(x) = e\mu_e n(x)\mathscr{E}(x) + eD_e\frac{dn(x)}{dx} = 0, \tag{2.9}$$

where μ_e is the mobility of the electrons and D_e the diffusion coefficient of electrons. $\mathscr{E}(x)$ is known and can be used to calculate $n(x)$ and $p(x)$. By solving Eq. 2.9 for $\mathscr{E}(x)$ and $D_e = \frac{\mu_e k_B T}{e}$ we get

$$\mathscr{E}(x) = -\frac{k_B T}{e}\frac{1}{n(x)}\frac{dn(x)}{dx}, \tag{2.10}$$

where k_B is the Boltzmann constant and T the absolute temperature. Integration from $-x_p$ to x and using $\int_{-x_p}^{x}\mathscr{E}(x)dx = V(x) - V(-x_p)$ the diffusion potential can be calculated in dependence of macroscopic parameters given by the material used and ambient conditions (for a detailed derivation see [112]):

$$\boxed{V_D = \frac{k_B T}{e}\ln\frac{N_D N_A}{n_i^2}} \tag{2.11}$$

p-n junction with applied external field

The model used above can also be applied when an external voltage (V) is applied across the p-n- junction. To determine the diode parameters for this case the same areas as shown in Fig. 2.3 are used [112].

① neutral region of the p-type silicon

② negative depletion region due to acceptor ion cores

③ positive depletion region due to donator ion cores

④ neutral region of the n-type silicon

If an external voltage is applied, in a manner that the positive pole is connected to the n-type semiconductor and the negative pole is connected to the p-type semiconductor ((b) in Fig. 2.4), electrons will drift towards the n-type silicon and holes towards the p-type silicon. This increases the width of the depletion layer, and the conductivity is reduced. This condition is known as reverse bias. If the polarity is changed, called forward bias, the opposite happens, resulting in an increased conductivity ((c) in Fig. 2.4) [114].

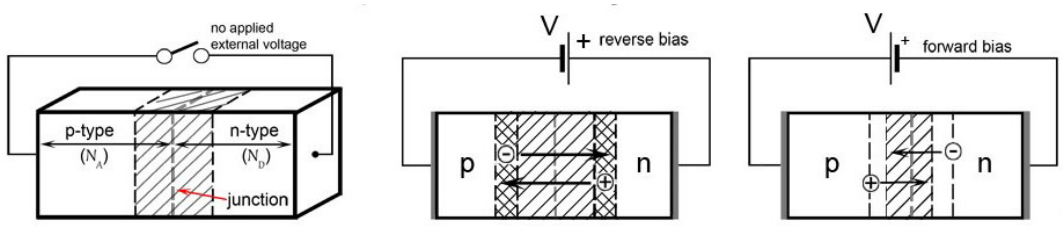

Figure 2.4: *Schematic diagram of a p-n junction* ***(a)*** *without applied external voltage,* ***(b)*** *an external voltage placed across the diode with the same polarity as the built-in potential, so called reverse bias, and* ***(c)*** *with polarity of the external voltage opposing the built-in potential, so called forward bias [114].*

As mentioned above, when the whole potential difference is changed by applying a potential V the width of the depletion layer changes. In this case V_D has to be replaced by $(V_D - V)$ resulting in a modification of equations 2.6 to:

$$x_n^2 = \frac{2\epsilon\epsilon_0}{e}\frac{N_A}{N_D N_A + N_D^2}(V_D - V), \quad \text{and} \quad x_p^2 = \frac{2\epsilon\epsilon_0}{e}\frac{N_D}{N_D N_A + N_A^2}(V_D - V) \tag{2.12}$$

respectively. Hence the thickness of the depletion area of the p-n junction can be expressed as [112]:

$$\boxed{b = \sqrt{\frac{2\epsilon\epsilon_0}{e}}\sqrt{\frac{N_D + N_A}{N_D N_A}}\sqrt{V_D - V}} \tag{2.13}$$

An important description for the use of a diode in electronic circuitry is the I-V characteristic of the device under applied external voltage. For the p-n junction

diode the I-V characteristic can be calculated by summation of the electron j_e and hole j_h currents (see [112] for a detailed derivation):

$$j = j_e(-x_p) + j_h(x_n) = \left(\frac{eD_e}{L_e}n_0 + \frac{eD_h}{L_h}p_0\right)\left(e^{\frac{eV}{k_BT}} - 1\right), \tag{2.14}$$

with $L_e = \sqrt{D_e\tau_e}$ and $L_h = \sqrt{D_h\tau_h}$ being the diffusion lengths and τ_e and τ_h the recombination time for electrons and holes respectively. Equation 2.14 is known as the Shockley diode equation [115], and reveals the characteristic curve of semiconductor diodes. If a positive potential is applied to the diode the current increases exponentially (under forward bias), and if negative potential is applied there is a very small but almost constant current (reverse bias) that will be dominated by tunnelling current for high doped semiconductors and thermally assisted field emission for low doped semiconductor [112–114]. These characteristics enable the utilization of p-n diodes as rectifiers [112,115] The pre-factor in Eq. 2.14 is called the dark saturation or leakage current, and depends only on the geometry of the device and the semiconductor materials used. Using $j_s = \left(\frac{eD_e}{L_e}n_0 + \frac{eD_h}{L_h}p_0\right)$ the Shockley equation can be written in its well known form

$$j = j_s\left(e^{\frac{eV}{k_BT}} - 1\right), \tag{2.15}$$

which applies to both p-n junction and Schottky diodes. As shown in figure 2.5 the reverse saturation current for a Schottky diode is generally much larger than that for a p-n junction diode and the breakdown, when the charge flows freely under reverse bias, is at lower voltages.

2.3.2 The metal-semiconductor interface

Metal semiconductor interfaces are important elements in electronic circuitry. On the one hand they are used for providing contact to electronic components (mainly independent of polarity (as shown in Fig. 2.4(a)), whereas on the other hand they can be used to form discrete non-linear components, for example Schottky diodes. If this system is used for providing contact, the aim is to achieve a linear, polarity

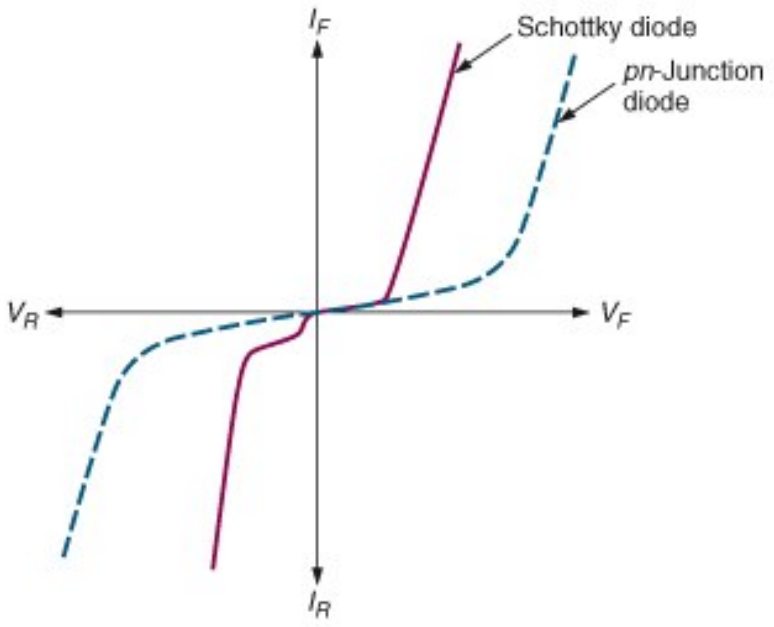

Figure 2.5: *I-V curve for Schottky diode and p-n junction diodes [116].*

independent I-V characteristic with as low as possible contact resistance ('ohmic contact') [113]. This is, however, not possible for 'real' components. For the Schottky contact, the metal-semiconductor junction is used in a way that the contact resistance is mainly dependent on the polarity and hence the I-V characteristic of a diode is achieved [113]. In both cases the I-V characteristics are determined by the potential barrier introduced by the metal-semiconductor interface. In contrast to p-n junctions the height of the barrier is determined by the work-function for both, the metal and semiconductor respectively [117], the depression of the barrier due to a applied potential ('Schottky-effect') and the density of surface states in the semiconductor at the boundary layer [112].

2.3.2.1 The metal-vacuum system

The work function of a material is defined as the energy difference between the Fermi-energy E_F of a solid and the vacuum level. For metals the work function (Φ_{me}) is of the order of a few eV. The highest work function metal is platinum with $\Phi_m = 5.28\,eV$, compared to hydrogen with $13.6\,eV$. For metals the occupied

energy states start at the Fermi level, where for semiconductors there are normally no available energy states. Therefore it is sensible to change the concept of the work function for semiconductors to the electron affinity (or vacuum ionization energy) $e\chi$, which is introduced as the difference between the vacuum level and the bottom of the conduction band (E_c, see Fig. 2.6). For semiconductors the electron affinity depends on the doping level, as the Fermi level moves relative to the conduction band. For n-type silicon with a doping concentration of $10^{16} cm^{-3}$ it is $4.20\,eV$ [114]. If a potential is applied it is possible to lower the energy barrier between the material used and the vacuum level of another material. This behaviour describes the Schottky effect, which is very important for the description and application of metal-semiconductor systems.

2.3.2.2 The ideal metal-semiconductor system

Similarly to the p-n junction described in section 2.3.1, the metal-semiconductor system is another junction that can be used to produce rectifying devices [112, 118]. Discovered in 1938 this mode of action is named after *Walter Schottky*. An easy way to explain the proportions in a Schottky contact is to use the energy band scheme. Figure 2.6 shows the energy band diagram of a metal-n-type silicon Schottky contact. Here the surface is assumed to be ideal (i.e. no surface states or image force lowering [119, 120]). As previously mentioned it is necessary to overcome an energy

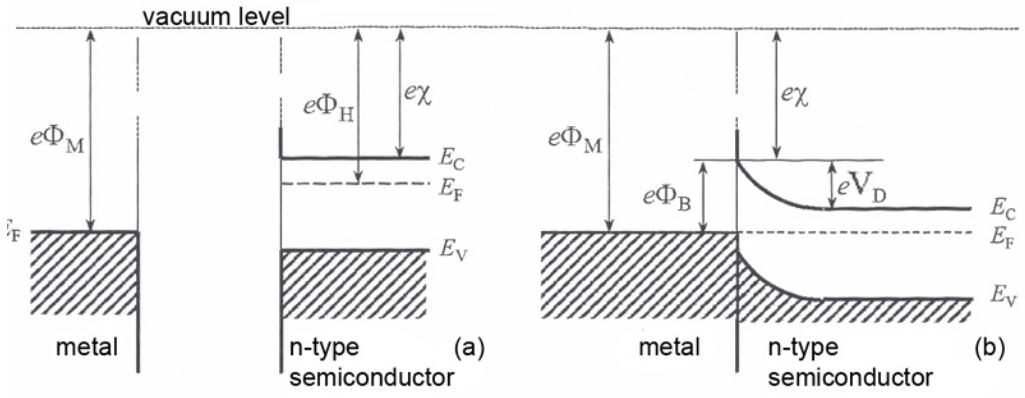

Figure 2.6: *Energy band diagram of a metal/semiconductor contact with $\Phi_{me} > \Phi_{sc}$.* ***(a)*** *Before contact is made,* ***(b)*** *after contact is made. [112]*

barrier at the material surface in order to extract electrons. For metals this barrier is the work function defined as the energy difference $e\Phi$ between vacuum level and the Fermi level ($e\Phi_M$ for the metal [112], see Fig. 2.6). For semiconductors, it is the electron affinity (eχ).

In Fig. 2.6(a) the case of metal and semiconductor not being in contact is shown, and the metal and semiconductor are not in equilibrium. If both materials are brought into contact, equilibrium will be reached and the situation will change as shown in Fig. 2.6(b). As seen in Fig. 2.6(a), in this example the metal work function $e\Phi_M$ is larger than the electron affinity $e\chi$ of the semiconductor. Hence the electrons in the semiconductor are at a higher energy level than in the metal, hence they will drift to the metal, when the two materials are brought into contact.

A positive space charge of the donor ion cores is therefore left close to the junction, and the same situation as described at n-type silicon side of the p-n junction (③ in Fig. 2.3) will occur. The energy band on that side will be raised, but nothing will happen at the metal side of the junction, because the small amount of electrons added is negligible compared to the large number of electrons in the metal [112]. When equilibrium is reached the Fermi levels of the metal and the semiconductor respectively will be equal. This is schematically shown in Fig. 2.6(b) and reveals that the the Fermi energy of the semiconductor will be suppressed for the width of the depletion layer formed. Whereas the energy difference of the Fermi levels of the materials was $e\Phi_M - e\Phi_H$ before the materials were brought into contact, there is no energy difference between the Fermi levels after they are in contact. However a barrier is built up in the semiconductor [112, 113]. The height of the conduction band E_C is therefore dependent on the distance form the junction x and hence $E_C = E_C(x)$. The barrier height V_D can be calculated using the diffusion current V_D in a similar manner to that previously shown for the p-n junction. As shown in Fig. 2.6: $eV_D = e\Phi_M - e\chi$ [112]. Hence the barrier height at the semiconductor side is eV_D whereas at the metal side it is $e\Phi_B = e\Phi_m - e\chi$ and therefore the electrons moving from the metal into the semiconductor experience a higher barrier compared

to the electrons moving in the other direction. Similarly to the p-n junction, the width of the depletion layer of the semiconductor can now be calculated as [112]:

$$b = \sqrt{\frac{2\epsilon\epsilon_0}{e}}\sqrt{\frac{1}{N_D}}\sqrt{V_D - V} \tag{2.16}$$

This is possible because it is feasible to consider the metal-semiconductor junction as an asymmetric $p^+ - n$ junction where the concentration of the acceptors of the p-type semiconductor is much higher then the donor concentration of the n-type semiconductor. To calculate the net current through the metal-semiconductor junction the following derivation is followed.
The electron concentration (n) on the semiconductor side at the junction (j) can be written as [112]:

$$n_j = \mathcal{N}_C \cdot e^{-\frac{E_{C,j}-E_F}{k_B T}} = \mathcal{N}_C \cdot e^{-\frac{e\Phi_B}{k_B T}} \tag{2.17}$$

where $\mathcal{N}_C$ is the effective density of states in the conduction band, $E_{C,j}$ is the energy height of the conduction band at the junction. The concentration of the electrons is significantly lower at the junction, compared to the bulk (further away) of the semiconductor, due to the larger distance of the band border $E_{C,j}$ to the Fermi level E_F ($E_C(junction) - E_F > E_C(inside) - E_F$). If a forward voltage is applied to the metal-semiconductor junction the energy level of the conduction band inside the semiconductor is raised by eV [112, 113]:

$$n_j(V) = \mathcal{N}_C \cdot e^{-\frac{\Phi_B - V}{k_B T}} = n_j e^{\frac{eV}{k_b T}}. \tag{2.18}$$

Furthermore it can be assumed that the electron current, flowing from the semiconductor to the metal, is proportional to the electron density at the barrier

$$j_{H\to M} = c n_j(V) \tag{2.19}$$

where c is a constant which is unknown at this stage [112]. Because the barrier height in the metals is independent of the applied voltage V, the current flowing from the

metal into the semiconductor can be assumed to be constant. If no voltage is applied across the junction the two currents have to be in equilibrium. Therefore

$$j_{M\to H} = -j_{H\to M}(V=0) = -cn_j(V=0). \tag{2.20}$$

If an external voltage V is applied, the difference of (2.19) and (2.20) reveals the net current to be [112]:

$$j = j_{H\to M} - j_{M\to H} = c(n_j(V) - n_j) = c\mathcal{N}_C e^{-\frac{e\Phi_B}{k_B T}}\left(e^{\frac{eV}{k_B T}} - 1\right) \tag{2.21}$$

This equation has the same form as Eq. 2.14 obtained to describe the I-V characteristics of p-n junctions:

$$\boxed{j = j_s\left(e^{\frac{eV}{k_B T}} - 1\right)}. \tag{2.22}$$

The pre-factor j_s also represents the saturation current of the metal-semiconductor junction. It can be shown that this can be written as follows (for a detailed derivation see [114]):

$$j_s = R^\star \cdot T^2 e^{\frac{e\Phi_B}{k_B T}}. \tag{2.23}$$

were $R^\star$ is the Richardson constant [112, 121, 122].
For a p-n junction the saturation current I_S depends on the diffusion length and the injected minority carriers (see section 2.3.1). In contrast, in a Schottky diode the current is due to thermionic emission (as described for the metal-vacuum system section 2.3.2.1) of the semiconductor´s majority carriers across the Schottky barrier Φ_B [118].

The real Schottky contact

The Schottky barrier above is described ideal, assuming atomically flat surfaces and perfect contact between the metal and the semiconductor. A real heterostructure will however, not represent this ideal system. To account for the non-idealities it is

common to include the diode ideality factor η into the diode equation (2.22) [113]:

$$I = I_s \left(e^{\frac{eV}{\eta k_B T}} - 1 \right) \tag{2.24}$$

The diode ideality factor is an empirical 'ideality' coefficient which should be unity for an ideal contact. However Schottky contacts with idealities $\eta > 1$ are common in literature and can be ascribed to several effects [123]:

- interface states at a thin oxide between the metal and the semiconductor;
- tunneling currents between the metal and the semiconductor;
- tunneling currents in highly doped semiconductors;
- image force lowering of the Schottky barrier in the electric field at the interface; and
- generation/recombination currents within the space-charge region.

These effects all assume spatially homogenous interfaces between the materials used. For the screen printed layers, made of nanoparticulate silicon with a disperse size distribution and printed on a rough substrate, however this assumption is not valid. J. H Werner and H. H. Güttler [123] suggested, that the influence of two-dimensional band inhomogeneities results in different Schottky barriers for currents (see Fig. 2.7) due to spatial variations of band bending V_d and Schottky barrier height Φ_b. The shape and position of the ridges in the potential 'mountains', caused by different particle sizes and rough substrate, depend on the bias voltage and cause therefore idealities $\eta > 1$ [123].

The effect of the diode series resistance R_S is usually modeled with a series combination of a diode and a resistor with resistance R through which the current I flows [125, 130]. The voltage V_D across the diode can then be expressed in terms of the total voltage drop V across the series combination of the diode and the resistor. Thus, $V_D = V - IR_S$ and for $V_D > 3k_BT$ Eq. 2.24 becomes [130]

$$I = I_s \left(e^{\frac{-e(V-IR_S)}{\eta k_B T}} \right). \tag{2.25}$$

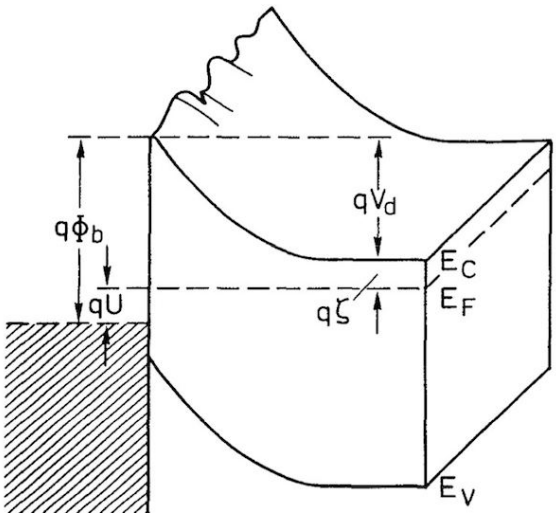

Figure 2.7: *Two-dimensional band diagram of an inhomogeneous Schottky contact [123].*

The saturation current I_s is usually described within the thermionic emission theory as [125, 131]

$$I_s = AA^{\star}T^2 e^{\frac{-e\Phi_B}{k_B T}}. \tag{2.26}$$

A method to extract the series resistance R_S of ideal Schottky diodes (i.e., $\eta = 1$) was first proposed by Norde in 1979 [132]. For the cases where $\eta > 1$, Sato and Yasumura modified Norde´s approach to extract the values of η, Φ_B, and R_S from the forward I-V characteristics of a Schottky diode [130] using two experimental I-V curves. Another approach to obtain the diode parameters from diodes with series resistance is to approximate Eq. 2.25 for $V_D = V - IR_S > {}^{\eta k_B T}/_{e}$, and Eq. 2.25 becomes [133]

$$I = AA^{\star}T^2 e^{\frac{eV_D}{\eta k_B T}} e^{\frac{e(V-IR_S)}{\eta k_B T}}. \tag{2.27}$$

This equation predicts a linear variation of $\ln I$ with V_D [133]

$$\ln I = \ln I_S + \frac{eV_D}{\eta k_B T} = lnI_S + \frac{e(V - IR_S)}{\eta k_B T}. \tag{2.28}$$

A plot of $\ln I$ vs. V remains linear as long as $V \gg \frac{\eta k_B T}{e}$ and $V \gg IR_S$ [133], and the ideality factor from Eq. 2.25 can be written as

$$\eta = \beta \frac{dV}{d \ln I} \tag{2.29}$$

where $\beta = \frac{e}{k_B T}$. This plot is used as the standard method [125, 133] and I_S is extrapolated from the intercept with the zero voltage axis. The zero voltage barrier height Φ_B is deduced from Eq. 2.26. However, this can only be used for diodes with a moderate series resistance, as the linear region shrinks as R_S is increased [133].

2.3.2.3 Ohmic contacts

As shown in Fig. 2.4 ohmic contacts are important for circuitry. The Ohmic contact is a low resistance, non-rectifying junction that provides current conduction from a metal to a semiconductor and vice versa [114]. The above described junctions which exhibit rectifying behaviour are to be avoided for ohmic contacts as the above described Schottky barrier contact is not desirable. Therefore the materials used need to be chosen carefully.

One way of obtaining a low barrier contact is, if the work function of the metal is smaller than the electron affinity of the semiconductor used, in contrast to the case described in Fig. 2.6. In this case, the conduction band energy is reduced at the barrier, which prevents the electrons experiencing a barrier when moving from the semiconductor into the metal. There will only be a very small barrier in the other direction [112, 113]. In contrast to the Schottky barrier this results in a similar conductivity under both forward- and reverse-bias. Due to interfering surface states, this is not easily realizable in practice. Usually for compound semiconductors ohmic contact by band alignment is hard to realize due to the presence of surface states [134, 135] and Fermi level pinning [136–138]. For p-type semiconductors, a further problem is the unavailability of metals with high enough work functions.

However, according to equation 2.16 it is possible to reduce the width of the depletion layer by increasing the doping concentration. If the doping concentration is high enough the depletion layer is narrow enough that electrons are able to tunnel through the barrier and hence the contact is non-rectifying, and an ohmic contact is formed which is able to conduct current in both directions equally. Another important requirement is, that the voltage drop across the contact is very small, and does not affect the performance of the device [111]

3 Experimental

In printed electronics there are different approaches for device production, which in contrast to the mainly crystalline silicon based traditional electronics, are based on a variety of new materials like organic semiconductors [139,140] and inorganic nanoparticles and semiconductors, such as ZnO [141,142]. In this work silicon nanoparticles have been used to developed fully printed silicon nanoparticulate diodes.
In section 3.1 it is described how high quality silicon nanoparticles, with stable, essentially oxide-free surfaces, were produced. Furthermore the process of producing screen printable inks, and the printing of the inks, which on curing have unique semiconducting properties [39,143], is described. Finally the design and production of printed diodes is discussed.
Detailed information on the characterization of the powder, the printed layers and fully printed devices is given in section 3.2. Different spectroscopy and microscopy techniques have been utilized to understand the microstructure of the particles, the printed layers, and the fully printed devices. Scanning electron microscopy (SEM), focused ion beam (FIB), high resolution transmission electron microscopy (HRTEM) and high-angle annular dark-field images obtained with a scanning transmission electron microscopy (HAADF-STEM), STEM in combination with energy-dispersive X-ray spectroscopy (STEM-EDX), as well as mid infrared scanning near-field optical microscopy (IR s-SNOM), have been used to understand and reconstruct the microstructure of printed devices. Raman-spectroscopy was also used to support the microscopy studies. Finally the methods used for electrical characterisation of the printed layer and the properties of the printed diodes are described at the end of this chapter.

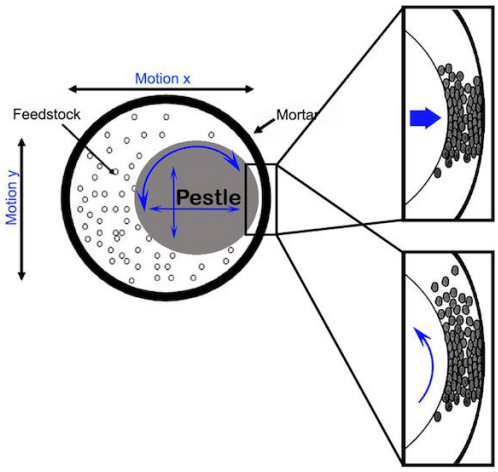

Figure 3.1: *Schematic drawing showing the different forms of impact which occur during high-energy milling. [80]*

3.1 Nanoparticle production, printing and device fabrication

3.1.1 Nanoparticle production by high energy milling

Mechanical milling is a process which is routinely used in powder metallurgy and in the mineral processing industry. Excessive plastic deformation of the particles and cold welding between particles are absent in the process [92]. For this thesis silicon nanoparticles were produced by high energy mechanical milling using a vibratory disc mill. A 5200 chrome steel milling pot and pestle are mounted on a base set to deliver vibrations in two axes causing rotational and lateral motion of the pestle. Due to this motion, as indicated in Fig. 3.1, brittle feedstock is fractured and attrited progressively resulting in nanometre sized particles with a disperse log normal size distribution [80, 92, 94].

In this study three types of silicon have been used as feedstock. For high and intermediate doping levels, Czochralski grown prime grade boron and phosphorous doped silicon ingots and wafers (Siegert Wafer GmbH, Aachen, Germany) were used. The ingots had a nominal resistivity of $\rho < 0.001\,\Omega cm$ for the p-type (boron doped) and $\rho = 0.001 - 0.00102\,\Omega cm$ for the n-type (phosphorous doped) silicon. Wafers with

a nominal resistivity of $\rho < 0.005\,\Omega cm$ for the boron doped and $\rho = 0.008 - 0.02\,\Omega cm$ for the phosphorous doped silicon were used to provide particles with a lower doping level. Even lower doping levels were obtained using phosphorous doped wafers with a resistivity of $\rho = 1 - 10\,\Omega cm$ (Siegert Wafer GmbH, Aachen, Germany) and 2503 grade metallurgical silicon (Silicon Smelters, Polokwane, South Africa). According to the manufacturer's analysis, the purity of the metallurgical silicon is 99.4%, with the main impurities being Fe at 0.21% and Al at 0.144%. Other specified impurities were Ca, Ti, Cr, P, and Ni with concentrations, of 230, 129, 62, 43 and 18 ppm respectively [109]. It had previously been observed that during extended milling periods the powder was compressed into a compact 'cake', making the size reduction process less efficient. Consequently for the nanoparticles produced for this work the milling procedure was interrupted to redistribute the powder. This was performed every 15 minutes for a total milling period of 1.5h, and every 30 minutes for a total milling time of 5h respectively. On completion of the milling, the pots were allowed to cool down to room temperature, before the powder was harvested in its dry state and stored under ambient conditions. Furthermore carbon nanoparticles have been prepared from graphite feedstock (Sigma Aldrich, Fluka Analytical) with a nominal size of $\leq 0.1\,mm$. The carbon was continuously milled for 1 hour in a similar manner to the silicon.

3.1.2 Ink formulation

To be suitable for screen printing an ink must have specific rheological features. The most important one is that the ink is stable against phase separation of the liquid and solid components under applied shear force. Furthermore the print quality and properties of the cured layer depend strongly on the rheology of the ink. In general screen printing ink needs to be dilatent (shear thinning) and thixotropic. Only the right combination of viscosity, thixotropy, and viscoelastic properties will ensure that the ink flows through the screen but does not flow on the substrate once printed and therefore ensures that the print has both good edge definition and coverage [47, 144]. In other words, the ink produced has to be adjusted to obtain appropriate rheological

properties that ensure a homogenous distribution of the printing paste on the screen and its uniform flow through the screen openings [145].

In this work in order to prevent incompatibility issues between different materials both water based acrylic and solvent based inks were investigated. Both ink systems were used to produce conductive and semiconducting inks. Using the water based acrylic ink, carbon nanoparticles and graphene platelets (IoLiTec Ionic Liquids Technologies GmbH,size 6-8nm, 99,5%) have been used as conducting materials and silicon nanoparticles have been used for the semiconducting layer. The solvent based system was additionally used for conducting inks containing silver nanoparticles and carbon nanotubes.

In previous works it could be shown that the performance of fully printed devices can be optimized if a particle loading of 80% by weight is used [108–110]. A lower particle loading results in a very high resistivity of the printed layer, whereas a higher particle loading results in poor printability of the ink [109, 110]. For inks with this particle loading the typical thickness of a layer produced by screen printing is approximately $25\mu m$.

Inks were produced from all types of nanoparticles by successive addition of the powder to the binder. The respective solvent or thinner was added to obtain the final properties necessary for printing. Silicon inks, with 80% particle loading by relative weight to the total weight of particle and binder, were produced with a commercially available acrylic ink base supplied by Marchem, Cape Town South Africa. For these inks reagent grade propan-1,2-diol (propylene glycol) from Sigma Aldrich was used as a thinner. It was shown in a previous work, that for a silicon ink which contains 20% by mass of binder, after curing the binder reduces to a residue of about 8.7% [109]. The same binder and thinner combination was used to produce conductive inks using milled carbon nanoparticles (as described in 3.1.1) and graphene platelets (IoLiTec Ionic Liquids Technologies GmbH,size 6-8nm, 99,5%).

ETHOCEL^{TM} ethyl cellulose and CELLOSOLVE^{TM} butyl (Dow Chemical) were used as the binder and solvent respectively in the solvent-based inks. With one exception these inks contained a particle loading of 70% by relative weight and the binder fraction was not reduced on curing. Conducting inks containing different particles

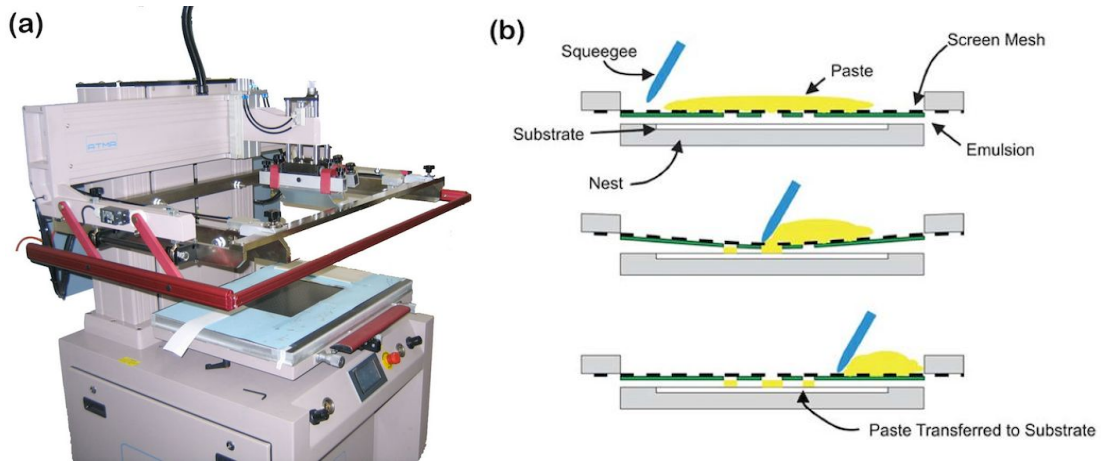

Figure 3.2: ***(a)*** *The ATMA AT-60PD semi-automatic flatbed screen printer used to print all devices described in this thesis.* ***(b)*** *Schematic drawing of the processes during screen printing [146].*

have been produced. The feedstock used were graphene platelets (IoLiTec Ionic Liquids Technologies GmbH, size 6-8 nm, 99,5%), multiwalled carbon nanotubes of $20 \sim 30\,\mu m$ diametre, and $10 \sim 20\,\mu m$ length (Nanocs Inc.) and silver nanoparticles with a nominal size of $70\,nm$ (Sigma Aldrich) [143]. Additionally conducting inks were mixed with 80% particle loading of graphene platelets (IoLiTec Ionic Liquids Technologies GmbH, size $6 - 8\,nm$, $99,5\%$) .

3.1.3 Printing of devices

To print the devices studied in this work an ATMA AT-60PD semi-automatic flatbed screen printer, shown in Fig. 3.2(a), was used. Screen printing is arguably the one of the most versatile printing methods. In principle it requires only four elements: the screen which carries the image, the squeegee, an ink or paste, and the substrate on which the design is printed. Ink is applied to the screen and is then forced through fine mesh openings forming the positive areas of the image, by the squeegee dragged across the screen. Shear forces cause the ink to flow through the open areas of the screen, as shown schematically in Fig. 3.2(b).

The two different designs used to print diodes are shown in Fig. 3.3. In order to produce a diode, three materials are printed: first a conductive layer (bottom

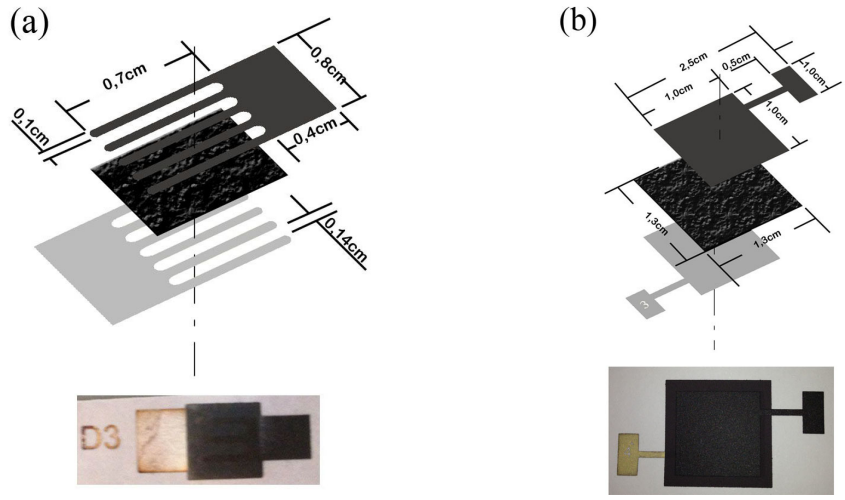

Figure 3.3: *The two designs used to produce diodes:* ***(a)*** *lateral design and* ***(b)*** *opposed design.*

contact), followed by the semiconducting silicon layer (active material) and finally a second conductive layer (top contact). In Fig. 3.3 the layers are as follows: the bottom layer is a conductive ink (light grey), followed by the silicon nanoparticulate ink (black) and another conductive ink (dark grey), different from layer 1, as a top contact. Fig. 3.3(a) shows a lateral interdigitated design where the conductive tracks do not overlap, but have a gap of about $200\,\mu m$ between each finger. In contrast Fig. 3.3(b) shows a planar opposed design where the second conductor layer is printed directly above the first one. The lateral design has the advantage that shunts between the conductors through the active layer are not possible, which is the main problem with the opposed design. It is also possible to vary the print sequence so that the contacts are either on the same side of the active layer or on opposite sides. In this work the latter was used. The disadvantages of the lateral design are: that the gap between conductive layers is larger, and that registration of the prints is more difficult, which is not a problem in the planar design. The gap in this design is determined by the thickness of the printed silicon layer, and hence is about $1/10$ that of the lateral design. In this thesis the layered design was used to consequently ensure a lower resistance of the semiconducting layer and therefore reduce the overall resistance of the printed device in order to improve the device performance. The active area of the lateral design is $0.7 \times 0.8\,cm^2$ consisting of six interlocking fingers with 3 devices per print. For the opposed design, three different sizes of devices were

printed: $0.5 \times 0.5\,cm^2$; $1.0 \times 1.0\,cm^2$; and $2.0 \times 2.0\,cm^2$ with two devices of each size on a screen.

The individual layers were printed using a SEFAR monofilament polyester mesh with an average screen tension of $24 \pm 2\,{}^{N}/_{cm}$. For the semiconducting and conducting inks mesh of diametre 40 microns and mesh count $100\,{}^{lines}/_{cm}$ and diameter 31 microns, and mesh count $150\,{}^{lines}/_{cm}$ were used respectively. The squeegee speed was set to $250\,{}^{mm}/_{sec}$ for printing commercially available silver inks, used for the bottom contacts, and $200\,{}^{mm}/_{sec}$ for all other inks. A double stroke print mode was used to ensure near uniform printed layers with no pinholes. Special attention was paid to screen registration when printing the lateral design to ensure uniform gap size between the interlocking fingers. i.e. that the layers are aligned with each other. All prints were allowed to dry for 24 hours, under ambient conditions, before printing the subsequent layer. No post processing steps such as sintering or annealing were performed. An overview of all devices printed for this thesis is given in the appendix.

Conductors were printed with commercially available silver nanoparticle ink PSI-211 (PChem Associates, Inc, Bensalem, PA, USA), DuPont 5000 silver ink (Du Pont (U.K.) Limited, Bristol, U.K.), and inks made with silver nanoparticles (Sigma Aldrich) as described in 3.1.2. The substrate material for the prints was polyethylene terephthalate (PET) for the devices using carbon nanotubes from Canatu and uncoated paper of area density $80\,gsm$ and $160\,gsm$ for all other devices. For characterization purposes individual layers of each ink were also printed. Samples suitable to be used with focused ion beam and high resolution transmission electron microscopy (HRTEM) for cross sectional studies also had to be prepared. For these studies silicon inks p-type (boron doped, $\rho < 0.005\,\Omega cm$ and $\rho < 0.001\,\Omega cm$) and n-type (phosphorus doped, $\rho = 0.008 - 0.02\,\Omega cm$ and $\rho = 0.001 - 0.00102\,\Omega cm$) were printed on prime grade boron doped wafers (Siegert Wafer) to ensure mechanical stability during sample preparation. The printing process used was the same as for the diodes except that conducting contacts were not printed. After printing, these individual layers were dried under ambient conditions. To investigate a cross section of a diode, a fully printed device on a paper substrate, was embedded in EPO-FIX embedding resin (EMS Hatfield USA) in order to stabilize the printed layer. After

drying for 24 hours, under ambient conditions, the specimen was cut using a diamond saw and subsequently mechanically polished, for examination using FIB, HRTEM, HAADF-STEM, and SEM.

3.2 Characterization of silicon nanoparticles and printed layers

In order to gather a more detailed understanding of the microstructure of the silicon nanoparticles as well as the printed layers, different microscopy and spectroscopy techniques have been used for this study. A combination of scanning electron microscopy (SEM), high resolution transmission electron microscopy (HRTEM), focused ion beam (FIB) and high-angle annular dark-field images obtained with a scanning transmission electron microscopy (HAADF-STEM) as well as STEM combined with energy-dispersive X-ray (EDX) spectroscopy was used to investigate the assumption of chemical passivation of the silicon nanoparticle surface with oxygen, and the observed charge transport [109] between particles and throughout printed silicon layers. STEM is an imaging technique which offers some advantages over conventional TEM, chiefly due to the fact that STEM images are directly interpretable and have a high atomic number sensitivity [147]. In each case, state-of-the-art structure determination complimented the high-resolution imaging to provide a framework for the analysis of nanoparticle surface structures through electron microscopy.

3.2.1 Morphology and internal structure of silicon nanoparticles

For sample preparation a small amount of Si nanoparticles dispersed in about $20\,ml$ of methanol (Sigma Aldrich anhydrous min. 99.5%). To break up large clusters the solution was then sonicated for about 30 seconds in a ultrasonic bath. An aliquot was drawn from the center of the suspension with a micropipette and drop-cast

onto a polished silicon wafer and a holey carbon coated TEM grid respectively. After drop-casting the samples were dried under ambient conditions. The particles drop-cast on the wafer were further prepared and investigated on a Zeiss Auriga Cobra FIB FESEM. The focused ion beam was used with an acceleration potential of $30\,kV$ at a current of $50\,pA$ to slice the drop-cast particles. To obtain information on the internal structure of the particles, imaging after cutting was performed using SEM with a $2\,kV$ electron beam in secondary electron imaging mode.
Imaging of the lattice planes near the surface has been performed in previous works [108, 109]. These studies concluded that there is no, or only a very thin, capping layer on the surface of the silicon nanoparticles. However, in these works it can be seen that the surface and interface atoms of the silicon nanoparticle are not clearly imaged due to aberrations in the optical system. To verify the interpretation of the previous results, changes in lattice positions of the order of 0.5 Å need to be resolved with confidence. This can be achieved if the image has a much higher quality. Therefore a microscope with a much higher point-to-point resolution was used.

Transmission Electron Aberration-corrected Microscope: TEAM 0.5. The TEAM 0.5 microscope is ideally suited to this need. Based on an FEI Titan 80-300 microscope the TEAM 0.5 at The National Center for Electron Microscopy, Lawrence Berkeley Laboratories, CA USA is a double-aberration-corrected transmission electron microscope. For improving the resolution and sensitivity spherical aberration C_s correction permits the generation of smaller electron probes with higher currents, thus significantly improving both. Chromatic aberration C_c correction as well as energy filtering also offers the opportunity to obtain images with a much higher resolution and contrast [149]. The TEAM 0.5 is equipped with a special high-brightness Schottky-field emission electron source, a gun monochromator, a high resolution GIF Tridiem energy-filter and two CEOS hexapole type spherical aberration correctors. Axial aberrations up to 4th order as well as 5th order spherical aberration and six fold astigmatism are corrected by the illumination aberration corrector. The imaging aberration corrector fully corrects for coherent axial aberrations

Figure 3.4: *The Transmission Aberration Corrected Microscope* TEAM *0.5 [148].*

up to 3rd order and partially compensates for 4th and 5th order aberrations [148,150]. For this study, silicon nanoparticles milled for 5 hours and drop-cast on a carbon coated holey grid were used. For imaging the instrument was operated at $80\,kV$.

3.2.1.1 Elemental mapping of silicon nanoparticles

In order to obtain more detailed information about the surface of the silicon nanopartilces produced with high energy milling, elemental mapping was performed. This was achieved using high-angle annular dark-field images (HAADF) obtained with a scanning transmission electron microscopy (STEM). This technique is ideally suited for elemental mapping. Images are formed by collecting high-angle scattered electrons with an annular dark-field detector in dedicated STEM instruments. The contrast of HAADF images is strongly dependent on the average atomic number of the scatterer encountered by the incident probe (Z contrast) [147]. The imaging was carried out with a Titan 60-300 electron microscope equipped with a Cs-corrector at $300\,keV$ beam energy at the electron microscopy laboratory at CIC nanoGUNE

in San Sebastian, Spain. The instrument was operated in STEM spectral imaging mode.
For the fully printed diode elemental mapping has been performed on a cross section using STEM images with the same instrument. In order to obtain the elemental map, the beam is scanned on the sample in STEM mode. Scanning transmission electron microscopy with energy dispersive x-ray spectroscopy (STEM-EDX) in particular has been shown to be a powerful, direct technique to study local compositional variations [151]. A full EDX spectrum is recorded in every beam position. A posteriori thus obtained 3-D data cubes (having the dimensions x, y and energy) are processed and (x, y) maps of intensity of characteristic peaks of the elements are plotted, giving the distribution of these elements on the sample.

3.2.2 Surface and structural analysis of printed layers

To study the surface morphology of printed layers SEM, FIB and HRTEM were used in this work. A FEI Nova NanoSEM 230 scanning electron microscope (SEM) was used to gather information about the surface topography of layers printed on paper substrate, and cross sections thereof produced by simply cutting printed layers with a sharp blade, without embedding them into resin.
With the use of FIB more detailed cross sectional information of the printed layers was obtained. Furthermore, the interfacial and network characteristics of silicon nanoparticle layers has been investigated [39]. Therefore HRTEM studies of a lamella of p-type silicon (90 minute milled p-type wafer, $\rho < 0.005\,\Omega cm$) printed onto a wafer as substrate have been carried out. For this purpose a lamella of the printed layer was produced by focused ion beam with in-situ lift out, using a FEI Helious NanoLab^{TM}DualBeam^{TM} FIB/SEM at CIC nanoGUNE in San Sebastian, Spain.
Due to the high porosity of the printed layer, as indicated in Fig. 3.5(a), precautions had to be taken to prevent damage to the lamella during preparation, as well as to avoid curtaining due to high surface roughness and strong variations in density [152]. Sample preparation took place in several steps: The position of the future lamella was covered by a 0.5 μm thick flat diamond membrane to ensure uniform milling

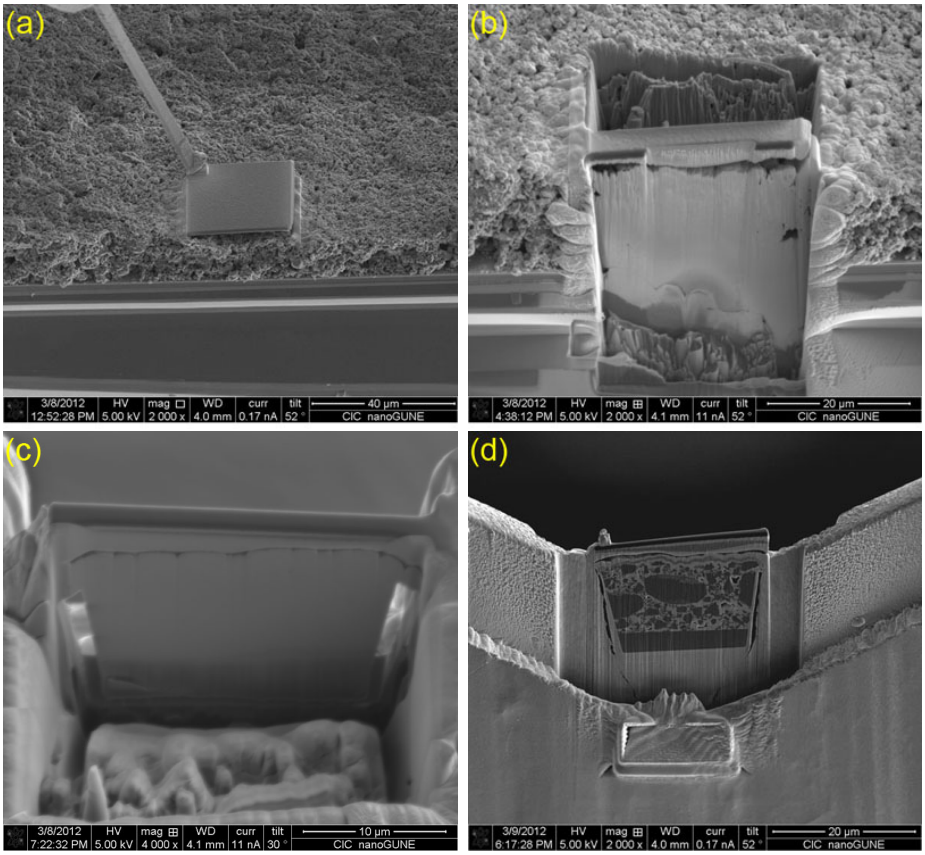

Figure 3.5: ***(a)*** *Surface view of the printed silicon layer, showing it´s porosity and a diamond membrane placed on top of the silicon layer as preparatory step for FIB cutting,* ***(b)*** *Pt covered cleaned cut surface to stabilize lamella,* ***(c)*** *lamella before it was undercut, extracted and mounted onto a standard FIB half grid, and* ***(d)*** *lamella mounted on a TEM half grid before polishing.*

(Fig. 3.5(a)). After digging a deep trench front and back, the sides of the future lamella were cleaned by FIB and its pores were filled with Pt by electron beam induced deposition (EBID) (Fig. 3.5(b)). The lamella was then polished to remove the amorphous surface layers. Thus prepared the lamella with a thickness of about $3\,\mu m$ (Fig. 3.5(c)) was undercut, extracted and mounted onto a standard FIB half grid. The lamella was fixed by Pt deposits on three sides to prevent it from bending in the final polishing step as seen in Fig. 3.5(d). The lamella was finally polished from both sides to electron transparency with a 5 keV ion beam energy to remove surface amorphous layers. HRTEM imaging was performed, using a FEI Titan 60-300 electron microscope equipped with imaging Cs-corrector at $300\,keV$ beam energy at

the electron microscopy laboratory at CIC nanoGUNE in San Sebastian, Spain. Additional cross sections of printed layers were also produced for structural analysis using focused ion beam and mechanical polishing. For the first study, a diode fully printed on paper (as described in section 3.1.3) was used. The cross sectioning and imaging was performed with focused ion beam using a Zeiss Auriga FIB/SEM at the National Centre for Nano-structured Materials, Pretoria. Secondly another diode was embedded in resin and cross sectioned using a diamond saw, and subsequently mechanically polished. Imaging was done using a Quanta^{TM}250 FEG environmental scanning electron microscope (ESEM) at CIC nanoGUNE in San Sebastian, Spain.

3.2.3 Infrared scanning-type near-field optical microscopy (IR s-SNOM)

In 1928 E. H. Synge proposed a scanning method [154], to extend the resolution of a microscope, beyond the diffraction limit discovered by Abbé and Rayleigh. In optical microscopy the limiting factor is the Rayleigh criterion, for which the minimum distance Δx_{min} which can be resolved, by an optical system with opening angle Θ in a medium of refractive index n between two distinct point sources is [117]

$$\Delta x_{min} = \frac{0.61\lambda}{n \sin\Theta}, \tag{3.1}$$

where λ is the wavelength. The denominator in Eq. 3.1 is the *numerical aperture* NA.

In the method suggested by Synge a strong light source is placed behind a thin, light-tight metal film with a small aperture of diameter d less than $100\,nm$ ($d \ll \lambda$). Fig. 3.6 shows the principle where a small light spot illuminates a thin specimen at height z below the aperture ($z \ll \lambda$). If the specimen is scanned in nanometre steps and the transmitted light is collected with a microscope lens and projected onto a phototube a optical signal of the specimen is collected. Thereby the resolution is limited by the size of the aperture not by the used wavelength λ [154].

In 1984 Pohl et al. [155] and Lewis et al. [156] presented the first optical near-field

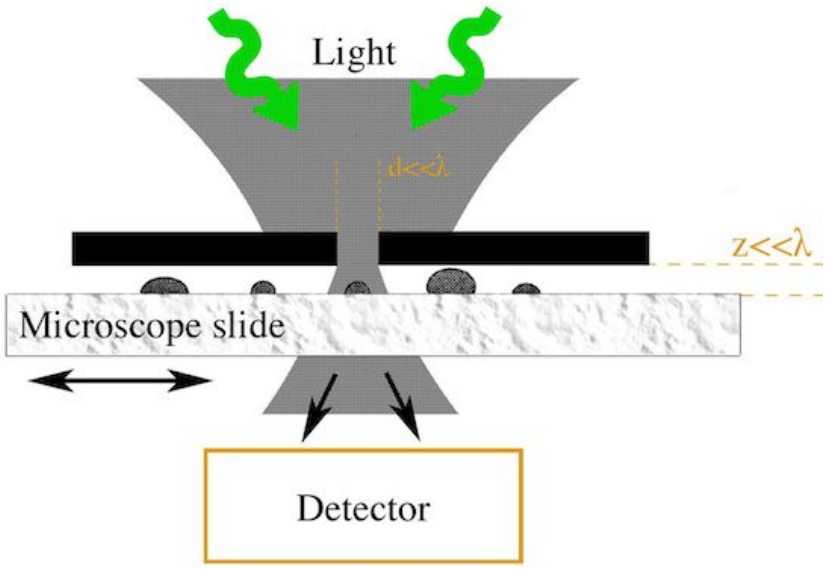

Figure 3.6: *Near-field microscopy proposed by Synge where a small aperture serves as a light source. Behind that is the screened specimen and the detector for the transmitted light. [153]*

microscopes which reached resolutions of $\lambda/20$ and $\lambda/16$ respectively. The main problem for this technique is the production of apertures smaller then the wavelength of light. To get around this problem Wessel introduced an aperture-less approach in 1985 [157]. In this approach, the near-field of a small, optically resonant particle serves as a local light source for the nanoscale specimen. The optical resonance is due to excitation of localized surface plasmons. The scattered light is detected in far-field and contains the information about the optical near-field interactions between the probe and the specimen. Due to Raman-scattering the wavelength of emission is different from the excitation in Wessel´s experiment.

Optical near-fields The propagation of light in a homogeneous, isotropic, linear and source-free medium is described by the *Helmholtz wave equation*, $(\nabla^2 + k^2)\, E(\vec{r}) = 0$ [158, 159]. Solutions to the Helmholtz equation are plane waves, which have the form

$$E(\mathbf{r}, t) = E_0 \mathrm{e}^{i\left(\vec{k}\cdot\vec{r} - \omega t\right)}. \tag{3.2}$$

Here, E_0 is the amplitude of the electric field, $\vec{k}$ is the wavevector ($|\vec{k}| = {}^{n\omega}/_{c}$), $\vec{r}$ the position vector, ω the angular frequency and t the time. n is the index of refraction which is given by $n = \sqrt{\epsilon_m \mu_m}$, where ϵ_m and μ_m are the relative permittivity and permeability of the medium in which the wave propagates, respectively. At optical frequencies and for non-magnetic materials $\mu_m = 1$ [158,160]. With the help of Fourier transformation, any space- and time-dependent wave can be described by a series of monochromatic plane waves (Eq.3.2), which is known as the angular spectrum representation [158,160]. The wavevector can be expanded into its components along the three space coordinates (x, y, z) according to $k^2 = k_x^2 + k_y^2 + k_z^2$. Neglecting the time dependence of Eq.(3.2), two well-defined situations can be distinguished for the propagation of light along a given direction z [158]:

- $k_x^2 + k_y^2 \leq k^2 \implies k_z$ is real. $\implies \mathsf{e}^{\pm i|k|\cdot z}$ is an oscillatory term and Eq.(3.2) describes a propagating plane wave in the z-direction.
- $k_x^2 + k_y^2 > k^2 \implies k_z$ is purely imaginary. $\implies \mathsf{e}^{-|k|\cdot z}$ describes an evanescent electromagnetic-wave decaying exponentially in the z-direction, which is also named the *evanescent near*-field.

Evanescent waves are characterized by the fact that at least one component of the wavevector $\vec{k}$ describing the direction of propagation is imaginary. In the spatial direction defined by the imaginary component of $\vec{k}$ the wave does not propagate but rather decays exponentially [160]. For distances far from the source ($z \gg \lambda$) and $k_x^2 + k_y^2 \leq k^2$ only propagating waves exist, whereas in the proximity ($z \ll \lambda$) of a small radiating object ($a \ll \lambda$) and $k_x^2 + k_y^2 > k^2$ there is an evanescent field as well. Evanescent fields cannot occur in an infinite homogeneous medium but are inevitably connected to the interaction of light with inhomogeneities. One such example of an inhomogeneity is an interface between two media characterized by different optical constants ϵ_1, μ_1 and ϵ_2, μ_2. Due to total internal reflection an evanescent wave is generated [160]. These near-field interactions can be detected with an optical near-field microscope where a small probe, brought close to the specimen, converts the evanescent fields into propagating fields, which can be detected in far-field [161].

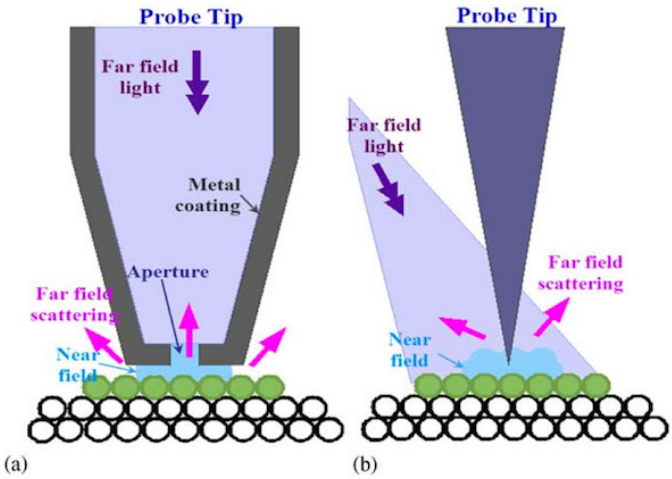

Figure 3.7: *Schematic comparison of:* ***(a)*** *aperture SNOM and* ***(b)*** *apertureless SNOM. [162]*

Principle of scattering-type Scanning Near-field Optical Microcopy (s-SNOM) Most methods used for scanning near field optical microscopy (SNOM) are based on scanning probe microscopy where a near-field probe is scanned over the sample surface. The most common SNOM technique exploits tiny apertures for imaging as shown in Fig. 3.7(a). These probes are mostly based on metal coated optical fibers with a tapered end and an aperture at the apex of the fiber [158, 162]. The size of the aperture is typically greater than $50\,nm$ and is the limiting factor in resolution. Furthermore the propagation of light in the coated fiber is similar to the transport of electromagnetic waves in hollow metal waveguides and therefore decays exponentially when the diameter of the probe becomes smaller than $\lambda/2$ (cut-off), because the wavevector of the propagating mode becomes imaginary. Knoll and Keilmann showed that the transmission for infrared light ($\lambda \approx 10\,\mu m$) and an aperture diameter of $100\,nm$ the transmission is reduced by 10^{-25} [158, 163].

Aperture based near-field microscopy at infrared wavelengths, used to analyze chemical properties of nanophase materials, cannot be used to gather information with a spatial resolution not better than approximately $> \lambda/10 \approx 1 - 2\,\mu m$ [158]. In order to circumvent the restrictions in wavelength with aperture probes, thus gaining the ability to use longer wavelength infrared light, apertureless probes can be used [164]. The principle is shown in Fig. 3.7(b). Based on an atomic force microscope (AFM)

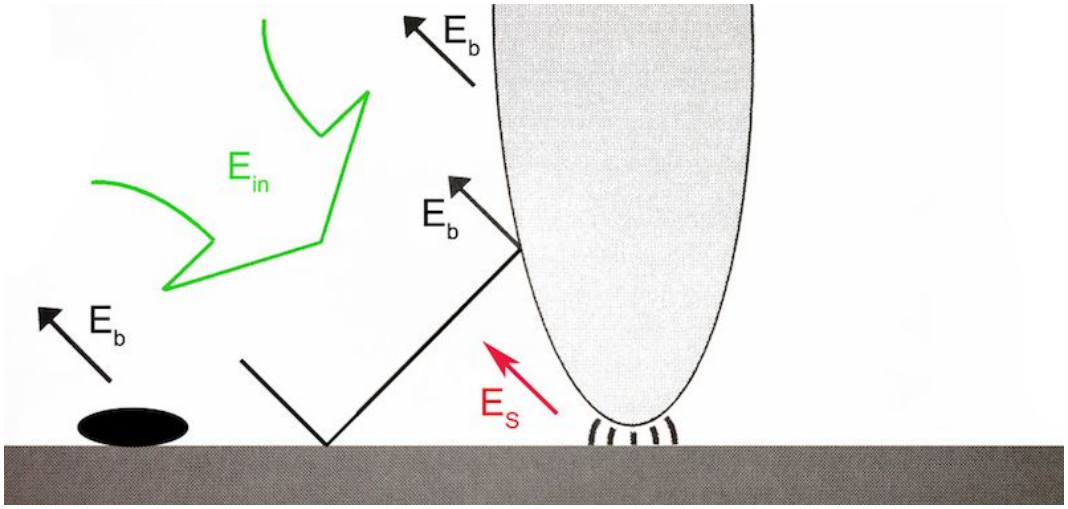

Figure 3.8: *Distinction of different sources of near-field signals. The signal can contain background E_b from different sources as well as the signal of the specimen E_S [161].*

a s-SNOM gives, first of all, a topographical image of the sample. A mid-infrared laser beam is focused onto the tip by an objective lens which creates a diffraction limited focus on the sharp metal tip. The small probe, with an apex-radius of a, functions as an optical antenna, concentrating the incoming light at its apex to a small spot of only few nanometres, which is used as a nanoscopic light source to illuminate the sample [158]. This rests on the fact that an illuminated small metal particle or sharp tip-like metal structure can exhibit enhanced optical fields in its neighbourhood when illuminated by light [158, 160]. If the tip is brought close to the sample surface, the highly convergent electric field at the apex interacts optically with the sample. Because of the optical near-field interactions between the metallic [157, 165] or dielectric [166] tip and the sample, the light scattered from the tip contains information about the local optical properties (e. g. refractive index) with a resolution of about $10nm$ [158, 167, 168]. The light backscattered from the tip can be recorded by a distant detector. With this method it is, in principle, possible to use any wavelength without losing resolution because neither an aperture nor an waveguide is used [164]. Hence the resolution is only limited by the geometrical size of the tip [161, 164, 165]. However, one challenge of s-SNOM is that there is also a strong background signal. In addition to the scattered light from the tip (E_s in Fig. 3.8), scattered light from the cantilever, the tip shaft, or from other features on

the sample is also detected (E_b in Fig. 3.8). To enhance the signal to noise ratio the near-field signal is modulated by varying the distance between the tip and the sample [153]. Therefore the tip is oscillated with a frequency Ω and an amplitude A ($A \ll \lambda$) resulting in the near field being modulated with the same frequency Ω. Using the higher harmonic frequencies of the signal $n \cdot \Omega$ ($n > 1$) allows supression of the background signal [153, 158, 161]. The demodulation process relies on the fact that the near-field interaction depends in a non-linear manner on the distance between the tip and the sample [153].

Theory of s-SNOM The crucial factors in SNOM measurements are the relative signal change, which results when probing different materials, and the absolute scattering efficiency, which determines the observable signal power [169]. To determine the latter, the scattering cross section W_{sca} has to be calculated. For a small sphere this is the integral of the Poynting vector over the field of the solid angle of the detector. By computing the integral over all solid angles the total scattering cross section $C_{sca} = W_{sca}/I_{inc}$ can be derived, normalized to the intensity of the incident field [161]. For a spherical particle with diameter a at Rayleigh-limit [161]:

$$C_{sca} = \frac{8\pi}{3} k^4 a^6 \left| \frac{\epsilon - \epsilon_m}{\epsilon + 2\epsilon_m} \right|^2 = \frac{k^4}{6\pi} |\alpha|^2 , \tag{3.3}$$

where k is the wavevector, ϵ is the absolute permittivity, ϵ_m is the relative permittivity of the material, and α is the polarizability.

As a first approximation in analytical models the point-dipole model is used. As shown in Fig. 3.9 the tip of the SNOM is reduced in this model to a small metal sphere of radius R, placed at a height $z = R + h$ above the specimen. In order to calculate the scattering cross section the effective polarizability $\alpha_{eff,z}$ in z-direction (schematically shown in Fig. 3.9(a)) is needed. It can be given as [170]

$$\alpha_{eff,z} = \frac{\alpha(1+\beta)}{1 - \frac{\alpha\beta}{16\pi(R+h)^3}}, \tag{3.4}$$

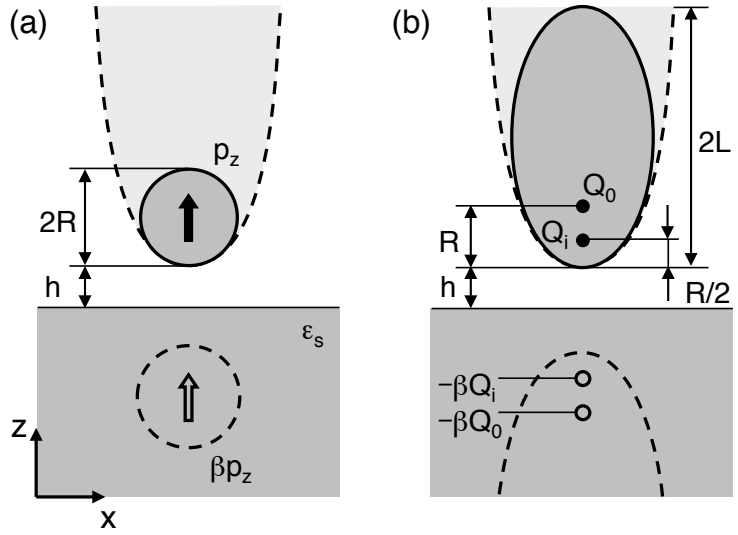

Figure 3.9: *Comparison of typical s-SNOM models.* ***(a)*** *Point-dipole model used for analytical models where the tip is reduced to a dipole.* ***(b)*** *Finite-dipole model where a sphereoid is used for approximation. [158]*

where $\beta = \frac{\epsilon_s - 1}{\epsilon_s + 1}$ is the surface response function of the sample with ϵ_s being the relative permittivity of the sample [158]. In order to achieve quantitative agreement between experiment and theory this model had to be refined. Cvitovic et al. and Ocelic et al. showed that refining the tips geometry to a prolate spheroid with semi-major axis length L (shown in Fig. 3.9(b)) is in agreement with the measurements, as the calculated field in the vicinity of a spheroid is similar to the field of an extended or finite, and not a point-like, dipole [170,171]. For the finite dipole the polarizability can be given as [170,171]

$$\alpha_{eff} = R^2 L \frac{\frac{2L}{R} + ln\frac{R}{4eL}}{ln\frac{4L}{e^2}} \left(2 + \frac{\beta\left(g - \frac{R+h}{L}\right) ln\frac{4L}{4h+3R}}{ln(4L/R) - \beta\left(g - \frac{3R+4h}{4L}\right) ln\frac{2L}{2h+R}} \right). \tag{3.5}$$

Five independent parameters are needed to solve Eq. 3.5. Operating the AFM in tapping mode, the tip vibrates vertically, giving the tip / sample separation h, with an amplitude of about 55 nm at a frequency of $\Omega \approx 250\,kHz$. The tip radius R ($\sim 40nm$) is specified by the manufacturer. The parameters of the effective spheroid L and complex factor g are empirical parameters, which have been derived from

phenomenological comparison between experiment and theory in previous work. Detailed information can be found in [158, 161, 170, 171].

The s-SNOM experiments in this work were carried out at NEASPEC GmbH and the NanoPhotonics group CIC02 at nanoGUNE in San Sebastian, Spain. The first experiment was imaging of a printed layer from top with a commercial available instrument at NEASPEC. For this experiment no special steps had been made. The specimen, prints of silicon nanoparticles produced by high energy milling (p-type wafer ($\rho < 0.005\,\Omega cm$, 90min milled)), were printed as described in section 3.1.3 on a silicon wafer as substrate. For the second experiment, powder was milled from p-type wafer ($\rho < 0.005\,\Omega cm$, 90min HE-milled) and cross sections of layers printed on silicon wafer substrates were studied. Due to the high porosity of the printed layers, the samples were embedded in resin (EPO-FIX embedding resin, EMS Hatfield USA) in order to stabilize the nanoparticle layer during the polishing process. Before embedding, two layers were cut with a diamond saw and put together facing each other. To ensure a low viscosity and penetration into all cavities of the printed layer, the resin was heated to $\sim 50\,°C$ and exposed to vacuum 5 times repeatedly. After that, the layer was allowed to dry for 24 hours before being polished mechanically, instead of using the focused ion beam. The cross sections were mechanically polished in order to prevent contamination of the silicon nanoparticles with the gallium beam used with FIB. An optical micrograph of the specimen used is shown in Fig. 3.10. The samples used for both s-SNOM experiments were layers, printed on wafers ($\rho = 1 - 10\,\Omega cm$) as a substrate. As described above the AFM operates in intermittent contact mode where the tip oscillates perpendicularly to the sample surface (z-direction) at its resonance frequency of $\Omega \approx 250\,kHz$ with an amplitude $A \approx 55nm$. Piezo actuators control the position of the tip, using a feedback loop in order to keep the tapping amplitude constant. The measurements were carried out with a tunable mid-infrared CO_2 laser between $k = 936\,cm^{-1}$ and $k = 1069\,cm^{-1}$ ($\lambda = 10.68 - 9.35\,\mu m$) measured by grating spectrometer. For interferometric detection of the light backscattered from the tip, a Michelson interferometer, based on a ZnS beamsplitter (Fig. 3.11), is employed. Light transmitted by the beam splitter is focused onto the AFM tip by a parabolic mirror with a numerical aperture of approximately 0.5. The same

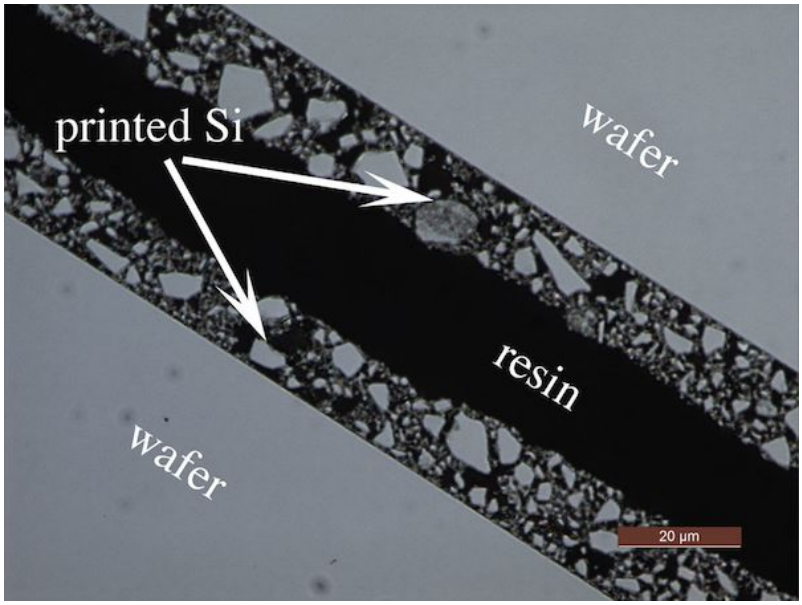

Figure 3.10: *Optical micrograph of the set-up of the sample used for s-SNOM. Two layers of printed silicon on a Si wafer substrate were put together with the prints facing each other.*

mirror is used to collect the backscattered light as shown schematically in Fig. 3.11. The collected light interferes with the reference beam obtained from the reflected light of the beam splitter. The detector used to detect the interference field between the backscattered light and the reference beam is a Mercury Cadmium Telluride (MCT) detector. The near-field images are obtained by scanning the sample below the probing tip and recording the backscattered light simultaneously with the topography. A visible laser can be overlapped with the CO_2 laser for alignment purposes [158].

3.2.4 Raman spectroscopy

As with other optical spectroscopy techniques, Raman spectroscopy can be applied non-invasively under ambient conditions in almost every environment [172]. In the Raman effect, incident light is inelastically scattered from a sample and shifted in frequency by the energy of its characteristic phonon frequencies vibrations. Since its discovery in 1927, the effect has attracted attention from a basic research point of view as well as a powerful spectroscopic technique with many practical applications [172]. For this study, a WITEC alpha 300 AR raman spectroscopy system was used under

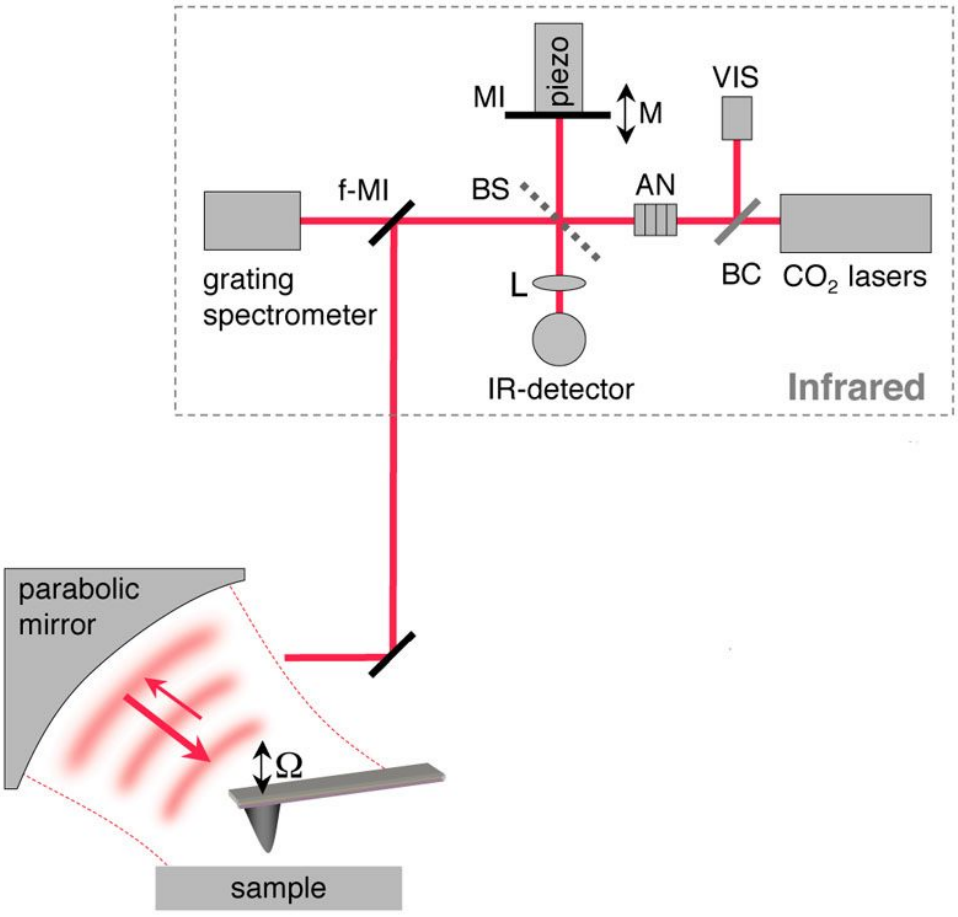

Figure 3.11: *Schematic configuration of the s-SNOM used for this work. Mid-infrared CO_2 laser, BS – beam splitter; AN – attenuator; BC – beam combiner (e.g. ITO glas slide); VIS – visible laser for adjustment; (f-)MI – (flipable-)mirror; L – lens. [158]*

ambient conditions, to investigate layers printed from acrylic ink (90 minute milled p-type wafer, $\rho < 0.005\,\Omega cm$) on paper substrate. The alpha 300 AR is equipped with an UHTS spectrometer, and an IDUS-CCD camera (width 1024 pixels, height 127 pixels and full vertical binning read mode). For excitation a frequency doubled NdYAG laser with 532nm was used.

3.3 3-D reconstruction of printed layers

For the tomographic reconstruction of a printed layer, a series of SEM images prepared using a FIB-SEM was used. The series was obtained by slicing a a fully printed diode. For stability during the cutting, the diode was embedded in EPO-FIX embedding resin (Electron Microscopy Sciences, Hatfield, PA, USA), as described previously. The resin was allowed to cure for 24 hours before the experiment was carried out. The instrument used (FEI Helious NanoLab^{TM}DualBeam^{TM} FIB/SEM) was aligned to cut slices of the printed diode with a thickness of abround 11 nm using 24 pA beam current at an accelerating potential of 30 kV. Overall 618 slices were cut to collect data for a volume of about $6 \times 6 \times 6\,\mu m^3$. The 3-D tomogram was reconstructed from -75 to $+75$ degrees image series by SIRT algorithm using the Insepct3D software (FEI Co, Netherlands) at CIC nanoGUNE, Spain. Subsequently the tomogram was visualised in UCSF Chimera version 1.8, a freely available computer software package [173, 174].

3.4 Electrical characterization of fully printed diodes

The electrical characterization of the printed diodes was carried out using a Keithley 4200 semiconductor characterization system (SCS). The instrument was used to determine the current versus voltage characteristic of the printed diodes at room temperature. Used with a double Faraday cage, to prevent electronic noise or interferences from nearby electrical systems, this system enables high accuracy measurements with a current and voltage resolution of 1 pA and 2 μV respectively, using two source measurement units (SMU). The enclosed double Faraday cage also serves as a shield for any source of light that may result in photo induced conduction [108]. For DC I-V measurements, the 4200 SCS Source Measure Unit (SMU) was connected to the bottom electrical contact of the diodes while the ground unit (GNDU) of the system is connected to the top electrical contact. The connections

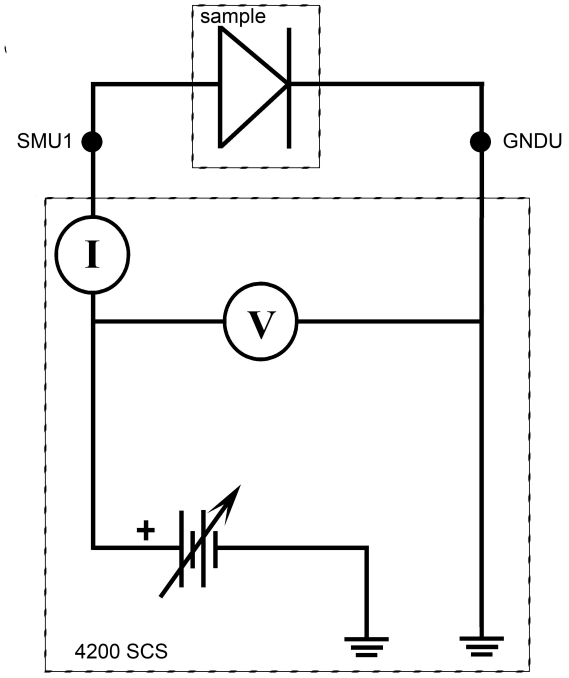

Figure 3.12: *Equivalent circuitof the SCS set-up used for I-V characterisation.*

were then tested with a digital multimeter to check the continuity between the printed devices and the electrodes. Figure 3.12(a) shows the equivalent electrical circuit used to carry out the I-V measurements. The SCS was set to sweep the source through a voltage range of either -20 V to +20 V, -15 V to 15 V, -10 V to +10 V or -5 V to +5 V with steps of 0.2 V, 0.15 V, 0.1 V or 0.5 V respectively. A hold time of 5 seconds and sweep delay of 100 milli seconds was set to allow for current settling after each sweep. The measurements were carried out under ambient laboratory conditions.

4 Morphology and internal structure of silicon nanoparticles

In previous work it has been shown that the charge transport in a printed silicon nanoparticulate system is limited by the properties of the interface between the particles and is best described as a hopping percolation transport [109]. Hence, in order to understand the observed charge transport through the percolative network of printed silicon nanoparticles, the particles themselves were investigated before printing. In this chapter the focus was on the investigation of the surface of the particles produced by high energy milling (as described in chapter 3.1.1). This helped to provide a baseline for similar studies for particles in printed layers to investigate whether there was a change in oxidation state and clustering of the particles during the ink making and printing processes described later in chapter 5.

4.1 Scanning electron microscopy (SEM) and focused ion beam (FIB) on Si-NP

The particles investigated were produced with high energy milling as described in chapter 3.1.1. Using this technique and the same milling regime, nanoparticles with a log-normal size distribution with a median of around $100\,nm$ were produced [38]. Newer measurements using ultra-small-angle X-ray scattering(USAXS), also suggest a similar particle size of about $80\,nm$ [93,110]. Hence the milled nanoparticles are large enough to prevent size-related (e.g. quantum) electron confinement [175,176], wich enables charge transport between particles. Figure 4.1(a) shows a low magnification image of n-type silicon particles drop-cast onto a silicon wafer (see section 3.2.1).

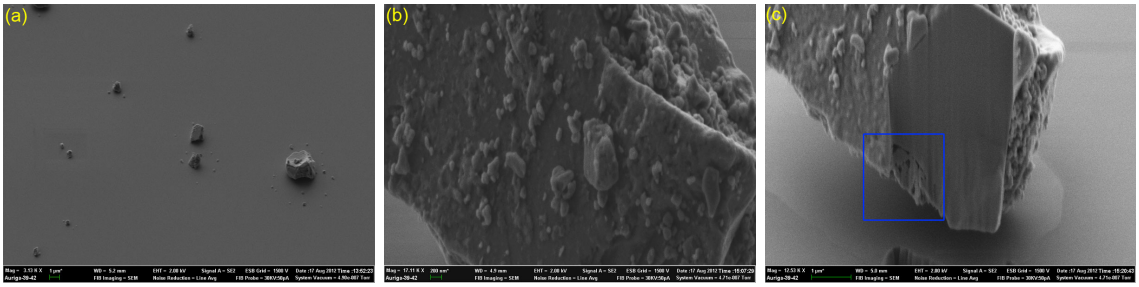

Figure 4.1: ***(a)*** *drop-cast n-type Si-NP on a polished wafer.* ***(b)*** *higher magnification of a large particle, showing that the surface of the particle is covered with small nanoparticles, and* ***(c)*** *focused ion beam section showing that large particles show an internal structure.*

Particles with sizes from the nanometre scale up to a few micrometers can be seen. A higher magnification of a particle is shown in Fig. 4.1(b), revealing that some of the milled particles are covered with clusters of very small nanoparticles on their surfaces. This feature has not only been seen on particles drop-cast but was also observed in micrographs of particles in the dry powder which has not been in solution before. Even after dispersion in methanol the particles form loosely aggregated small clusters, which in turn are grouped together at different positions on the wafer.
In order to investigate whether the large particles have an internal structure, a focused ion beam study was performed. Fig. 4.1(c) shows a section of the particle shown in Fig. 4.1(b). The particle clearly shows an internal structure near the surface of the particle (blue square). The observed structure inside the particle can be explained if the particles form large clusters of nanoparticles after or during the milling process as the used feedstock for the milling process was monocrystalline. This internal structure could be observed with most particles that were cut with FIB. Therefore it can be concluded that the powder feedstock used for ink preparation contains nanoparticles as well as clusters of nanoparticles with sizes up to a few micrometres.

4.2 High resolution transmission electron microscopy (HRTEM) on Si-NP

A series of HRTEM micrographs of 5hr milled n-type silicon is shown in Fig. 4.2. The micrographs were taken from powder, drop-cast onto a carbon coated holey grid, using the TEAM 0.5 [177, 178] instrument with a $80\,kV$ electron beam (see chapter 3.2.1). The measurements were performed approximately six months after the particles were milled. Figure 4.2(a) shows a large area TEM image of silicon nanoparticles produced by high energy milling. It can be clearly seen that the particles form clusters (Fig. 4.2(a)), and in the image overlap by a large extent (Fig. 4.2(b)). However, in these micrographs it is possible to determine the exact boundary of the individual particles making up the cluster (Fig. 4.2(c)), unlike in previous lower resolution studies [108, 109]. The morphology of the particles is similar to

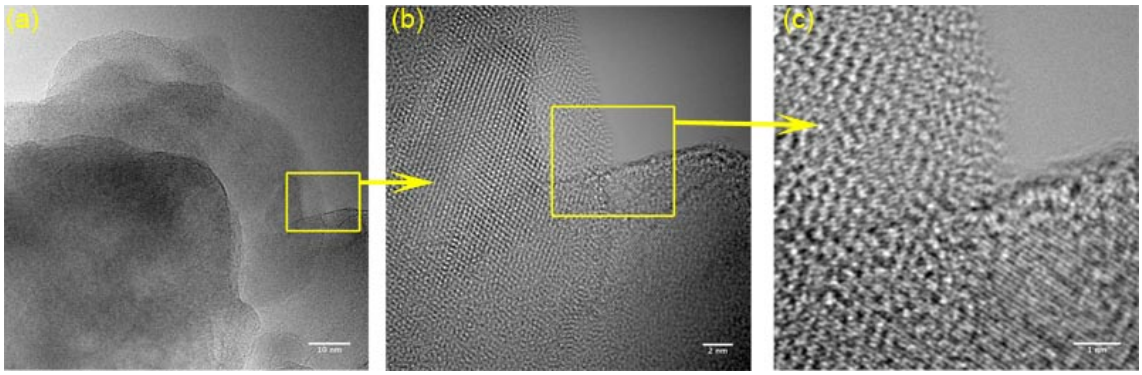

Figure 4.2: *Series of HRTEM micrograph with increasing magnification, taken approximately six month after the particle production.* ***(a)*** *low magnification TEM image of a group of small clusters of silicon nanoparticles.* ***(b)*** *TEM micrograph showing the boundary of individual particles making up a cluster, and* ***(c)*** *HRTEM image of an overlay of a large crystal (lower) and a particle (left).*

that previously reported for metallurgical silicon nanoparticles, with most particles being irregularly faceted and slightly prolate [36, 110]. The particles form loosely aggregated small clusters, which in turn are grouped together at different positions on the TEM grid, often forming an extended network.

Previous work on silicon nanoparticles showed that the particles have no capping layer [36–38], with the majority of the surfaces being <111> or <100> faces. How-

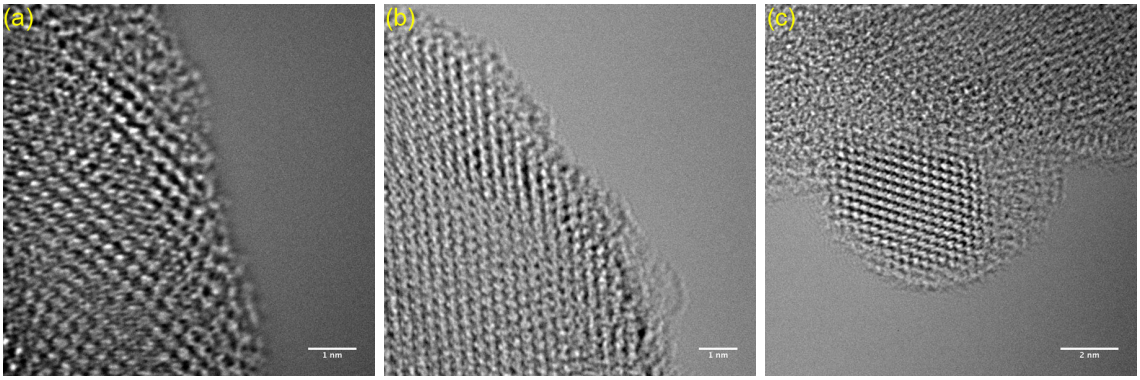

Figure 4.3: *HRTEM micrographs of grains showing the near surface area of* ***(a)*** *<100> lattice plane extending almost to the surface of the paticle,* ***(b)*** *surface region of a silicon nanoparticle with <111> lattice orientation, and* ***(c)*** *silicon nanoparticle with a size of around 10nm.*

ever, islands of a disordered surface regions were seen near edges. These aspects have been further investigated in this work using an instrument with a much better point-to-point resolution as well as reduced delocalization (see 3.2.1).

A high resolution image of the near surface region of a single particle, shown in figure 4.3(a), clearly shows the <100> silicon lattice planes extending almost to the surface of the particle, without indication of a thick disordered surface layer. However, the image shows that the particle has a thin disordered surface layer with a thickness of about two atomic layers ($< 5\,\text{Å}$) on its surface. Figure 4.3(b) shows the near surface region of a silicon nanoparticle with <111> lattice orientation. This micrograph also shows a thin amorphous layer outside the disordered layer on its surface. The same features are seen with much smaller particles as shown in Fig. 4.3(c).

Although this thin surface layer might be a natural silicon oxide, it is also possible that it is a carbon phase originating from the sample preparation. A similar lack of oxidation has also recently been seen in smaller <111> faceted silicon nanoparticles produced by hot wire chemical vapour synthesis [79]. To compliment the data obtained from the HRTEM micrographs X-ray photoelectron spectroscopy has been carried out.

In previous studies, investigation of the Si 2p X-ray photoelectron emission shows predominantly Si^{2+} oxidation states and low intensity emission from the Si^{4+} oxidation state [143]. If all the Si is in its 4^+ oxidation state, due to the presence

of a uniform stoichiometric oxide layer, for excitation with Al Kα X-rays and an exponential escape probability for the photoelectrons [179], the thickness of this layer can be estimated to be $0.35 \pm 0.1\,nm$ [143]. This thickness corresponds to less than one monolayer of stoichiometric oxide and is in good agreement with earlier estimates based on a determination of the total oxygen concentration [35]. This applies to all investigated nanoparticles, irrespective of the used feedstock.
In the above it has been shown that for high energy milled particles of different feedstock, but using the same milling regime, the surface is likely to be not completely devoid of oxygen but contains the equivalent of nearly a monolayer of SiO [143]. Energy transfer in the milling process not only breaks the particles into smaller units, but during milling firstly strain as well as dislocations and subsequently grain boundaries are introduced into the crystal structure. There is, however, no indication of amorphisation, and hence within the particles charge transport is expected to be equivalent to that in crystalline silicon [39].

4.3 Elemental mapping of silicon nanoparticles

For this study HAADF STEM images were obtained using a FEI Titan 60-300 electron microscope operated in STEM spectral imaging mode at the electron microscopy laboratory at CIC nanoGUNE in San Sebastian, Spain. Fig. 4.4 shows a drift corrected STEM image of particles drop-cast onto a holey grid (n-type Si-NP, $\rho < 0.001\,\Omega cm$, milled for 5hr). Elemental mapping was performed using Energy-dispersive X-ray spectroscopy (EDX).
A large area STEM image of the drop-cast particles is shown in Fig. 4.4(a). The shadowing visible in this image shows, that particles are clusters or that they are overlapping. However, in this 2-D representation a conclusive interpretation is not possible. Elemental maps of the zoomed area, marked with the rectangle in Fig. 4.4(a), are shown in Fig. 4.4(b) and Fig. 4.4(c) respectively. The orange colour in Fig. 4.4(b) represents the oxygen content, whereas green in Fig.4.4(c) shows the silicon distribution.
The elemental maps shown in the figures reveal that there is only an incomplete

layer of oxygen (orange) on top of the silicon nanoparticles (green). Furthermore the elemental analysis shows, that the oxygen layer is fairly thin. However it can be seen that an small area shows a thick oxygen layer (arrow in Fig. 4.4(b)). This is in good agreement with the HRTEM micrographs shown above which revealed that there is no thick, continous oxide layer but only a thin disordered surface layer, and some small islands of disordered surface regions (see chapter 4.2) on the particles investigated.

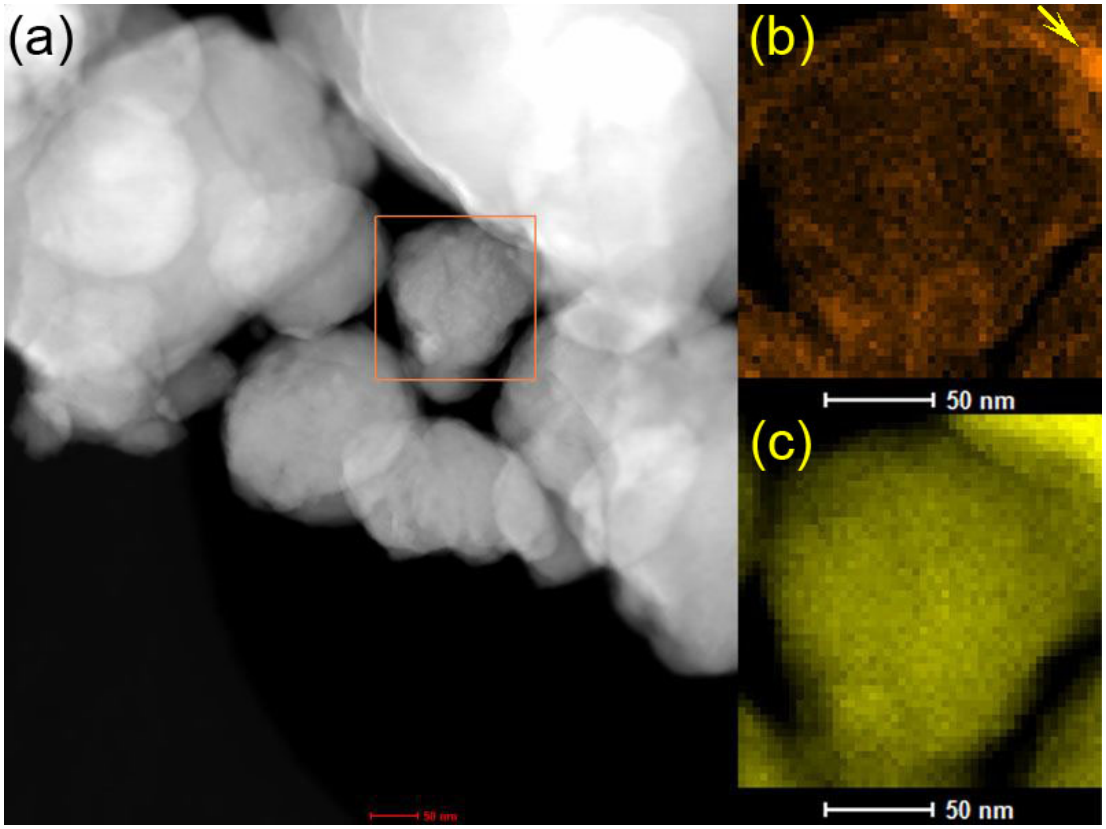

Figure 4.4: ***(a)*** *large area STEM image of silicon nanoparticles, and elemental maps of the zoomed area marked with the rectangle of* ***(b)*** *oxygen, and* ***(c)*** *silicon.*

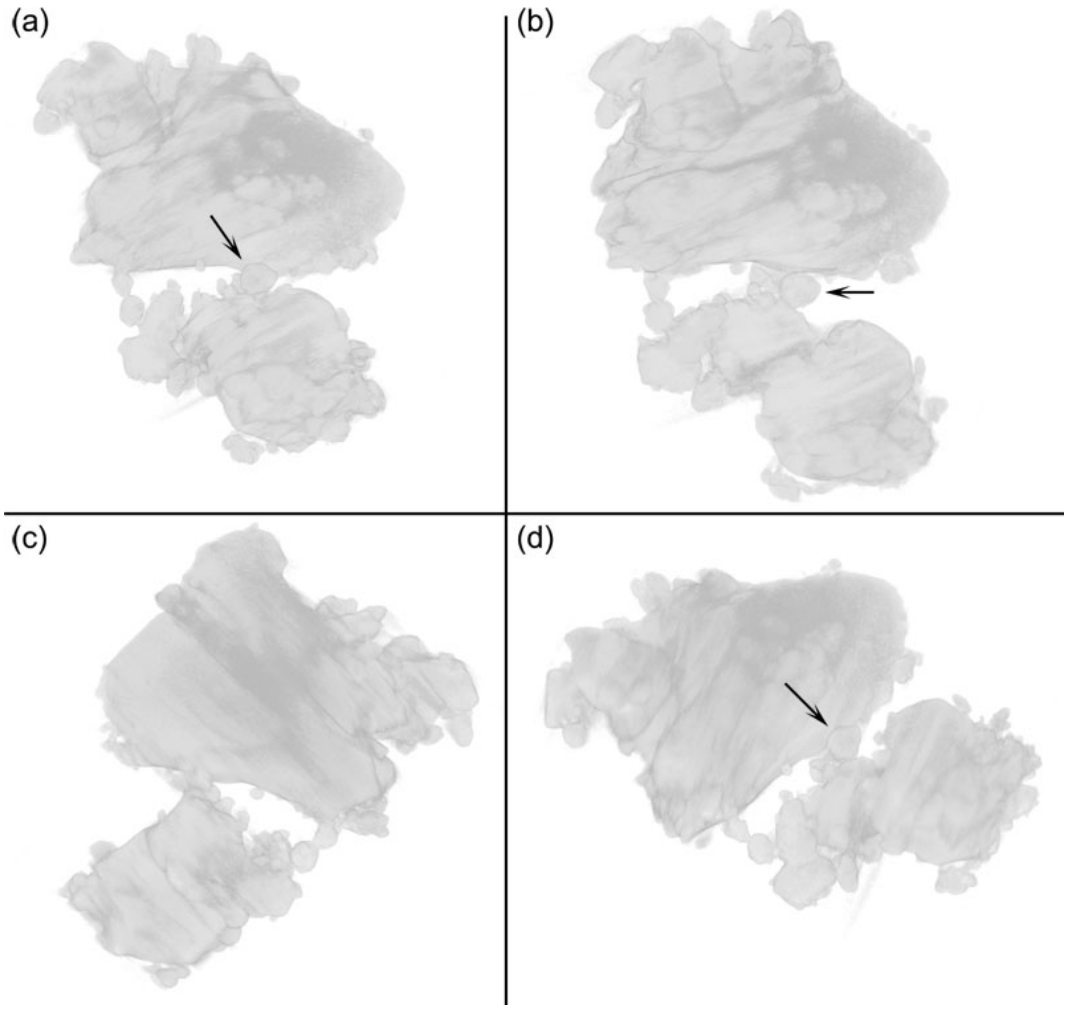

Figure 4.5: *3-D tomograms of 5hr milled silicon nanoparticles*

4.4 3-D tomogram of silicon nanoparticles

In order to reveal the shape and connectivity of the silicon nanoparticles, 3-D tomograms were reconstructed from TEM images as decribed in chapter 3.3. Fig. 4.5 shows different views of a tomogram produced from TEM images of the same area, used for elemental mapping discussed in chapter 4.3 above. One particle is marked with an an arrow for reference between the images. This particle is not visible in Fig. 4.5(c).

It can be seen that the particles have a disperse size distribution and form agglomerates of particles with different sizes, which is in good agreement with the size

distribution expected from particles produced by high energy milling and micrographs shown above. Furthermore the tomogram reveals that the particles have surfaces with relatively smooth facets and good connectivity. These characteristics are important features the particles need to form a percolative path when used as the active material in a screen printable ink discussed later in this thesis.
In comparison to the features seen in the STEM images shown above in chapter 4.3, it can be seen that the particles form chain-like networks of particles, what is not possible to distinguish in a two dimensional projection. Furthermore it can be seen that small particles are attached to the surfaces of larger particles which is in good agreement with the TEM study presented later in this thesis.

5 Morphology and internal structure of printed silicon nanoparticulate networks

In the previous chapter the microstructure of silicon nanoparticles, produced with high energy milling was discussed. In this chapter the microstructure of printed silicon nanoparticulate networks will be presented. Firstly, an overview of the printed layers using scanning electron microscopy (SEM) is shown, followed by an investigation of printed networks using electron microscopy combined with mechanical cross sectioning. In order to obtain a more detailed picture of the interfacial and network characteristics of the printed layer a rigorous high resolution transmission electron microscopy (HRTEM) study was performed on a cross-sectioned lamella. This lamella was prepared using focused ion beam (FIB) milling as described in chapter 3.2.2. This HRTEM study helped to provide a more detailed information about the interfacial and network characteristics of the printed layers. Information obtained by electron microscopy is supported by Raman spectroscopy, and preliminary mid-infrared scattering type near field optical microscopy (IR s-SNOM) studies are discussed at the end of this chapter.

5.1 Scanning electron microscopy

As previously demonstrated, high energy milled particles were used to formulate an aqueous ink [37, 38, 109]. In addition to the water-based ink printed, solvent-based inks printed on paper are also investigated in this thesis [143]. Screen printing

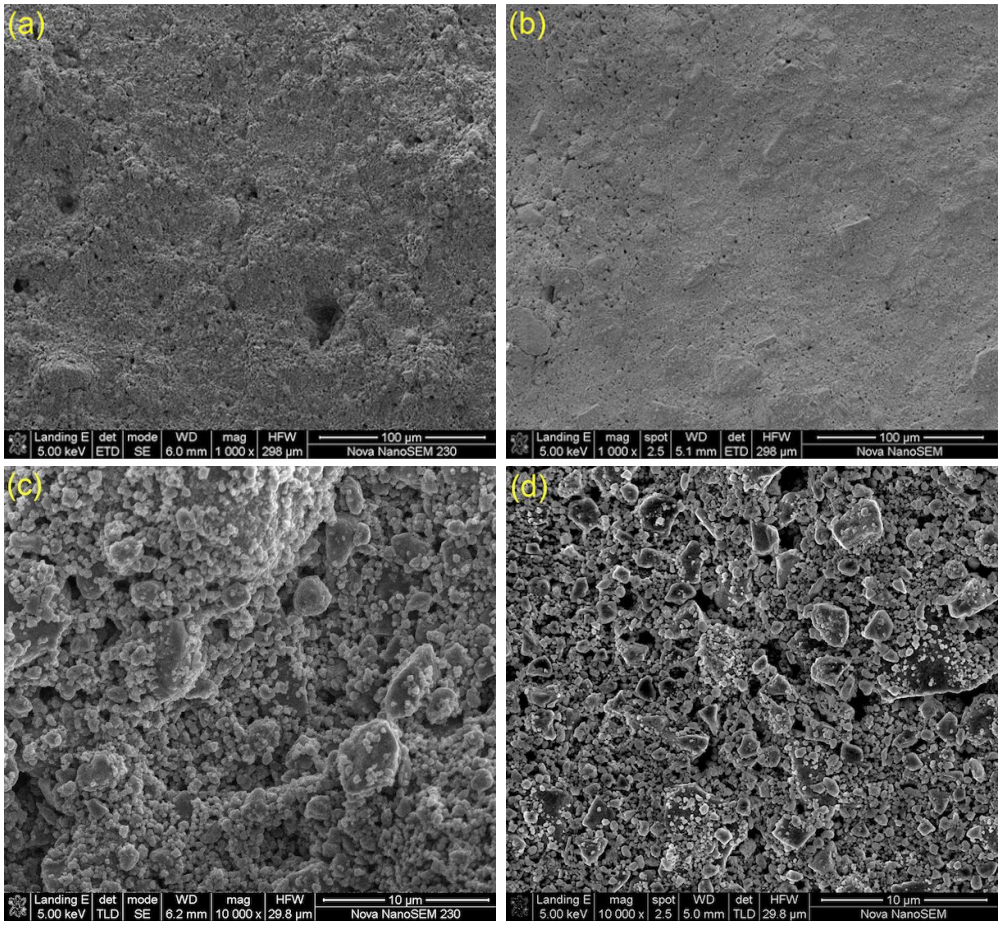

Figure 5.1: *Low magnification surface view SEM micrograph of a printed silicon layer* ***(a)*** *printed with water-based ink with acrylic binder, and* ***(b)*** *solvent-based ink using ethyl cellulose as a binder.* ***(c)*** *shows a higher magnification micrograph of the layer shown in* ***(a)****, and* ***(d)*** *shows a higher magnification micrograph of the layer shown in* ***(b)****.*

these semiconducting silicon layers avoids complex semiconductor processing and post-processing steps such as thermal annealing. In Fig. 5.1 top-view micrographs show the typical features of water based and solvent based inks, using n-type silicon ($\rho = 0.008 - 0.02\,\Omega cm$, milled for 5hr). Fig. 5.1(a) and (b) show low magnification images of layers printed with the two different binders used. It can be seen that both printed layers have rough surfaces, and that both printed layers are highly porous. The surface of the layer printed with water-based ink (Fig. 5.1(a)) has a small number of large pinholes. In contrast, the layer printed with solvent based ink ((Fig. 5.1(b))) generally has smaller pinholes but they are much higher in number.

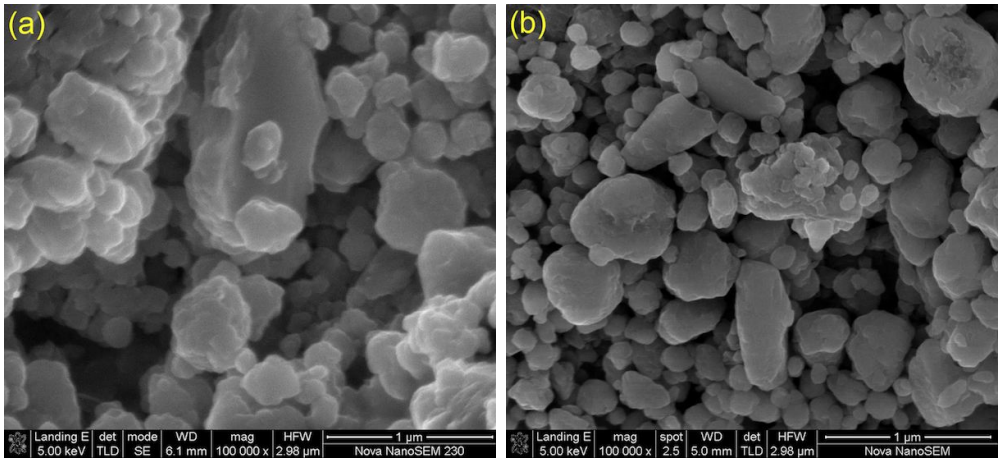

Figure 5.2: ***(a)*** *high magnification micrograph of a layer printed with a water based ink, and* ***(b)*** *ethyl cellulose based ink.*

The higher magnification micrographs of layers printed with water-based ink (Fig. 5.1(c)) and with solvent based ink (Fig. 5.1(d)) respectively reveal that the printed layers also exhibit roughness on a smaller scale. In these micrographs it is difficult to distinguish individual particles. However, it can be seen that both inks form layers of interlocking clusters with sizes up to a few micrometres. In the micrographs the layer deposited from water-based ink appears to show a higher packing density than that printed with the solvent based ink.

Fig. 5.2 shows higher magnification SEM micrographs of the silicon layers. Similar features can be observed for both the layer printed with water-based ink (Fig. 5.2(a)) and solvent-based ink (Fig. 5.2(b)). Here small particles with sizes down to less than 50nm can be observed. Furthermore it can be seen that the small particles form interlocking clusters and a self similar web of clusters. The micrograph also shows the high porosity and generally low packing density of the printed layer at a very small scale.

It is obvious from the above observations, that microscopy of the surface alone does not provide full information of the printed layers. To investigate the microscopic features and the internal structure of the printed semiconductor layer a cross-sectional view of the layers is necessary. As a first approach this was carried out with silicon layers printed on paper using 80% particle loading by relative weight for both types of inks.

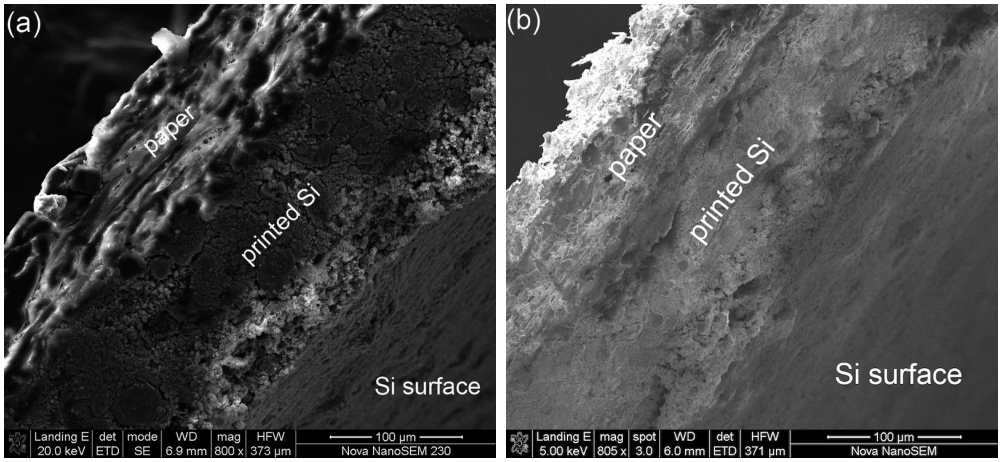

Figure 5.3: *SEM micrographs of printed silicon cross sectional cuts on paper substrate.* ***(a)*** *in water based, and* ***(b)*** *in solvent based binder.*

By simply cutting printed layers with a sharp blade, without embedding them in resin, possible dissolving of the printed layer due to the solvent of the resin is prevented. Fig 5.3 shows micrographs of the cross-section of the layers printed with water-based ink (Fig. 5.3(a)) and solvent-based ink (Fig. 5.3(b)). These micrographs also reveal that there is no significant difference noticeable in the microstructure of the layers produced with these two binder systems at this magnification. The thickness of the layers was seen to be of the order of $25 \pm 10\,\mu m$ which is in good agreement with previously reported thickness of printed silicon layers using metallurgical grade silicon [109].
The micrographs again show the formation of the interlocking clusters, which is one requirement for charge transport, as these are the structures which form a percolation network. On the other hand the micrographs in Fig. 5.3 also show the porosity of the layer. Due to the tearing forces involved during sample preparation, some features of the sample might have been damaged which makes it necessary to investigate the cross-sectional views with another technique at a higher magnification.

The micrographs shown above clearly reveal that the printed layers are highly porous. The non-uniformity of the surface seen in the low magnification micrographs is probably a result of the mesh pattern of the screen used for printing, and the thixotropic behaviour of the ink. This is in good agreement with previously reported

work for layers also printed with silicon inks using water-based binder [109]. The low scale roughness as well as the porosity and low packing density of the print observed in the higher magnification micrographs can be explained by the disperse particle size distribution which is a result of the production process of the silicon nanoparticles (see chapter 3.1.1). It was shown with cross section micrographs, that layers printed from silicon ink with a particle concentration of 80% showed excellent layer integrity and mechanical stability.
All results presented here are also in close agreement with results obtained in previous works for layers printed with metallurgical grade silicon inks showing that the formation and macro scale features of printed silicon layers are independent of silicon feedstock and the binder system used [108, 109].

5.2 High resolution transmission electron microscopy of interfacial and network characteristics of printed silicon

To investigate the microscopic as well as the mesoscale features of printed silicon layers a cross sectional study was performed on thin slices of printed layers, produced with a FIB/SEM as described in chapter 3.2.2. Fig. 5.4 shows a lamella cut from a printed layer with an ink, containing 80% silicon particle (p-type, $\rho < 0.005\,\Omega cm$) loading by relative weight. The TEM images shown below were obtained using a FEI Titan 60-300 electron microscope equipped with imaging Cs-corrector at 300 keV beam energy at the electron microscopy laboratory at CIC nanoGUNE in San Sebastian, Spain. The TEM image taken at a relatively low resolution shown in Fig. 5.4 reveals the overall structure of the printed layer. Three distinctive regions can be clearly seen: (**I**) in Fig. 5.4 shows the silicon wafer used as substrate. Here the contrast with dark contours (marked with red arrows) is due to bending of the lamella. (**II**) shows the printed layer and (**III**) shows the diamond membrane used to cover the printed layer and prevent damage to the lamella during preparation, as well as a region of the Pt filling used to stabilize the lamella. The inhomogeneity of

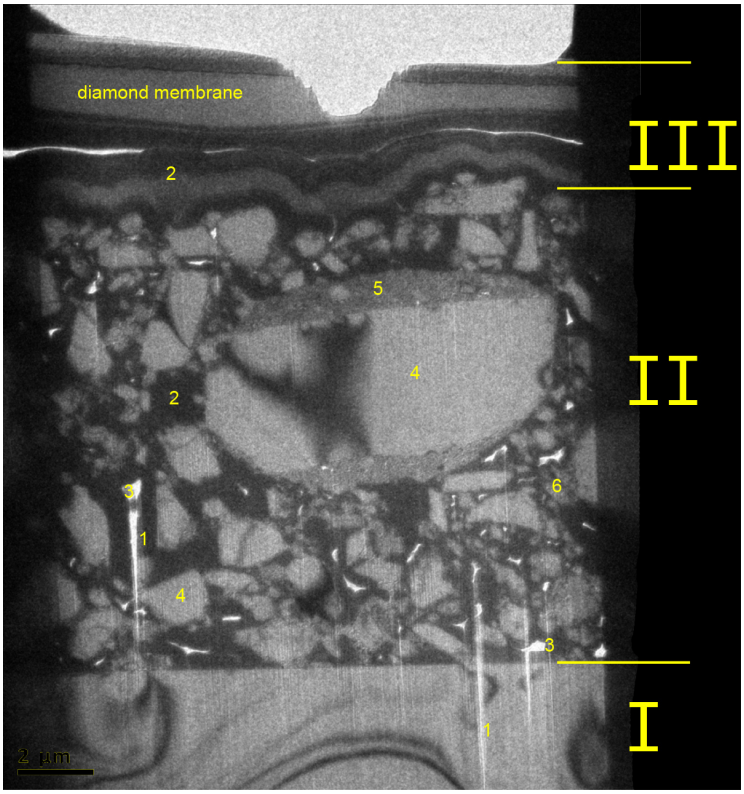

Figure 5.4: *Overview TEM-micrograph of the lamella produced of a printed layer, showing the distinct features of the sample. Region* **(I)** *shows the silicon wafer used as substrate,* **(II)** *shows the printed layer, and* **(III)** *shows the diamond membrane used to cover the printed layer*

the Pt filling is due to thickness variations of the Pt deposited. However damage to the sample could not be prevented in full, hence different artefacts arising from the FIB milling process are also visible. The light parallel lines visible in Fig. 5.4, marked with *(1)*, are milling artefacts of the ion beam. The darkest regions marked with *(2)* are residual platinum deposited to cover and fill the lamella (see chapter 3.2.2). Furthermore the white structures *(3)* in Fig. 5.4 are unfilled holes.
Within the printed layer several distinctive feature can be seen. The areas marked with *(4)* are large mono crystalline particles. Due to the short milling time of only 90 minutes and the general particle production process during milling a disperse size distribution is expected. Although very few in number compared to the smaller particles, the larger structures dominate the image. These also have a light contrast with dark contours due to bending, similarly to the wafer substrate (region (**I**)). A

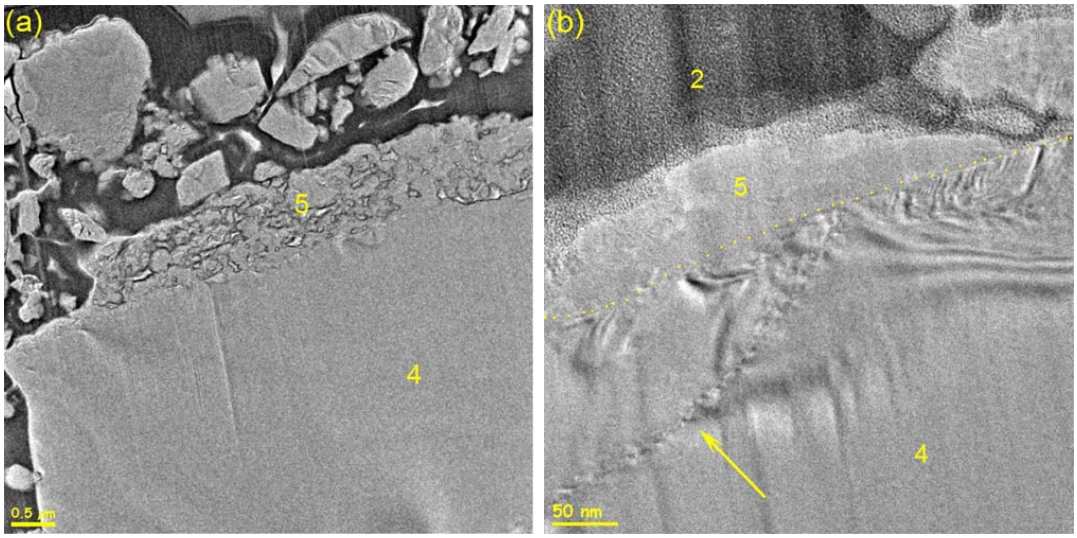

Figure 5.5: ***(a)*** *TEM micrograph showing the interface of large monocrystalline particles and nano-phase crystals.* ***(b)*** *Higher magnification image of a interface showing defect generation.*

grey layer, with internal structure, covering some of the mono crystalline particles is marked with *(5)*. A few particles have a spotty and streaky diffraction contrast *(6)* corresponding to a high concentration of defects, due to the preparation process of the particles.

A higher magnification micrograph, Fig. 5.5(a), of the same lamella shows the region surrounding a part of the larger particle *(4)* seen in Fig. 5.4. The edge of the particle on the left hand side seems to be straight with only one small particle attached to it. However, the top surface of the large crystalline particle is decorated by smaller particles *(5)*. The interface is not clearly visible, indicating a close contact of the crystals. The origin of the small crystalline nanoparticles at the surface is not conclusive, but might be an indication of the milling process where attrition is happening (see chapter 3.1.1) or may result from smaller particles being pushed into the surface of the large particle during milling. This situation is also visible around a few smaller particles. In Fig. 5.5(b) another low magnification TEM micrograph of the interface (dotted line) between a smaller particle *(4)* and the nano-phase crystals *(5)* is shown. It can be again seen that the particles do not show a significant separation between them. An extended defect can be seen in the large particle, marked with an arrow. Defects like these are produced during the milling process

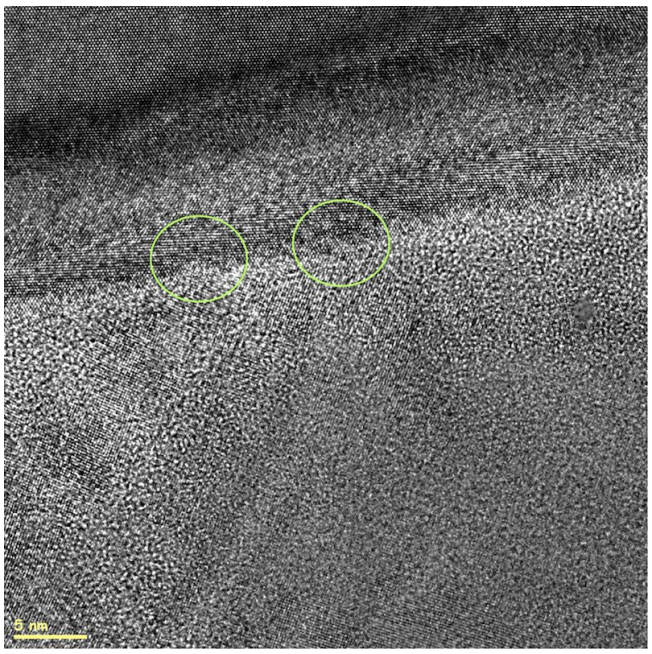

Figure 5.6: *Interaction of Si nano-crystalline phase with silicon crystals. There is a direct contact between the lattices of the particles without a clear separating interface.*

when the particles are cleaved into small pieces. The contours visible in the larger particle which indicate stress fields can be seen to cross this defect, suggesting that these originate from flexing of the lamella after the sample preparation.

A higher magnification micrograph of this interface is shown in Fig. 5.6. It clearly shows that the smaller nanoparticles are attached to the surface of larger particles. It can be seen in the micrograph that there is a direct contact between the lattices of the two crystals (green circles). This close contact, without the particles having a significant capping layer (see chapter 4.2) enables the observed charge transport throughout the percolation network described later in chapter 6.

That the silicon nano crystals are randomly oriented can be seen in Fig. 5.7 which shows a higher magnification of the area marked with *(5)* in Fig. 5.5(a). A qualitative image analysis of the micrograph shown in Fig. 5.7(a) of the orientation of the nano crystals is shown in Fig. 5.7(b), where the orientation of the lattice is colour coded. For this purpose the <111> lattice fringes were analysed and the different colours reflect the azimuthal orientation of the fringes. Green indicates horizontal (on the page) fringes, blue 45°, pink 90° and red 135° tilt.

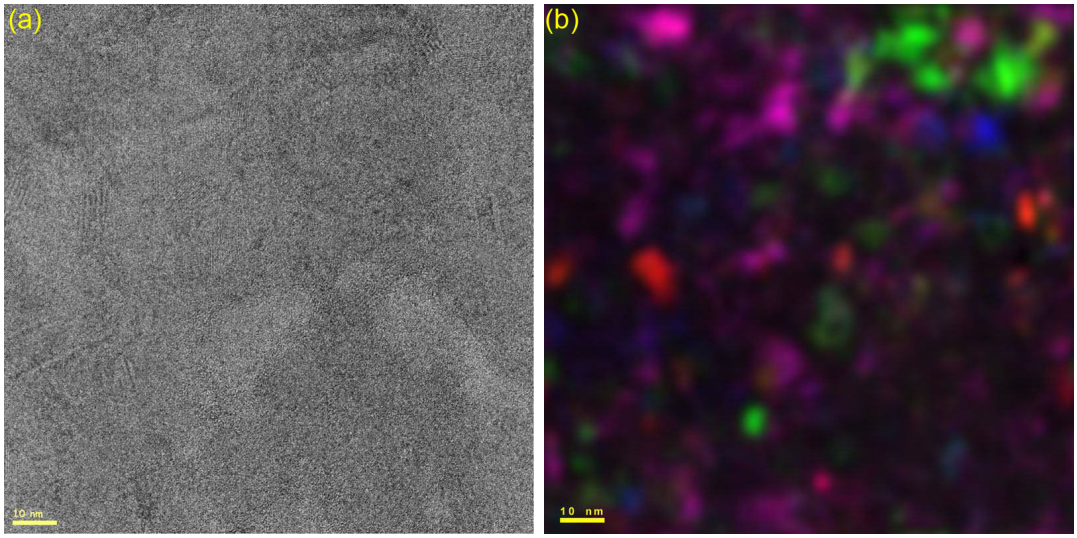

Figure 5.7: ***(a)*** *HRTEM micrograph of nano crystalline particles.* ***(b)*** *Qualitative image analysis of the crystal orientation. Intensity corresponds to appearance of the <111> lattice, orientation is colour coded, green indicates horizontal (on the page) fringes, blue* $45°$*, pink* $90°$ *and red* $135°$ *tilt*

As there is no visible contrast in lower magnification micrographs of this region it might have been concluded that this is a mono crystalline particle and therefore the constitution of the printed layer is falsely interpreted. In reality the close contact between particles formed and connected with these nano-phase crystals are poly-crystalline even though they appear to be homogenous in most scanning electron micrographs. These small nano-phase silicon crystals can be found at the surface of almost every larger silicon crystal, and might be a key to form connections between large clusters of particles with each other.

A more important feature, that might originate from the milling of the particles used to print the layer is shown in the TEM micrographs in Fig. 5.8. The structures (i) on the left in Fig. 5.8(a) are clusters of particles, whereas on the right a single large particle (ii) can be seen. The dark regions (iii) are Pt deposited to fill in the lamella. The high magnification micrograph in Fig. 5.8(c) shows that the smaller particles are polycrystalline, in contrast to the large particle which is a defective single crystal. Energy transfer in the milling process not only breaks the particles into smaller units, but during milling firstly dislocations and then grain boundaries are introduced into the crystal structure as seen in Fig. 5.5. Again there is no indication

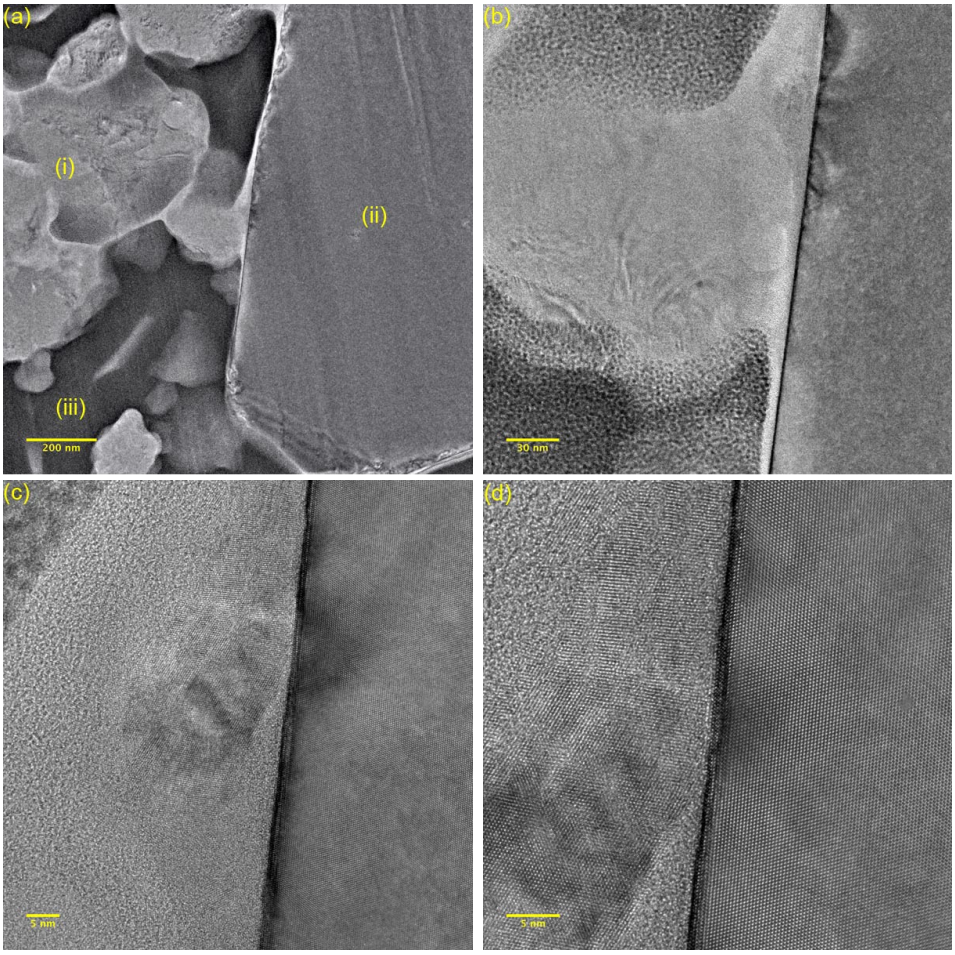

Figure 5.8: *TEM micrographs of a printed silicon layer in a cross-sectional view at four different magnifications.*

of amorphisation, and hence within the particles charge transport is expected to be equivalent to that in polycrystalline silicon. In Fig 5.8(c) it can also be clearly seen that the silicon lattice planes in both particles are in contact with each other. There is no silicon oxide layer hindering charge transport between the particles. The dark line visible in Fig. 5.8(b),(c) & (d) is an optical artifact which can be reproduced in simulations, occuring because the grain is very thick and slightly tilted.

In addition it can be seen in Fig. 5.9 that some of the nano-phase silicon crystals are encased by a thin amorphous layer, marked as *(7)*. This is a light amorphous polymer layer on the surface of the particles, remaining from the binder used to prepare the ink, as described in chapter 3.1.2. The thickness of this layer is up to

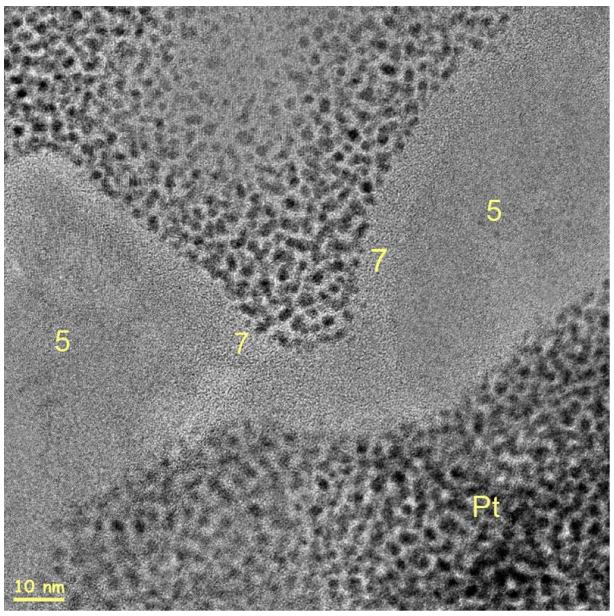

Figure 5.9: *HRTEM micrograph showing that the size of nano-crystalline silicon (marked with (5) is about $5nm$. Some crystals have a light amorphous capping layer (7).*

5nm but could only be found on few particles and some particles are not covered completely. As this thin layer is not present between all particles, it does not hinder the charge transport much, and its presence is in good agreement to the expected amount of about 9% binder left after the layer is cured (see chapter 3.1.2).
In summary combined SEM and HRTEM studies reveal that the silicon particles, according to their milling state, are either polycrystalline or single crystalline depending on their size. No amorphisation occurs due to energy transfer in the milling process. Furthermore, the particles are in close contact, which is the requirement for percolation driven charge transport [39]. Because the micrographs shown are of a printed layer which is produced using a water-based ink, it can be concluded that wet processing of the particles does not change the surface state of the particles. The nanoparticle surfaces are not only stable under ambient atmospheric conditions, but no surface oxidation is formed in aqueous environments. The mesoscale features described above are supported also by topological models derived from ultra-small angle X-ray scattering (USAXS) experiments [93,95]. Additionally it has been shown by SAXS that these small primary clusters are stable throughout the ink preparation and printing processes, and are generally independent of the ink chemistry [93] and

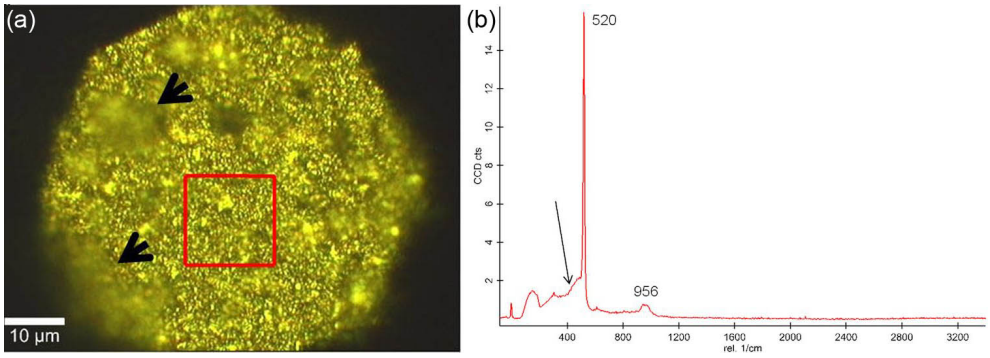

Figure 5.10: ***(a)*** *optical micrograph of the area scanned with the Raman microscope,* ***(b)*** *shows an average spectrum of all the acquired spectra during Raman imaging.*

flow processes during deposition, whereas larger structures are sensitive to these parameters [95].

5.3 Raman spectroscopy of printed silicon

For this study Raman spectroscopy was performed on printed silicon layers. The data were obtained from a top view spectrometer under ambient conditions with no special precautionary steps, as described in chapter 3.2.4. The parameter used for imaging are summarized in table 5.1.

Fig. 5.10(a) shows the optical micrograph of the imaged area, seen through a 100x air objective (NA = 0.9). Due to the rough composition of the silicon print it can be seen that large areas marked with arrows are not in focus. The red frame in Fig. 5.10(a) marks the area scanned in Raman imaging mode. Fig. 5.10(b) shows the average spectrum of all aquired spectra during Raman imaging. It shows characteristic Raman bands of silicon at $520 \pm 3\, rel.\, 1/cm$ (1st order Si) and $956 \pm 3\, rel.\, 1/cm$ (2nd order Si). In addition there is no $C-H$ stretching peak visible in the spectral range $2800 - 3000\, rel.\, 1/cm$, which may give hints for organic components in the printed ink. However, there is a non characteristic shoulder at the low wavenumber side of the Si peak marked with an arrow in the spectrum which cannot be explained conclusively. This feature could be attributed to either the ω_1 band of the Si-O-Si configurations [180], to a contribution from the shifted Si peak due to phonon

Table 5.1: *Image scan parameters used.*

Image scan:	
Points per Line:	150
Lines per image:	150
Scan width:	15
Scan hight:	15
Integration time [s]:	0.08

confinement in small particles [181], or to a contribution from a well known amorphous silicon band at $480\,rel.\,1/cm$ [182, 183].

Figure 5.11(a) shows the intensity distribution of the 1st order Si band over the surface area analyzed. The intensity variations shown in Fig. 5.11(a) of this band reflects again the high roughness of the sample. The red and blue lines in the image mark the positions where the cross sections (shown in Fig. 5.11(b)) were measured. Due to the frequency doubled NdYAG laser with $532\,nm$ wavelength, used for excitation, only particles with a size larger than the diffraction limit of $368\,nm$ could be detected (see double peaks in Fig. 5.11(b)). This gives a strong indication, that some particles have a diameter below this value.

By applying a Gauss fit to the recorded Raman spectra, the precise position of

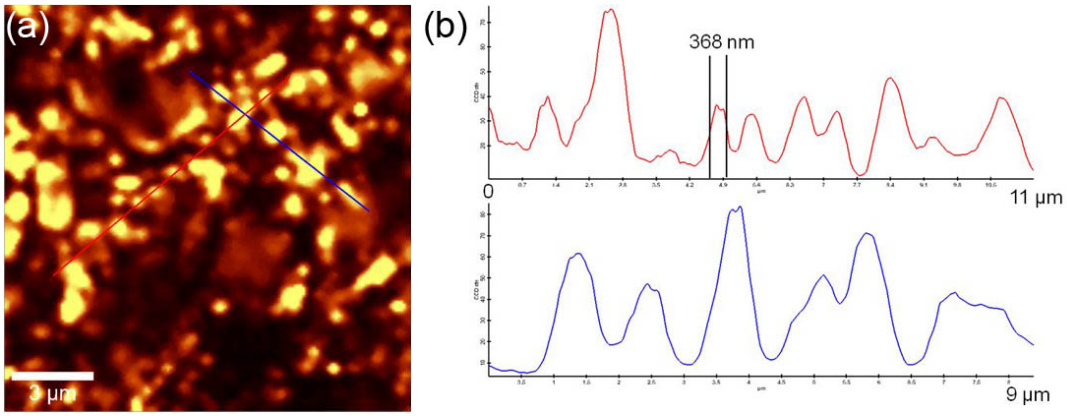

Figure 5.11: ***(a)*** *shows the intensity distribution of the 1st order Si band and the lines used for cross sections (red and blue line) of the imaged area.* ***(b)*** *Cross sections of the intensity distribution of the 1st order Si band.*

the 1st order Si Raman band and its width can be determined. The shift of this Raman band may be connected with deformation of the silicon lattice and possible particle size, whereas variations of the width of the Raman bands can be related to the crystallinity of the sample and the dispersion of the size distribution. The image shown in Fig. 5.12(a) shows the variation of the centroid and the image in Fig. 5.12(b) shows the width of the 1st order silicon band respectively. Due to the high surface roughness of the printed layers (see also chapter 5.1) the results presented above may not be representative for the whole sample. For the printed silicon layers, Raman spectroscopy reveals that the printed silicon nanoparticles are defective and have a different crystallinity, which is in good agreement to the HRTEM study discussed in chapter 4. The non characteristic shoulder of the 1st order Si band at $520\,rel.\,1/cm$ might be due to the islands of disordered surface regions described in chapter 4.2, particularly if these are oxygen related. However Raman microscopy is not suitable for a precise spatial analysis of the printed nanoparticulate network used, because most of the particles are smaller then the diffraction limit of the microscope used.

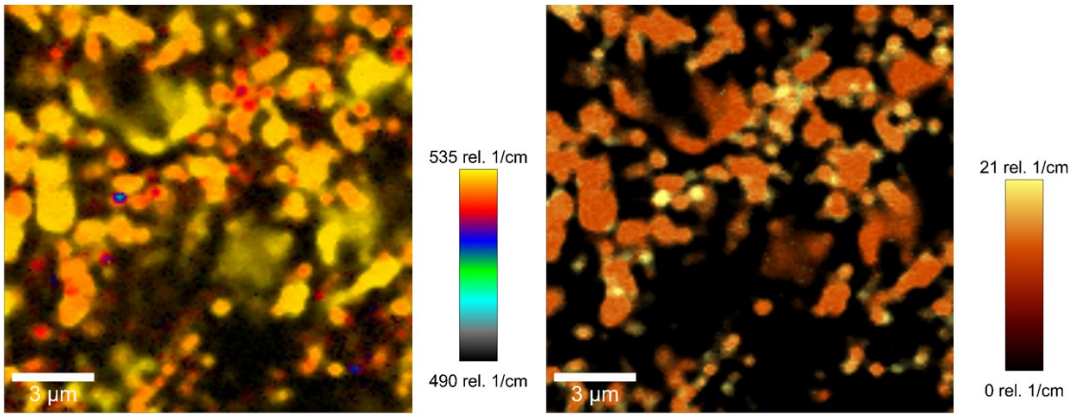

Figure 5.12: ***(a)*** *shows the center of mass of the 1st order Si band, and* ***(b)*** *shows the width of the 1st order Si band.*

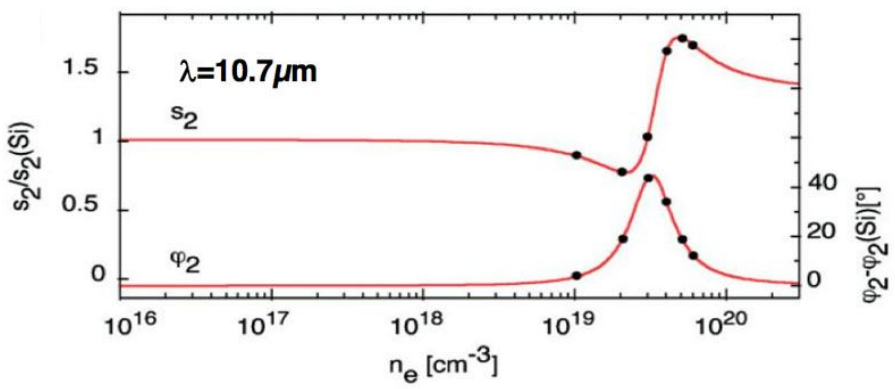

Figure 5.13: *Calculated near-field amplitude s_2 and phase φ_2 signal for varying free carrier concentration in n-doped Si at $\lambda = 10.73\,\mu m$ ($\omega = 932\,cm^{-1}$) and varying free carrier concentration [158, 184].*

5.4 Scattering type near-field optical microscopy of printed silicon layers

In order to circumvent the resolution related restriction of Raman spectroscopy, mid-infrared scattering type scanning-type near-field optical microscopy (IR s-SNOM) has been performed on printed silicon layers. This technique can overcome the diffraction limit, experienced with Raman spectroscopy discussed in 5.3 above. In particular, IR s-SNOM provides a high spatial resolution typically in the $10\,nm$ range [168].
For this study, layers printed from highly doped n-type silicon nanoparticles produced by high energy milling were investigated. Fig. 5.13 shows the calculated near-field amplitude and phase signal for varying free carrier concentration in doped silicon [184]. For this calculation the monopole model described in chapter 3.2.3 has been used. It can be seen that for a carrier concentration of $> 10^{19}\,cm^{-3}$ the near-field signals show characteristic changes, with local amplitude s minimum and maximum and as a local phase φ maximum occuring for free carrier concentrations in the range $10^{19} - 10^{20}\,cm^{-3}$. Therefore simultaneous amplitude and phase contrasts in near-field images are suitable for samples printed with highly doped silicon nanoparticles.

As a first experiment surface imaging of a printed layer using highly doped silicon nanoparticles was performed, but due to the high surface roughness $> 1\,\mu m$ (as previously shown in chapter 5.1) imaging using s-SNOM was not successful. As the

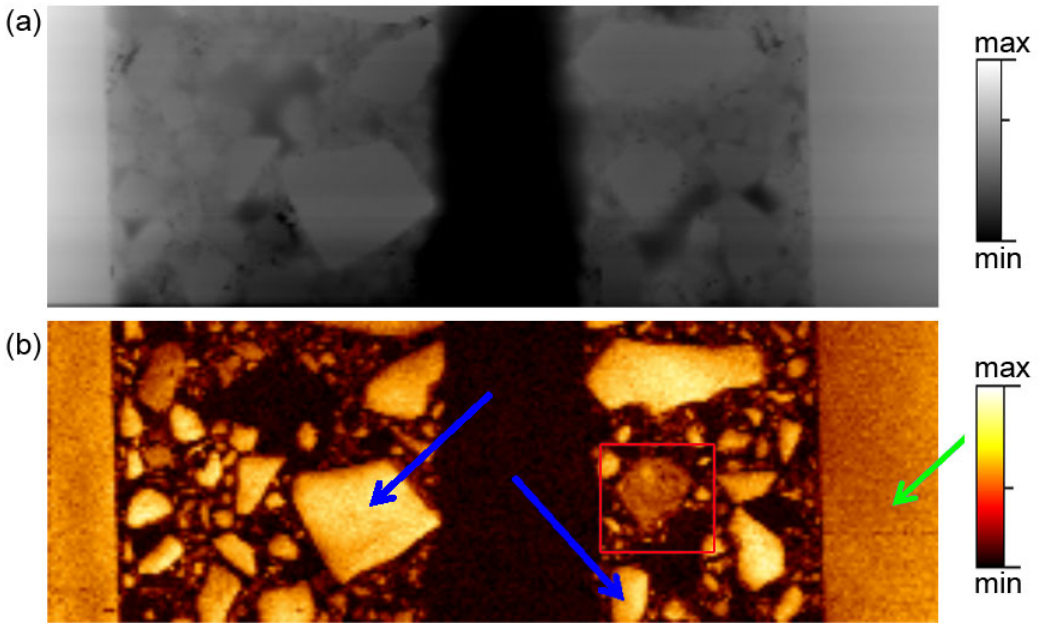

Figure 5.14: *Overview of the area imaged using IR s-snom,* ***(a)*** *is showing the topography, and* ***(b)*** *the amplitude signal micrograph.*

s-SNOM is based on an atomic force microscope (AFM) rough surfaces introduce atrefacts in the both amplitude and, especially, in the phase signal of the scattered radiation. In order to overcome these problems, the printed layers were stabilized by embedding them in EPO-FIX resin (see chapter 3.2.3). After curing for 24 hours the layers were mechanically polished to a suitable smoothness before being used for s-SNOM (see Fig. 3.10 in chapter 3.2.3). The wavelength used for these measurements was $9.26\,\mu m$ $(1080\,cm^{-1})$.

An overview of the area imaged is shown in Fig. 5.14. Fig. 5.14(a) shows the AFM image of the topography, revealing that the surface roughness is about $700\,nm$, including a clear depression in between the two printed layers. This depression is the resin used for embedding, which is softer than the silicon and hence the surface is lower after mechanical polishing. On the silicon however, the sample shows no significant surface roughness and is therefore suitable to be used with IR s-SNOM. Fig. 5.14(b) shows the third harmonic infrared amplitude images (s_3). The green arrow indicates the low doped silicon substrate used as reference, whereas the bright silicon grains with a much higher amplitude are indicated by the blue arrows. These

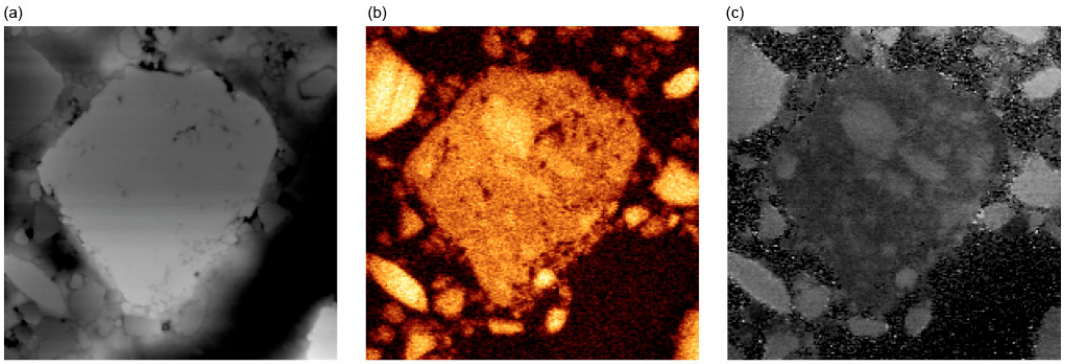

Figure 5.15: ***(a)*** *is showing the topography, and* ***(b)*** *the infrared amplitude (s_3) signal, and* ***(c)*** *the phase (φ_3) signal.*

bright grains also show a strong phase contrast. Next to the bright grains there are also grains with lower amplitude visible (red square). Topography and infrared amplitude (s_3) and phase (φ_3) images, of the third harmonic, of the area marked with the red square are shown in Fig. 5.15. The topography of the selected area is shown in Fig. 5.15(a), the infrared amplitude and the phase images are shown in Fig. 5.15(b) and Fig. 5.15(c) respectively. It can be seen that the topography only shows a slight gradient from top to bottom which results from a slight tilt of the polished surface. Additionally it can be seen that the particle does have an internal structure. This internal structure, areas of brighter and darker contrast with different sizes, can be clearly seen at the infrared amplitude (s_3) and phase (φ_3) images shown in Fig. 5.15(b) and Fig. 5.15(c). This can be explained by the fact that this object consists of small crystals showing a variation in amplitude and phase of the printed silicon, due to variations of the free carrier concentration of 10% to about 50%.
An additional feature can be seen with higher magnification imaging shown in Fig. 5.16. Fig. 5.16(b) shows an enlarged AFM topography micrograph, Fig. 5.16(c) and Fig. 5.16(d) a similar amplitude s_3 phase φ_3 image of the particle marked with the arrow in Fig. 5.16(a). Fig. 5.16(d) shows the near-field phase signal φ_3 with a scale from 0..180° together with a restricted scale from 0..18° shown in Fig. 5.16(e). The bright ring in the near-field phase signal φ_3 seen in Fig. 5.16(e) is an indication that the free carrier concentration at the outside of the particle is about 10% lower than inside. Furthermore it can be seen in all images that the small particles in the

s-SNOM images show almost no phase contrast, which may reflect a much smaller free carrier concentration.

The reduced mobility observed above is in good agreement with previous work for layers printed from metallurgical grade silicon [109]. This observation can be explained by shifts of the optical phonon frequencies caused by different doping levels or more likely local strain due to the production process, which reduces the carrier mobility. However this experiment only suggests a reduced carrier mobility at high-frequency (infrared) around 30 THz, whereas the DC mobility might be affected differently.

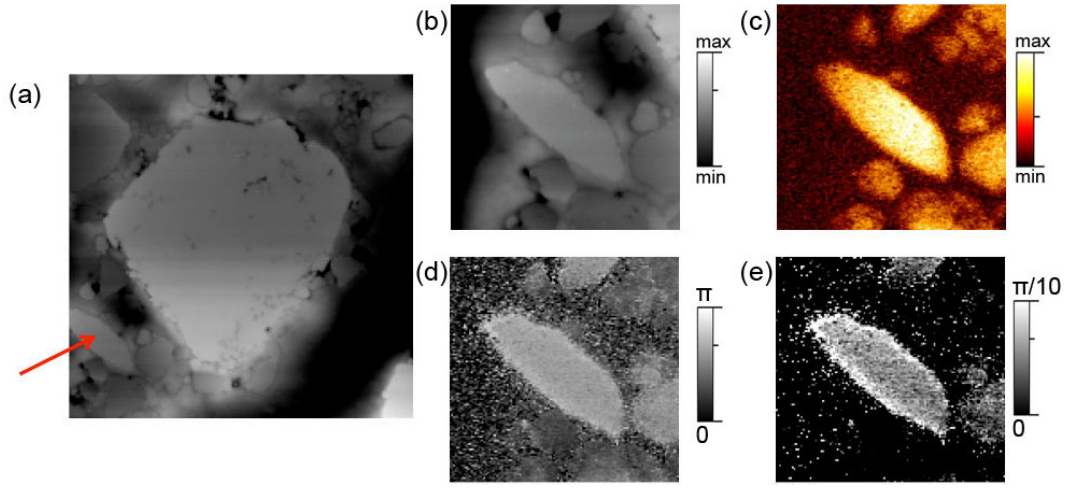

Figure 5.16: ***(a)*** *is showing the topography of the area shown above, and* ***(b)*** *the (AFM) topography together with the amplitude image, and* ***(c)*** *the phase shift image of the particle marked with the red arrow in (a).*

6 Device performance of printed silicon nanoparticulate diodes

In previous works silicon nanoparticles have been used to print symmetric devices in terms of the conductor used which, however, had non-linear I-V characteristics [108, 109]. For this work the device production has been extended in a way that different contact materials are used in order to get asymmetric current - voltage behaviour. To achieve this goal, heterostructure devices were produced and examined. In this chapter the I-V characteristics of the printed diodes and their analysis will be discussed. To print these diode structures, the silicon nanoparticles produced and characterized in previous sections were used. The electrical characteristics were measured using a Keithley 4200 SCS as described in chapter 3.4, and the data were exported to Origin 9.0 for further analysis. The devices can be seen as diodes with two metal-semiconductor junctions, with the nanoparticulate layer serving as the common semiconductor layer and the I-V characteristics of both junctions in the device are determined by the alignment of the Fermi levels in the two materials. Therefore they can be either ohmic or rectifying (see chapter 2.3). Hence diodes with

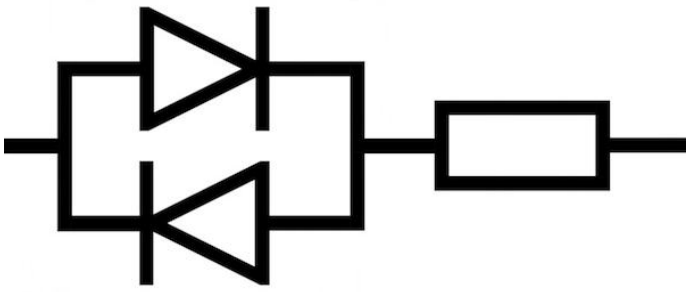

Figure 6.1: *Equivalent circuit used to model heterostructure of the devices printed for this thesis.*

different electrode materials are expected to show different behaviour depending on the position of the Fermi level (work function) in each.

6.1 Asymmetric junction diodes

For these kind of devices a back to back diode model (schematic shown in Fig. 6.1) can be used as the equivalent circuit. The mathematical description of this circuit is two diode functions (see chapter 3.8) subtracted from each other giving:

$$I = I_0 \exp\left(\frac{eV}{n_0 k_b T}\right) - I_1 \exp\left(\frac{-eV}{n_1 k_b T}\right) - (I_0 - I_1) \tag{6.1}$$

where I_0 and I_1 are the saturation currents in reverse bias and forwards bias respectively, n_0 and n_1 are the diode ideality factors.
As a first approach to produce rectifying devices, carbon nanotubes (CN), produced by Canatu Ltd. Finland, deposited at Canatu on a PET substrate, were used as a bottom contact. This was followed by a printed silicon layer, using 80% particle loading by relative weight to an acrylic binder of nanoparticles produced from p-type wafer ($\rho < 0.005\,\Omega cm$). To test the electrical characteristics of the Si-C junction different electrode combinations were constructed. In the first approach aluminium tape was used as the second contact. The GNDU of the SCS was connected to the carbon, making this contact the anode of the device. Hence the diode parameters I_1 and η_1 in Eq. 6.1 should refer to this junction. Figure 6.2(a) shows the DC I-V curve of a CN/p-si/Al-tape heterostructure, with an image of the device shown in the inset. The diode was measured using a voltage sweep in steps of $0.16\,V$ starting from $-16\,V$ up to $+16\,V$. It can be seen from the graph, that the I-V characteristics are non-ohmic and essentially non-rectifying. The device conducts in both directions at around $-8\,V$ and $+6\,V$ respectively. Two non-ohmic current versus voltage relations are observed on the graph resulting from the carbon nanotube / silicon and the silicon / aluminium junctions. 5 diodes of this type were produced and measured and they all show a similar behaviour. A fit based on Eq. 6.1, given by the solid line in Fig.6.2(a), determines the saturation currents to be $I_0 = 1.8 \cdot 10^{-4} \pm 4.5 \cdot 10^{-5}\,A$

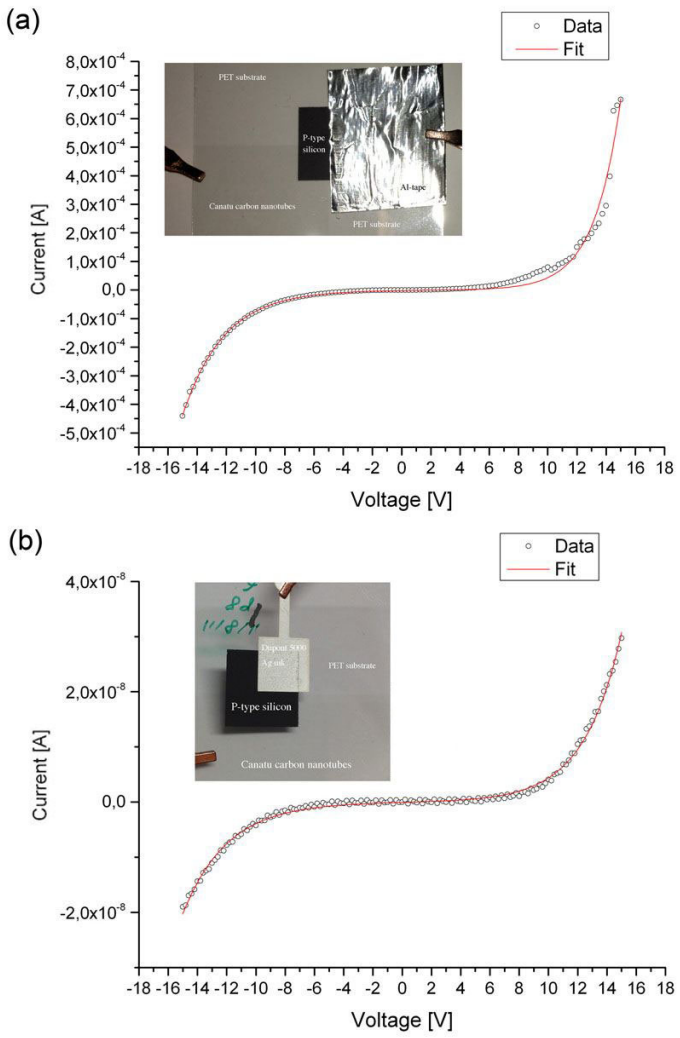

Figure 6.2: *Room-temperature I-V characteristics of* ***(a)****CN/p-si/al-tape and* ***(b)*** *CN/p-si/ dupont 5000 silver ink*

and $I_1 = 2.1 \cdot 10^{-3} \pm 4.2 \cdot 10^{-4}\, A$. Although the general behaviour of the I-V curve is reproduced, the high diode ideality factors of $\eta_0 = 71 \pm 2$ and $\eta_1 = 110 \pm 4$ respectively suggests that most of the applied voltage does not drop across the junctions, but rather in the nanoparticulate silicon layer. Furthermore the electrical contact of aluminium tape as a conductor is poor and possibly unstable due to the presence of glue at the interface.

To improve the contact to the cathode a commercially available silver conductor ink (Dupont 5000) was used to print the top contact material in a second approach.

Otherwise the set-up and measurement conditions were the same. Of the 10 diodes printed, eight of these devices show similar results, but two of them have symmetric I-V curves with a low resistance. This was caused by direct contact of the printed silver ink with the carbon nanotubes due to bad registration of those prints.
The DC I-V characteristics, under ambient laboratory conditions, of a representative CN/p-si/Ag heterostructure are shown in Fig. 6.2(b) with a photograph of a typical device in the inset. The saturation currents for this device were found to be $I_0 = 8.9^{-8} \pm 6.1^{-9}\, A$ and $I_1 = 1.48^{-7} \pm 1.2^{-8}\, A$ respectively. Due to design related differences (e.g the distance between the two conductor layers is different because the devices were registered by hand during printing) the absolute values of the saturation currents cannot be compared directly. However, the ideality factors were about the same and found to be 100 ± 1 and 118 ± 2 for η_0 and η_1 respectively, compared to $\eta_0 = 71 \pm 2$ and $\eta_1 = 110 \pm 4$ for the previous device with the aluminium tape contact.

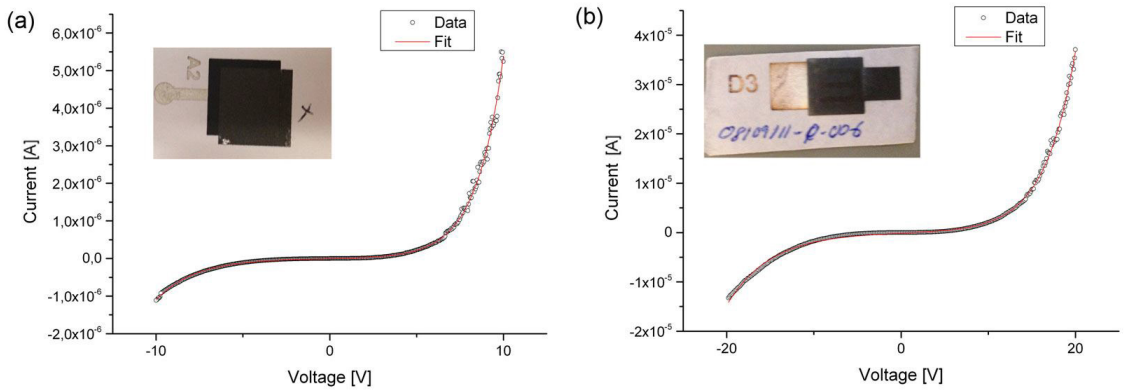

Figure 6.3: ***(a)*** *Opposed diode produced with commercial available Dupont 5000 silver ink, P-si-NP and carbon-NP ink, and* ***(b)*** *lateral design using the same materials.*

In Fig. 6.3 similar diodes printed with commercial silver ink (Dupont 5000 or Pchem PSI-211) as bottom contact but with a counter electrode printed using an ink mixed with carbon nanoparticles are shown. The silicon ink, used for the active layers, was produced with both p-type and n-type nanoparticles produced from wafers with $\rho < 0.005\,\Omega cm$, and $\rho = 0.008 - 0.02\,\Omega cm$ respectively. The carbon ink was produced with milled nanoparticles as described in chapter 3.1. Both silicon inks as well as the carbon ink were produced with 80% particle loading by relative weight. Using

these inks two different designs (see chapter 3.1.3) were printed on paper. It was not possible to produce a screen printable ink using graphene platelets.
The diodes were measured with the Keithley 4200 SCS using a voltage sweep in steps of $0.1\,V$ starting from $-10\,V$ up to $+10\,V$ for the opposed and in steps of $0.2\,V$ starting from $-20\,V$ to $+20\,V$ for the lateral design. As with the previous devices, the carbon contact was connected to the GNDU, making this the anode. In order to obtain the diode parameters, Eq. 6.1 was used as before.
For the opposed design 60 diodes were printed using p-type and n-type silicon respectively. The yield for this design was with about 40% relatively low, whereas for the lateral design 90 diodes were printed for each doping level with a yield of about 75%. The higher yield of the lateral design is to be accounted for by the fact that the two conductive tracks are not overlapping and therefore internal short circuits have not been measured as often. However, the higher ideality factor and saturation currents of the lateral design are due to the larger distance between the two conductors as the charge has a longer percolation path to follow.
For the p-type diodes printed with the opposed design (Fig. 6.3(a)) the ideality factors, η_0 and η_1, were found to be 60 ± 0.4 and 88 ± 2 respectively, whereas for the lateral design (Fig. 6.3(b)) these were almost double at 137 ± 0.7 and 193 ± 2.2 respectively. The respective saturation currents were found to be $I_0 = 8.7 \cdot 10^{-6} \pm 3.0 \cdot 10^{-7}\,A$ and $I_1 = 1.3 \cdot 10^{-5} \pm 1.2 \cdot 10^{-6}\,A$ for the opposed and $I_0 = 1.2 \cdot 10^{-4} \pm 3.3 \cdot 10^{-6}\,A$ and $I_1 = 2.6 \cdot 10^{-4} \pm 1.0 \cdot 10^{-5}\,A$ for the lateral design.
In order to investigate the high diode ideality factor, compared to the previous diodes, a cross section of the diode has been prepared using a Zeiss Auriga FIB. Fig. 6.4(a) shows a photograph of the device used for cross sectioning, Fig. 6.4(b) shows scanning electron micrographs of a p-type diode with lateral design. The silver contact, beneath the silicon layer, is not visible in this figure. Fig. 6.4(c) shows the cross-sectional image that clearly reveals that the carbon does not have good contact with the silicon layer, which accounts for the device having a high overall resistance. Additionally the poor contact between the silicon and carbon might also contribute to the higher diode ideality factor. For the material combination presented above, the DC $I - V$ curve is non-ohmic and asymmetric under forward- and reverse bias.

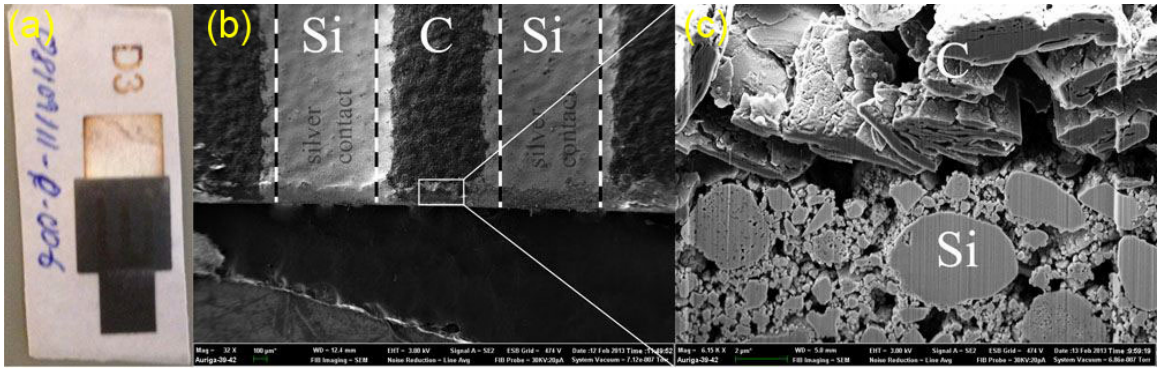

Figure 6.4: *Scanning electron micrograph of a fully printed diode on paper.*

The difference of the vacuum work function of the silver ($0.47\,eV$) relative to the vacuum electron affinity of the p-type semiconductor ($0.87\,eV$) is similar, hence the two are comparable and it can be assumed that the charge conduction is limited by the carrier injection into Ag and C for the forward- and reverse bias respectively.
As both semiconductors, p-type and n-type silicon form Schottky barriers with the contact, diodes using n-type silicon nanoparticles have also been produced the same way. These show the same overall behaviour, but the p-type diodes show a lower forward voltage. As the reverse leakage current is expected to increase with lowering the forward voltage, diodes made of n-type silicon have been used in further investigations.
For comparison diodes, using different doping levels of n-type silicon and a different material for the counter electrode have been printed. The opposed design, as described in chapter 3.1.3 was used because they exhibit a lower diode ideality factor. For the bottom electrode two different commercial silver inks were used: Dupont 5000 containing silver flakes, and PChem PSI-211 containing silver nanoparticles. For the active layer a water based, acrylic ink was used. The material used for the counter electrode was a commercially available Dupont LuxPrint 7164 translucent conductor (TCO). Diodes using the same doping level as for the diodes described above were also printed with much lower doping level of the silicon. Fig. 6.5 shows a representative I-V characteristics, measured from $-10\,V$ to $+10\,V$ of diodes printed with nanoparticles produced from the lower doped n-type silicon with a nominal resistivity of $\rho = 1 - 10\,\Omega cm$ (Fig. 6.5(a)) and from higher doped n-type silicon (Fig.

6.5(b)). It can be seen that both diodes show a more symmetric behaviour than the previously measured devices. Based on the fit of the data in Fig. 6.5(a), using Eq. 6.1, the diode parameters for the device with low doped silicon were found to be

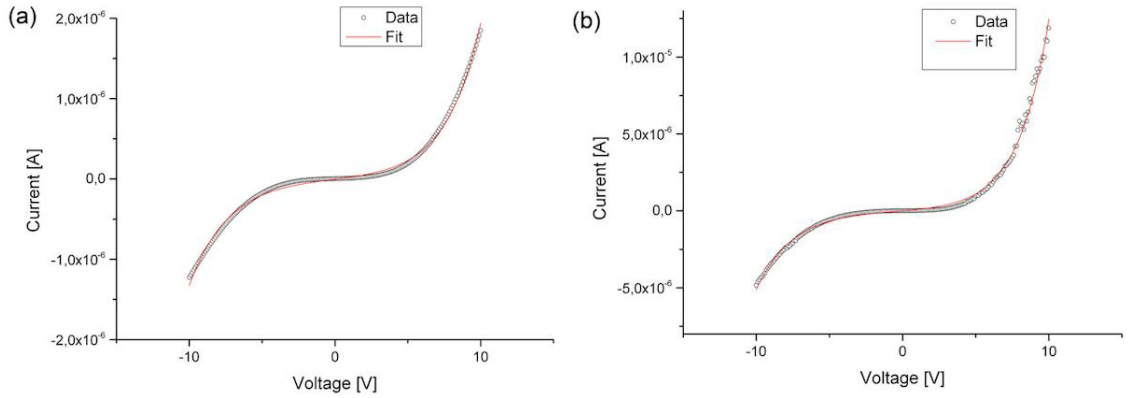

Figure 6.5: *Room temperature I-V curve using TCO as counter electrode and* ***(a)*** *low doped n-type silicon NP ($\rho = 1 - 10\,\Omega cm$), and* ***(b)*** *higher doped n-type silicon NP ($\rho = 0.008 - 0.02\,\Omega cm$)*

$I_0 = 2.9 \cdot 10^{-8} \pm 1.2 \cdot 10^{-9}\,A$ and $I_1 = 3.2 \cdot 10^{-8} \pm 1.6 \cdot 10^{-9}\,A$, and the diode ideality factors $\eta_0 = 92.4 \pm 1.0$ and $\eta_1 = 104.8 \pm 1.6$. These values confirm that the diode has an approximately symmetric character compared to the previously described devices. Fig. 6.5(b) shows the measured I-V characteristic of a diode printed with a higher doping level of the nanoparticles used (n-type, $\rho = 0.008 - 0.02\,\Omega cm$). It can be seen that this diode shows a slightly more asymmetric I-V curve in the measured range from $-10\,V$ to $+10\,V$. By fitting the data using Origin, the diode parameters were found to be $I_0 = 1.0 \cdot 10^{-7} \pm 6.0 \cdot 10^{-9}\,A$ and $I_1 = 8.9 \cdot 10^{-8} \pm 1.5 \cdot 10^{-8}\,A$ and $\eta_0 = 81.0 \pm 1.1$ and $\eta_1 = 96.4 \pm 3.4$ for the diode ideality factors.

The same overall behaviour was reproduced for diodes printed using silicon with the lower doping level, but with commercially available carbon ink (Dupont 7102) as a top contact. No difference was observed in the diode behaviour between the diodes printed with Dupont 5000 silver flake ink and PChem PSI-211 silver nanoparticle ink as a bottom contact.

For the total of 420 diodes printed using Dupont 7165 translucent conductor and Dupont 7102 carbon as top conductor for the opposed design the yield could be increased to about 70% for diodes with an active area of $0.5 \times 0.5\,cm^2$. Printing

diodes with an active area of $2.0 \times 2.0\,cm^2$ only resulted in a yield of about 10% due to the inhomogeneity and the high number of pinholes of the printed layer as shown in chapter 5.1. Most of the large area devices had low resistance indicating direct contact between the bottom and the top contact.
To obtain the behaviour of the diodes shown above, it is beneficial that a semiconducting material (in this case nanoparticulate silicon ink) with a high resistance prevents charge equalization. The asymmetric charge conduction arises between the work functions of the two (different) conductors with different barrier heights to the silicon. For the function of these devices the detailed structure of the metal/semiconductor junction is therefore not important, but it is, however, crucial that the metals are kept apart to avoid charge equilibration. If the conductors were connected by a third conductor the contacts would be ohmic. On the other hand, an insulator, as spacing between the two conductors would not allow charge transport at all. Therefore the two conductors need to be separated by something between a metal and an insulator which does not allow charge flow without an applied electric field. This is achieved by producing novel silicon nanoparticles, which maintain their semiconducting characteristics due to their unique surface characteristics. These particles are required, because they form a depletion layer to both conductors, allowing charge injection into the semiconductor with different barrier heights. If only one of the two contacts forms a depletion layer a Schottky diode will be formed. The high ideality factor observed for the diodes printed with carbon NP ink as top contact is to be accounted for because the current is limited by the carrier transport thought the nanoparticulate silicon film. For an ideality factor as high as 200, it can be suggested that most of the applied voltage drops across the nanoparticulate silicon layer rather than at the barriers. It can be seen that the ideality factor of the diodes can be reduced by half using different inks and higher doping level. For higher doping levels the ideality factor, and hence the rectifying properties of the diodes, can be increased. However, with using silicon nanoparticles with a nominal resistivity of $\rho = 0.008 - 0.02\,\Omega cm$, which equals a doping level of around $6 \cdot 10^{18}\,cm^{-3}$, rectifying contacts cannot be achieved.

6.1.1 Diodes printed using a solvent based system

Planar diodes were also fabricated using solvent based ink systems for comparison with the previously reported water based, acrylic devices. For the conductive layers (using silver nanoparticles with 70% particle loading and graphene platelets with 80% particle loading, see chapter 3.1.2) as well as the semiconducting layer (highly doped silicon NP ($\rho < 0.001\,\Omega cm$)) inks were mixed using ethyl cellulose as the binder and butyl cellosolve as the solvent respectively as described in chapter 3.1.2. It was not possible to produce screen printable inks using multiwalled carbon nanotubes. Figure 6.6 shows the I-V characteristics of a representative of the devices produced. It can be seen that the device shows a non-linear but not fully rectifying behaviour. Therefore it is reasonable to assume that an ohmic contact to the graphene could not be achieved, even though a doping level of around $7 \cdot 10^{19}\,cm^{-3}$ was used for the silicon layer. Using ethyl cellulose as binder it was not possible to produce diodes using other materials for the conducting layers. The obtained diodes showed a linear I-V characteristic with a very low resistance indicating that the silicon was short circuited. This result is due to the high number of pinholes in the ethyl cellulose inks as described in chapter 5.1.

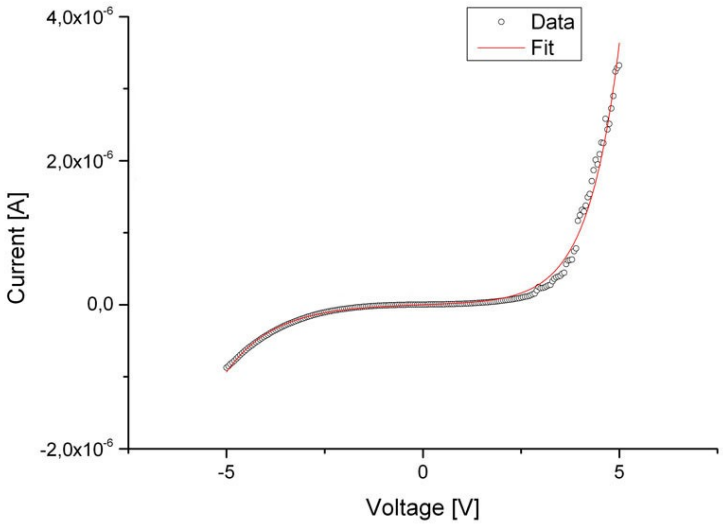

Figure 6.6: *Roomtemperature I-V curve of a solvent based device using silver nanoparticle ink as bottom contact, and graphene platelet ink as top contact.*

6.2 Fully printed Schottky diodes

In order to produce rectifying devices it is crucial to obtain one ohmic contact with the other contact being non-ohmic. As described in chapter 2.3 there are two possibilities in order to achieve an ohmic contact. One is to use a metal with the work function being lower than the vacuum electron affinity of the semiconductor used. However, because of the presence of interfering surface states this is not always possible [112, 114]. Another possibility to achieve an ohmic contact is to use a highly doped semiconductor (see chapter 2.3.2.3). Since the thickness of the depletion region b is inverse proportional to the carrier density $b \propto 1/n$ a higher doping level reduces the width of the depletion layer (see chapter 2.3). Eventually the depletion layer is thin enough so that electrons are able to tunnel through the barrier and hence do not have an obstacle against injection into the semiconductor. With this background, highly doped silicon nanoparticles (n-type, $\rho = 0.001 - 0.00102\,\Omega cm$) have been used to produce diodes with a single Schottky barrier. 240 Schottky diodes were fabricated using the same n-type Si nanoparticles but with either commercially available carbon and TCO as top contacts. Fig. 6.7(a) shows representative DC I-V curves of fully printed diodes using both inks as the top contact (opposed design with an active area $A = 0.25\,cm^2$, as described in chapter 3.1.3). The devices were printed, using Dupont 5000 silver or PChem PSI-211 silver nanoparticle inks for the bottom contact, and either Dupont 7102 carbon or Dupont 7165 TCO inks for the top contact.

The I-V characteristics of these devices can be represented as a series combination of a diode and a resistor (see chapter 2.3.2.2):

$$I = I_0 \exp\left(\frac{e(V - IR_s)}{\eta_0 k_b T} - 1\right) \tag{6.2}$$

where I_0, and η_0 are the same as above and R_s is a series resistance of the device which is usually assumed to be independent of the voltage applied. A fit to the measured data of both diodes, based on Eq. 6.2, is given by the red lines in Fig. 6.7(a). As seen in Fig. 6.7(a) the overall diode behaviour is reproduced for both diode systems, and the ideality factors are drastically reduced in comparison with

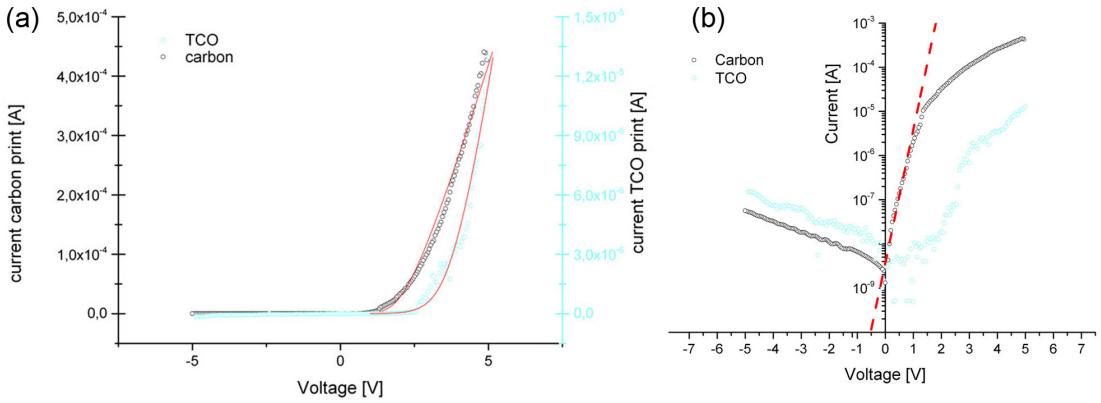

Figure 6.7: ***(a)*** *Comparison of I-V Characteristics of fully printed Schottky diodes using Ag/Si/C (black) and Ag/Si/TCO (cyan) structures.* ***(b)*** lnI *vs.* V *plot of both diodes and linear fit to the low voltage forward bias of the diode with carbon as top contact (dashed red line).*

the devices discussed in chapter 6.1. The diode ideality factors were found to be 10.7 ± 4.2 for the carbon based diode and 15.6 ± 4.7 for the TCO based one. However, the diode ideality factors are still high enough to suggest that most of the applied potential does not drop at the barrier, but rather across the nanoparticulate silicon layer. From equation 6.2 the saturation current density is found to be $1.1 \cdot 10^{-7} \pm 2.4 \cdot 10^{-8} \frac{A}{cm^2}$ and the series resistance is found to be $5.8 \pm 2.2\,k\Omega$ for the carbon based diode. For the diode with the TCO anode the saturation current was found to be $1.3 \cdot 10^{-9} \pm 4.8 \cdot 10^{-10} \frac{A}{cm^2}$ and the series resistance is found to be $77.6 \pm 7.5\,k\Omega$. Using the measured I-V characteristics, the rectifying ratio, using $-5\,V$ and $+5\,V$ of the devices were calculated. For the Ag/Si/TCO device the rectifying ratio (I_F/I_R) is only approximately 86, but for the Ag/Si/C device it was found to be about 7850. This behaviour can also be seen in Fig. 6.7(b) where a $\ln I$ vs. V plot is shown. Using Eq. 2.26 and Eq. 2.29 (see chapter 2.3.2) the ideality factor η_{carbon} of the printed Schottky diode and the barrier height Φ_b of the can be calculated from the forward I-V characteristics. The dashed red line in Fig. 6.7(b) represents a fit of the logarithmic forward I-V characteristic of the Ag/Si/C diode at low voltages. The barrier height of the diode with Ag/n-Si/C structure was calculated to be $0.82 \pm 0.1\,eV$ and the ideality factor 7.5 ± 1.8. This ideality factor is within the uncertainty in agreement with the diode ideality factor found directly using Eq. 6.2. Furthermore the calculated barrier height is in good agreement with previously

	Φ_b
This work Ag/n-Si	$0.82 \pm 0.10\,eV$
Schmitsdorf et.al. Ag/Si [185]	$0.73 \pm 0.11\,eV$
Guinea et.al. Ag/Si [186]	$0.66 \pm 0.04\,eV$
Aydin et.al. MIS system [125]	$0.79 \pm 0.02\,eV$

Table 6.1: *Calculated barrier heights in comparison with the barrier height calculated for the system produced for this thesis.*

reported values for the silicon-silver junction of $0.73\,eV$ [185] and $0.66\,eV$ [186], and 0.79 eV for a MIS system [125] (see Tab. 6.1).

Except for this work, in the literature no data has been presented on the performance of diodes based on printed silicon. However, a general comparison with diodes produced from vacuum deposited silicon and other nanomaterials and printable materials is useful to place the current results in context. An overall comparison of the diode parameters for relevant examples, extracted from the literature is given in Tab. 6.2. It can be seen, that the properties of the rectifying contacts produced in this thesis are comparable with the other systems considered.

As a comparison with the materials system of the diodes presented in this thesis, Altındal et.al. produced Au/n-Si Schottky diodes with a thin insulator layer (18Å) where the metal–semiconductor (Au/n-Si) Schottky diodes were fabricated on n-type (P-doped) single crystals silicon wafers. The experimental diode characteristics were found to be $3.61 \cdot 10^{-7} \frac{A}{cm^2}$ with an ideality factor of 2.878 and a rectification ratio of 342 [124].

Similarly Cd/p-Si Schottky barrier diodes (SBDs) with and without a native oxide layer have been studied by Aydin et.al. The devices were produced using a polished p-type silicon wafer with Schottky contacts formed by evaporation of Cd dots with a diameter of about 1.0 mm and an aluminium ohmic contact [125]. Here the authors reported a saturation current density of $2.06 \cdot 10^{-7} \frac{A}{cm^2}$ with an ideality factor of 1.32 and a series resistance of 310Ω.

As an example of using nanostructured materials, K. Mohanata and A. J. Pal [126] showed the ac response of rectifying junctions in ZnO nanowires grown from ZnO crystalline seeds, formed by thermal decomposition of zinc acetate. Single

Author	system	I_0 $[\frac{A}{cm^2}]$	η	R_s $[k\Omega]$	I_F/I_R	Ref.
This work	Ag/n-Si with carbon	$1.1 \cdot 10^{-7}$	10.7	5.6	7850	
This work	Ag/n-Si with TCO	$1.3 \cdot 10^{-9}$	15.6	77.6	86	
Altındal et.al.	Au/n-Si	$3.6 \cdot 10^{-7}$	2.9	assumed to be 0	342	[124]
Aydin et.al.	Cd/p-Si	$2.1 \cdot 10^{-8}$	1.32	0.3	100000	[125]
Mohanata & Pal	ZnO nanowires	-	5.8	15900	8.2	[126]
D. M. Taylor & H. L. Gomes	Al/poly(3-methylthiophene)	$13.3 \cdot 10^{-12}$	4.48	-	2200	[127]
Z. Ahmad & M. H. Sayyad	Al/methyl red	$3.2 \cdot 10^{-4}$	8.9	41.8	1.4	[128]
F. Wahab et.al.	CoPC/p-Si	$2.9 \cdot 10^{-9}$	6.14	20.0	316	[129]

Table 6.2: *Comparison of diodes produced in this thesis with diode systems in literature.*

$n^+ - n$ junctions within the individual wires were produced by successive growth of intrinsically doped n-type ZnO and extrinsically doped n^+-type material for the same period of time. The best rectification ratio was reported to be 8.2 for a growth time of 90 minutes for the n-type and n^+-type nanowires respectively with an ideality factor of 5.8 and a series resistance of 15.9 $M\Omega$.

At present Organic/inorganic heterojunctions are of widespread interest due to their use in various electronic and photonic devices. A Schottky barrier formed between aluminium and a conducting polymer precursor poly(3-methylthiophene) was shown by D. M. Taylor and H. L. Gomes in 1995 [127]. More recently, for example Z. Ahmad, and M. H. Sayyad presented the non-polymeric organic compound methyl-red in the fabrication of the surface-type Schottky diodes with Al and Ag contacts [128]. The Al/methyl red/Ag devices showed a saturation current density of $3.2 \cdot 10^{-4} \frac{A}{cm^2}$, a diode ideality factor of about 9, and a series of about $42k\Omega$. However, the devices had a very low on/off ratio of about 1.4 [128]. F. Wahab recently presented the fabrication of an organic/inorganic heterojunction of cobalt phthalocyanine (CoPc) with p-type silicon (p-Si) using vacuum thermal evaporation [129], which had a saturation current of $2.96nA/cm^2$. The diode ideality factor was found to be 6.14 with a series resistance of $20k\Omega$ and a rectification ratio of 316.

As performed in section 6.1, a cross section of a diode printed using a planar opposed design is shown in Fig. 6.8. Fig. 6.8(a) shows the device used for cross sectioning. The cross section was prepared in order to investigate the lower diode ideality factor found. It was produced by embedding the layer in resin and mechanically polishing as described in chapter 3.1.3. Fig. 6.8(b) shows the cross sectional SEM image of the

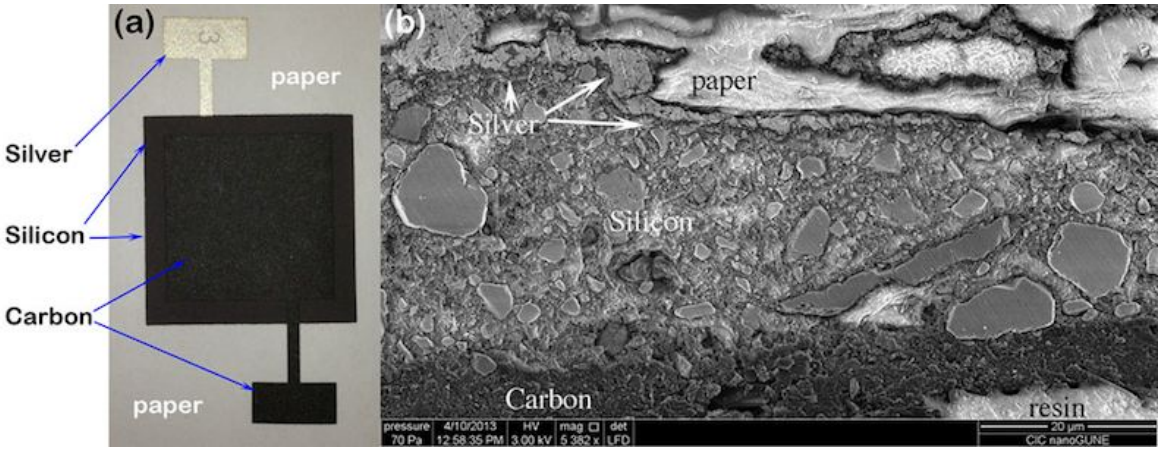

Figure 6.8: ***(a)*** *Image of a device using opposed design* ***(b)*** *Cross sectional scanning electron micrograph showing the internal structure of the device.*

device printed on paper. It can be clearly seen, that the three layers of silver, silicon and carbon form a compact, closely connected structure. Compared to the device produced with milled carbon nanoparticles (see Fig. 6.4), the different contacts show a very good contact to the silicon and hence allow charge transport with a lower contact barrier. Although the general diode behaviour is reproduced for the I-V curve, the high ideality factor 11 can be due to several different origins. Similarly to the asymmetric junction diodes, which have even higher ideality factors of up to 200, for the Schottky diodes the applied voltage under forward bias is higher than it could be expected for any reasonable single barrier. As discussed previously, due to the long percolation path for the charge in the silicon layer, a significant fraction of the applied voltage does not drop at the barrier, but rather across the nanoparticulate silicon layer. Other factors that could increase the ideality factor are that interface states at a thin oxide between the metal and semiconductor are formed and hence the current vs. voltage characteristics become nonlinear [187]. Furthermore tunneling currents become more important for highly doped silicon and influence the diode ideality factor [188]. However, these effects all assume spatially homogenous interfaces between the materials used. For the screen printed ink, made of nanoparticulate silicon with a disperse size distribution on a rough substrate, however, this assumption is not valid. As discussed in chapter 2 a further

contribution to the high ideality factor is possibly the influence of two-dimensional band inhomogeneities resulting in different Schottky barriers for currents [123].

6.2.1 Internal structure of fully printed Schottky diodes

For the observed I-V characteristic, the most important feature is, that the silicon nanoparticulate system forms a percolation path throughout the layer which allows charge to be transported. Although Fig. 6.8 shows that the particles form clusters of various sizes, it is not clear from this picture whether the silicon forms a continuous percolation path throughout the printed layer. In order to investigate this a method with elemental sensitivity is required. Fig. 6.9(a) shows a HAADF STEM image, superimposed with an EDX image of the oxygen $K\alpha_1$ emission (orange). In Fig.

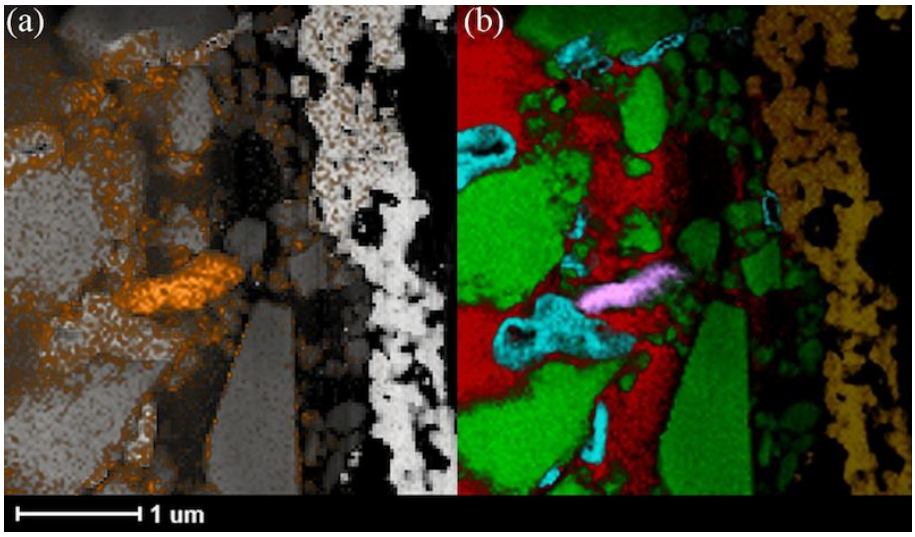

Figure 6.9: ***(a)*** *HAADF STEM image superimposed with an EDX image of the oxygen $K\alpha_1$ emission and* ***(b)*** *EDX elemental map revealing the internal structure of the silicon/silver interface of a printed Schottky diode. The colours represent the different materials detected as follows: silicon - green, silver - brown, carbon - red, platinum - turquoise, and iron - pink.*

6.9(b) EDX images of different materials can be seen overlayed. Due to the fact, that the specimen has been embedded for sample preparation, cavities in the porous printed layer are filled with resin used for embedding. This is seen as detected carbon which is coloured red in Fig. 6.9(b). Also from the sample preparation,

remains of platinum (turquoise) and and iron (pink) can be seen. Platinum was used to stabilize the layer during the FIB-milling process, and iron might be due to contamination introduced during mixing or milling the powder. The yellow layer at the right of Fig. 6.9(b) indicates the silver nanoparticles, used for the bottom contact. Silicon is represented as green. From the EDX image, it can be clearly seen again, that the silicon forms clusters of various sizes. Oxygen is mainly found with the iron contamination, but also with the carbon and platinum. There is however, only a small amount of oxygen found inside or at the surface of the silicon clusters. Occasionally oxygen is found attached to small islands on the silicon surface and sometimes as a very thin layer on small particles. This is in very good agreement with the results of the particle characterization, shown in chapter 4. However, this elemental map does show that, in this two dimensional representation of the printed layer there is no obvious percolation path.

In order to investigate the internal structure of a printed layer in full, it is therefore necessary to reconstruct the three dimensional internal structure of a printed layer. For this purpose, the first 3-D tomographic reconstruction of a printed silicon nanoparticulate layer has been carried out for this work. A diode, printed on paper was subsequently cross-sectioned with a FEI Helious NanoLab^{TM}DualBeam^{TM}

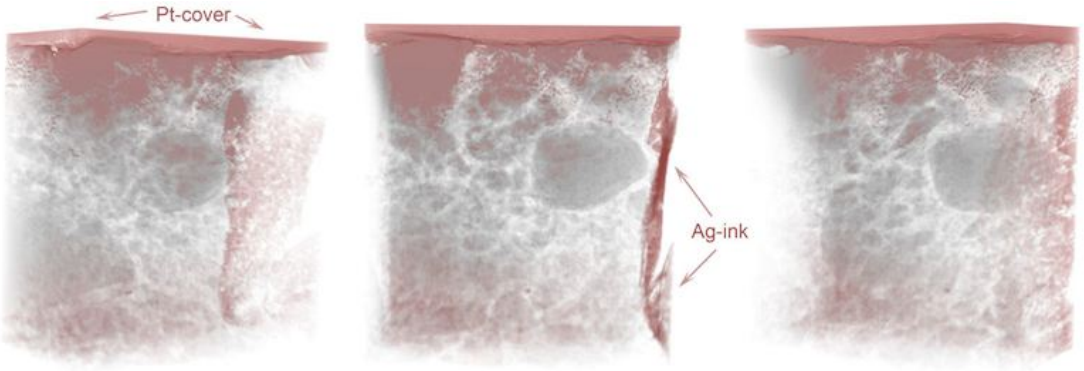

Figure 6.10: *3-D reconstruction of a printed silicon layer from 3 different view points.*

FIB/SEM as discussed in Chapter 3.2.2. The reconstruction was created, using 618 individual slices with a thickness of 11 nm. After imaging the data were processed as discussed in chapter 3.2.2. Fig. 6.10 shows the results of the reconstruction, using UCSF Chimera version 1.8. Platinum used to protect the printed layer during FIB

is visible on top of the printed layer. The dark red feature on the right of the centre image (marked with the arrows) is the silver contact of the diode as seen in Fig. 6.8(b) and Fig. 6.9. The 3D-data reveal that the particles indeed form a dense network of large clusters and clusters of clusters, which form an interlocking layer. Furthermore it can be seen that although the printed silicon layer is porous, it forms well defined percolation paths in 3 dimensions throughout the print which allows the observed charge transport throughout the printed devices.

7 Conclusion

The results presented in this thesis show that the devices printed on paper substrate are Schottky barrier diodes, and hence a crucial component in printed electronics, which has not been reported in literature so far, has been successfully developed. The best diode characteristics were observed for devices produced using highly doped silicon nanoparticles in a water based acrylic binder. These diodes, printed with carbon as the anode, and silver as the cathode, have a lower saturation current density and ideality factor compared to the other types of diodes produced, because it is the silver that forms a ohmic contact with highly doped silicon. The other types of diodes, which have low doped silicon, show a more symmetric I-V curve and have higher values for the saturation current density and ideality factor. The saturation current density in the diodes fabricated with highly doped silicon results in a lower current under reverse bias. For forward bias, a low ideality factor enables a more rapid exponential increase in conduction with voltage applied. Therefore as the value of these parameters decrease it shows that quality of the diode improves. However, using solvent based inks, it was only possible to produce asymmetric, non-rectifying diodes even when using highly doped silicon nanoparticles.

In this thesis previous microscopy studies have been extended to investigate the surface of the silicon nanoparticles in both the original powder and, more importantly, for the first time the printed layers. In particular, detailed information of the internal structure and the investigation of the surface of silicon nanoparticles allowed the analysis of the ability of the particles to form a percolation path in the printed layers. Using the *T*EAM 0.5 instrument, it could be shown with high resolution transmission electron microscopy (HRTEM) that the particles are not capped with a thick oxide layer but that there is a thin disordered layer with a maximum thickness

of approximately 5Å at the surface of the silicon nanoparticles.
Furthermore, a rigorous HRTEM study on a lamella of a printed layer revealed that the particles are in close contact, which is the requirement for percolation driven charge transport. But the most important feature of the silicon nanoparticles revealed in this work is that no surface oxide is formed in aqueous environments, which makes the particles solution processable, and therefore printable, without losing their semiconducting properties. Additionally to the HRTEM micrographs, elemental mapping using high-angle annular dark-field images obtained with a scanning transmission electron microscope (HAADF STEM) showed that there is only an incomplete layer of oxygen on top of the silicon nanoparticles, and furthermore it revealed that generally there is only a low oxygen content at the silicon nanoparticles. To compliment the microscopic techniques used, 3-D tomographic reconstructions of a single nanoparticle cluster and a printed silicon layer have been performed. Using this technique it could be shown that the particles have in general smooth faceted surfaces. The same result was found for the printed layer which forms a 3 dimensional network of interconnected clusters, thus allowing charge transport through a percolation path.
To investigate the change in carrier density and/or mobility IR s-SNOM has been performed. It could be shown that the carrier concentration in the nanoparticles, compared to the feedstock used, is not significantly changed by the production process. However, from the reduced amplitude and phase signals observed, there is an indication of a reduced carrier mobility of the high-frequency (i. e. infrared) mobility at 30 THz on the surface of large particles. Further investigation will be needed because DC mobility might be affected differently.

The relationship between the microscale as well as nanoscale features and the electrical properties is still an open ended question. This thesis has shown that silicon nanoparticles produced by high energy milling can be utilized for the production of Schottky barriers and that the surface properties of the particles are related to the electrical properties of the layers produced by using these silicon nanoparticulate system. Similar approaches should be used to study other nanoparticles used in electronic ink systems.

For future work it would be helpful to investigate if the irregularity of the silicon nanoparticle shape and size distribution has an influence on the performance of the devices produced. Therefore it could be investigated if more regular crystallites produce better performance or if a tighter size distribution results in a better percolation. Additionally it could be investigated what techniques beyond high-energy milling could be used to produce silicon nanoparticles for electronic applications. This might give an insight to the question if roughly spherical particles would perform better. To some extend this has been done in early structural [35, 76, 79] and electrical [189, 190] studies with nanoparticles produced by chemical vapour synthesis. Furthermore it should be investigated if liquid phase chemical synthesis results in usable nanoparticles or if nanoparticle surface functionalisation results in electrically inactive films, or if there are other means to produce silicon nanoparticles that might result in a better electronic material. Other important future studies would be the investigation of how to produce better electrical contacts with the printed silicon layer to enhance the diode performance.

Appendix

A. Devices printed for this thesis

For this thesis two different types of inks were produced, namely solvent and water based acrylic inks. In Tab. A.1 devices printed using the solvent based ink are listed. For these devices ETHOCEL^{TM} ethyl cellulose and CELLOSOLVE^{TM} butyl (Dow Chemical) were used as the binder and solvent respectively.

material combination			**binder**	**layout**	**substrate**	#
bottom contact	silicon nanoparticles	top contact				
custom Ag NP	P-type B $< 0.001\,\Omega cm$	custom graphene	solvent	opposed	paper	60
custom Ag NP	P-type B $< 0.001\,\Omega cm$	custom carbon nanotubes	solvent	opposed	paper	60
custom Ag NP	N-type Ph $0.001 - 0.00102\,\Omega cm$	custom graphene	solvent	opposed	paper	60
custom Ag NP	N-type Ph $0.001 - 0.00102\,\Omega cm$	custom carbon nanotubes	solvent	opposed	paper	60

Table A.1: *Overview of all devices printed using solvent based ink for this work.*

For the water based acrylic ink, two different designs were printed. Firstly the lateral design and secondly a opposed design. The devices printed using these designs are listed in Tab. A.2 and Tab. A.3 respectively.

material combination			binder	layout	substrate	#
bottom contact	silicon nanoparticles	top contact				
Canatu carbon nanotubes	P-type B $< 0.005\,\Omega cm$	aluminium tape	acrylic	lateral	PET	5
Canatucarbon nanotubes	P-type B $< 0.005\,\Omega cm$	Dupont 5000 silver	acrylic	lateral	PET	10
Dupont 5000 silver	P-type B $< 0.005\,\Omega cm$	Dupont 7164 TCO	acrylic	lateral	paper	120
PChem PSI-211	P-type B $< 0.005\,\Omega cm$	Dupont 7164 TCO	acrylic	lateral	paper	30
Dupont 5000 silver	P-type B $< 0.005\,\Omega cm$	custom carbon NP	acrylic	lateral	paper	90
PChem PSI-211	P-type B $< 0.005\,\Omega cm$	custom carbon NP	acrylic	lateral	paper	30
Dupont 5000 silver	P-type B $< 0.005\,\Omega cm$	Dupont 7102 carbon	acrylic	lateral	paper	90
PChem PSI-211	P-type B $< 0.005\,\Omega cm$	Dupont 7102 carbon	acrylic	lateral	paper	30
Dupont 5000 silver	N-type Ph $0.008 - 0.02\,\Omega cm$	Dupont 7164 TCO	acrylic	lateral	paper	120
PChem PSI-211	N-type Ph $0.008 - 0.02\,\Omega cm$	Dupont 7164 TCO	acrylic	lateral	paper	40
Dupont 5000 silver	N-type Ph $0.008 - 0.02\,\Omega cm$	custom carbon NP	acrylic	lateral	paper	90
PChem PSI-211	N-type Ph $0.008 - 0.02\,\Omega cm$	custom carbon NP	acrylic	lateral	paper	40
Dupont 5000 silver	N-type Ph $0.008 - 0.02\,\Omega cm$	Dupont 7102 carbon	acrylic	lateral	paper	90
PChem PSI-211	N-type Ph $0.008 - 0.02\,\Omega cm$	Dupont 7102 carbon	acrylic	lateral	paper	90

Table A.2: *Overview of all devices using acrylic binder an lateral design printed for this work.*

material combination			binder	layout	substrate	#
bottom contact	silicon nanoparticles	top contact				
Dupont 5000 silver	2503 metallurgical grade silicon	Dupont 7102 carbon	acrylic	opposed	paper	150
Dupont 5000 silver	2503 metallurgical grade silicon	Dupont 7164 TCO	acrylic	opposed	paper	150
Dupont 5000 silver	P-type B $1 - 10\,\Omega cm$	Dupont 7102 carbon	acrylic	opposed	paper	150
Dupont 5000 silver	P-type B $1 - 10\,\Omega cm$	Dupont 7164 TCO	acrylic	opposed	paper	150
PChem PSI-211	P-type B $1 - 10\,\Omega cm$	Dupont 7102 carbon	acrylic	opposed	paper	150
PChem PSI-211	P-type B $1 - 10\,\Omega cm$	Dupont 7164 TCO	acrylic	opposed	paper	150
Dupont 5000 silver	P-type B $< 0.005\,\Omega cm$	Dupont 7164 TCO	acrylic	opposed	paper	60
Dupont 5000 silver	P-type B $< 0.005\,\Omega cm$	custom carbon NP	acrylic	opposed	paper	60
Dupont 5000 silver	P-type B $< 0.005\,\Omega cm$	Dupont 7102 carbon	acrylic	opposed	paper	60
PChem PSI-211	P-type B $< 0.005\,\Omega cm$	Dupont 7102 carbon	acrylic	opposed	paper	60
PChem PSI-211	P-type B $< 0.005\,\Omega cm$	Dupont 7164 TCO	acrylic	opposed	paper	60
Dupont 5000 silver	P-type B $< 0.001\,\Omega cm$	Dupont 7102 carbon	acrylic	opposed	paper	120
Dupont 5000 silver	P-type B $< 0.001\,\Omega cm$	Dupont 7164 TCO	acrylic	opposed	paper	120
PChem PSI-211	P-type B $< 0.001\,\Omega cm$	Dupont 7102 carbon	acrylic	opposed	paper	120
PChem PSI-211	P-type B $< 0.001\,\Omega cm$	Dupont 7164 TCO	acrylic	opposed	paper	120
Dupont 5000 silver	N-type Ph $1 - 10\,\Omega cm$	Dupont 7102 carbon	acrylic	opposed	paper	150
Dupont 5000 silver	N-type Ph $1 - 10\,\Omega cm$	Dupont 7164 TCO	acrylic	opposed	paper	150
PChem PSI-211	N-type Ph $1 - 10\,\Omega cm$	Dupont 7102 carbon	acrylic	opposed	paper	150
PChem PSI-211	N-type Ph $1 - 10\,\Omega cm$	Dupont 7164 TCO	acrylic	opposed	paper	150
Dupont 5000 silver	N-type Ph $0.008 - 0.02\,\Omega cm$	Dupont 7164 TCO	acrylic	opposed	paper	60
Dupont 5000 silver	N-type Ph $0.008 - 0.02\,\Omega cm$	custom carbon NP	acrylic	opposed	paper	60
Dupont 5000 silver	N-type Ph $0.008 - 0.02\,\Omega cm$	Dupont 7102 carbon	acrylic	opposed	paper	60
PChem PSI-211	N-type Ph $0.008 - 0.02\,\Omega cm$	Dupont 7102 carbon	acrylic	opposed	paper	60
PChem PSI-211	N-type Ph $0.008 - 0.02\,\Omega cm$	Dupont 7164 TCO	acrylic	opposed	paper	60
Dupont 5000 silver	N-type Ph $0.001 - 0.00102\,\Omega cm$	Dupont 7102 carbon	acrylic	opposed	paper	120
Dupont 5000 silver	N-type Ph $0.001 - 0.00102\,\Omega cm$	Dupont 7164 TCO	acrylic	opposed	paper	120
PChem PSI-211	N-type Ph $0.001 - 0.00102\,\Omega cm$	Dupont 7102 carbon	acrylic	opposed	paper	120
PChem PSI-211	N-type Ph $0.001 - 0.00102\,\Omega cm$	Dupont 7164 TCO	acrylic	opposed	paper	120

Table A.3: *Overview of all devices using acrylic binder printed in opposed design.*

Acknowledgements

I would like to thank associate Prof. M. Härting and Prof. D. T. Britton for supervising my thesis. Prof. Brittons contributions improved the quality of this work.

The acting heads of department Prof. David Ashmann and Prof. Andy Buffler I thank for the opportunity to work and to carry out my experiments in the department of physics at the University of Cape Town and the great support.

My special thanks I want to express to Andrey Chuvilin for his significant contribution to the microscopy work in this thesis and my mentor for the s-snom experiments Dr. Rainer Hillenbrand. I am thankful for the numerous ideas and motivating suggestions, the inspiring discussions and the constructive criticism about my conducted projects and the scientific presentation of my results. I'm deeply indebted to them for giving me the opportunity to work in the exciting environment of the electron microscopy unit and the nano-optics group at CIC nanoGUNE in San Sebastian, in an optimal working atmosphere. The constructive discussions of my projects, their suggestion and ideas for further experiments and the recommendations to the manuscript greatly improved the quality of the presented work.

I would like to thank Mohammed A. Jaffer and Miranda Waldron for the introduction into TEM and SEM and the help for imaging my samples at the electron microscopy unit at the UCT. Especially I want to highlight their patience with me and all the different samples and requests for imaging specimens.

Prof. Mark Blumental has brought many times new insights into nanomaterials and solid-state physics to me. His vast experience in solid state physics was always of big help. I appreciate very much that Prof. Mark Blumental gave me the chance to get strong motivation to carry out the interesting projects. His recommendations to the manuscript improved the quality of the presented work as well.

I am thankful to Christopher Tollan for the help with the FIB/SEM and especially for the great support with sample preparation. Especially I want to highlight his patience to produce all samples I asked for.

Special thanks also to Dr. Andreas Huber from Neaspec GmbH, Dr. Alexander A. Govyadinov, Dr. Martin Schnell, Iban Amenabar and Paulo Sarriugarte for the introduction into s-SNOM and the warm welcome at the nano-optics group at CIC nanoGUNE. Also for the help with the data analysis and very fruitful discussions about my scientific projects. I am grateful to them for the support and the wonderful working atmosphere during my visits in Munich and San Sebastian.

I am thankful to all the present and past members of the NanoSciences Innovation Centre, including Dr. Batsirai Magunje, Dr. Emmanuel Jonah, Dr. Rudolf Nüssl, Stephen Jones, Stanley Walton, Claire van den Berg and Serges Zambou. I would like to thank all of them for the very inspiring atmosphere in our group, the support in the lab as well as the occasional distractions from scientific questions when needed.

I want to thank Dr. Elena Bailo and Dr. Ute Schmidt from WITec GmbH for the support with Raman spectroscopy and the chance to carry out some experiments in Ulm.

Thanks also to the developers of UCSF Chimera for providing an open source 3-D visualisation software. Chimera is developed by the Resource for Biocomputing, Visualization, and Informatics at the University of California, San Francisco (supported by NIGMS P41-GM103311).

I also acknowledge the support of the National Center for Electron Microscopy, Lawrence Berkeley Lab, which is supported by the U.S. Department of Energy under Contract # DE-AC02-05CH11231. Special thanks goes to Dr. Jim Ciston and Peter Ercius for the warm welcome and the collaboration with the TEAM 0.5.

I thank the University of Cape Town for the financial support through the UCT Travel Grant and the Max and Lille Sonnenberg Scholarship which gave me the change to attend scientific conferences and establish a close collaboration with CIC nanoGUNE in San Sebastian, Spain. Additionally it lead to many valuable international contacts and interesting projects.

Cape Town, October 2014. Ulrich Männl

References

[1] M. Berggren, N. Nilsson, and N. D. Robinson, *Organic materials for printed electronics*, Nat. Mat. **6** (2007) 3-5. DOI: 10.1038/nmat1817

[2] A. C. Arias, J. D. MacKenzie, I. McCulloch, J. Rivnay, and A. Salleo, *Materials and Applications for Large Area Electronics: Solution-Based Approaches*, Chem. Rev. **110** (2010) 3-24. DOI: 10.1021/cr900150b

[3] Y. Kumashiro, H. Nakako, M. Inada, K. Yamamoto, A. Izumi, and M. Ishihara, *Novel materials for electronic device fabrication using ink-jet printing technology*, Appl. Surf. Sci. **256** (2009) 1019-1022. DOI: 10.1016/j.apsusc.2009.05.134

[4] P. Duan, O. Raz, B. Smalbrugge, J. Duis, and H. Dorren, *A Novel 3D Stacking Method for Opto-Electronic Dies on CMOS ICs*, Opt. Express **20** (2012) B386-B392. DOI: 10.1364/OE.20.00B386

[5] J. Y.-C. Sun, *System Scaling and Collaborative Open Innovation*, VLSI Technology (VLSIT), 2013 Symposium on (2013) T2-T7. ISSN : 0743-1562

[6] S. Ju, A. Facchetti, Y. Xuan, J. Liu, F. Ishikawa, P. Ye, C. Zhou, T. J. Marks, and D. B. Janes, *Fabrication of fully transparent nanowire transistors for transparent and flexible electronics*, Nat. Nanotechnol. **2** (2007) 378-384. DOI: 10.1038/nnano.2007.151

[7] A. Hanson, British Patent 4861 (1903).

[8] C. E. Marlies, *Electrical Circuits on Plastics and other Nonconductors*, Proceedings of the First Technical Symposium on Printed Circuits, New Advances in Printed Circuits **192** (1948) 36-40.

[9] J. Perelaer, P. J. Smith, D. Mager, D. Soltman, S. K. Volkman, V. Subramanian, J. G. Korvink, and U. S. Schubert, *Printed electronics: the challenges involved in printing devices, interconnects, and contacts based on inorganic materials*, J. Mater. Chem. **20** (2010) 8446-8453. DOI: 10.1039/C0JM00264J

[10] S. Jeong, S. H. Lee, Y. Jo, S. S. Lee, Y.-H. Seo, B. W. Ahn, G. Kim, G.-E. Jang, J.-U. Park, B.-H. Ryua, and Y. Choi, *Air-stable, surface-oxide free Cu nanoparticles for highly conductive Cu ink and their application to printed graphene transistors*, J. Mater. Chem. C **1** (2013) 2704-2710. DOI: 10.1039/C3TC00904A

[11] L. Grande, V. T. Chundi, D. Wei, C. Bower, P. Andrew, and T. Ryhänen, *Graphene for energy harvesting/storage devices and printed electronics*, Particuology, **10** (2012) 1-8. DOI: 10.1016/j.partic.2011.12.001

[12] L. Huang, Y. Huang, J. Liang, X. Wan, and Y. Chen, *Graphene-based conducting inks for direct inkjet printing of flexible conductive patterns and their applications in electric circuits and chemical sensors*, Nano Research **4** (2011) 675-684. DOI: 10.1007/s12274-011-0123-z

[13] J.-H. Chen, M. Ishigami, C. Jang, D. R. Hines, M. S. Fuhrer, and E. D. Williams, *Printed Graphene Circuits*, Adv. Mater. **19** (2007) 3623–3627. DOI: 10.1002/adma.200701059

[14] Q. Cao, and J. A. Roger, *Ultrathin Films of Single-Walled Carbon Nanotubes for Electronics and Sensors: A Review of Fundamental and Applied Aspects*, Adv. Mater. **21** (2009) 29-53. DOI: 10.1002/adma.200801995

[15] J. F. Wager, *Transparent Electronics*, Science **300** (2003) 1245-1246. DOI: 10.1126/science.1085276

[16] R. L. Hoffmann, B. J. Norris, and J. F. Wager, *ZnO-based transparent thin-film transistors*, Appl. Ph.D.s. Lett. **82** (2003) 733-735. DOI: 10.1063/1.1542677

[17] X. Li, W. Cai, J. An, S. Kim, J. Nah, D. Yang, R. Piner, A. Velamakanni, I. Jung, E. Tutuc, S. K. Banerjee, and Luigi Colombo, *Large-Area Synthesis of High-Quality and Uniform Graphene Films on Copper Foils*, Science **324** (2009) 1312-1314. DOI: 10.1126/science.1171245

[18] T. Sekitani, and T. Someya, *Stretchable, Large-area Organic Electronics*, Adv. Mater. **22** (2010) 2228-2246. DOI: 10.1002/adma.200904054

[19] G. Eda, G. Fanchini, and M. Chhowalla, *Large-area ultrathin films of reduced graphene oxide as a transparent and flexible electronic material*, Nat. Nanotechnol. **3** (2008) 270-274. DOI: 10.1038/nnano.2008.83

[20] F. Eder, H. Klauk, M. Halik, U. Zschieschang, G. Schmid, and C. Dehm, *Organic electronics on paper*, Apply. Phys. Lett. **84** (2004) 2673-2675. DOI: 10.1063/1.1690870

[21] M. Chason, P. W. Brazis, J. Zhang, K. Kalyanasundaram, and D. R. Gamota, *Printed Organic Semiconducting Devices*, Proceedings of the IEEE **93** (2005) 1348-1356. DOI: 10.1109/JPROC.2005.850306

[22] D. R. Gamota, P. Brazis, K. Kalyanasundaram, and J. Zhang, *Printed organic and molecular electronics*, Springer 1st edition (2004).

[23] E. H. Nicollian, J. R. Brews, *MOS Metal oxide semicondutor physics and technology*, Wiley-Interscience, (1982).

[24] D. Kim, S. Jeong, J. Moon, and K. Kang, *Ink-Jet Printing of Silver Conductive Tracks on Flexible Substrates*, Mol. Cryst. Liq. Cryst., **459** (2006) 45/[325]-55[335]. DOI: 10.1080/15421400600930458

[25] H. Hillebrandt, and M. Tanaka, *Electrochemical Characterization of Self-Assembled Alkylsiloxane Monolayers on Indium Tin Oxide (ITO) Semiconductor Electrodes*, J. Phys. Chem. B **105** (2001) 4270–4276. DOI: 10.1021/jp004062n

[26] T. Karasawa, and Y. Miyata, *Electrical and optical properties of indium tin oxide thin films deposited on unheated substrates by d.c. reactive sputtering*, Thin Solid Films **223** (1993) 135–139. DOI: 10.1016/0040-6090(93)90737-A

[27] K. S. Kim, Y. Zhao, H. Jang, S. Y. Lee, J. M. Kim, K. S. Kim, J.-H. Ahn, P. Kim, J.-Y. Choi, and B. H. Hong, *Large-scale pattern growth of graphene films for stretchable transparent electrodes*, Nature **457** (2009) 706–710. DOI: 10.1038/nature07719

[28] S. Holdcroft, *Patterning π-Conjugated Polymers*, Adv. Mater **13** (2001) 1753–1765. DOI: 10.1002/1521-4095(200112)13:23<1753::AID-ADMA1753>3.0.CO;2-2

[29] S. E. Shaheen, R. Radspinner, N. Peyghambarian, and G. E. Jabbour, *Fabrication of bulk heterojunction plastic solar cells by screen printing*, Appl. Phys. Lett. **79** (2001) 2996-2998. DOI: 10.1063/1.1413501

[30] J. Nelles, D. Sendor, F.-M. Petrat, and U. Simon, *Electrical properties of surface functionalized silicon nanoparticles*, J. Nanopart. Res. **12** (2010) 1367-1375. DOI: 10.1007/s11051-009-9676-0

[31] T. Shimoda, Y. Matsuki, M. Furusawa, T. Aoki, I. Yudasaka, H. Tanaka, H. Iwasawa, D. Wang, M. Miyasaka, and T. Takeuchi, *Solution-processed silicon films and transistors*, Nature **440** (2006) 783-786. DOI: 10.1038/nature04613

[32] H. Li, Z. Xie, Y. Zhang, and J. Wang, *The effects of ethyl cellulose on PV performance of DSSC made of nanostructured ZnO pastes*, Thin Solid Films **518** (2010) e68-e71. DOI: 10.1016/j.tsf.2010.03.125

[33] J.-G. Nam, E.-S. Lee, W.-C. Jung, Y.-J. Park, B.-H. Sohn, S.-C. Park, J. S. Kim, and J.-Y. Bae, *Photovoltaic enhancement of dye-sensitized solar cell prepared from [TiO2/ethyl cellulose/terpineol] paste employing TRITON^{TM} X-based surfactant with carboxylic acid group in the oxyethylene chain end*, Mater. Chem. Phys **116** (2009) 46-51. DOI: 10.1016/j.matchemphys.2009.02.037

[34] T.-X. Liang, W. Z. Sun, L.-D. Wang, Y. H. Wang, and H.-D. Li, *Effect of Surface Energies on Screen Printing Resolution*, IEEE T. Compon. Pack. B **19** (1996) 423-426. DOI: 10.1109/96.496047

[35] D. T. Britton, and M. Härting, *Printed nanoparticulate composites for silicon thick-film electronics*, Pure Appl. Chem. **78** (2006) 1723-1739. DOI: 10.1351/pac200678091723

[36] D. T. Britton, E. A. Odo, G. Gonfa, E. O. Jonah, and M. Härting, *Size distribution and surface characteristics of silicon nanoparticles*, J. Appl. Crystall. **42** (2009) 448-456. DOI: 10.1107/S0021889809011947

[37] M. Härting, J. Zhang, D. R. Gamota, and D. T. Britton, *Fully printed silicon field effect transistors*, Appl. Phys. Lett. **94** (2009) 193509. DOI: 10.1063/1.3126958

[38] U. Männl, B. Magunje, C. van den Berg, D.T. Britton, and M. Härting, *Electronic Devices Based on Printed Silicon Nanoparticles*, Proc. of the International Conference Nanomaterials: Applications and Properties, **1** (2012) 01PCN03. 2304-1862/2012/1(1)01PCN03(3)

[39] U. Männl, A. Chuvilin, B. Magunje, E. O. Jonah, M. Härting, and D. T. Britton, *Interfacial and network characteristics of silicon nanoparticle layers used in printed electronics*, Jpn. J. Appl. Phys. **52** (2013) 05DA11. DOI: 10.7567/JJAP.52.05DA11

[40] D. Tobjörk, and R. Österbacka, *Paper Electronics*, Adv. Mater. **23** (2011) 1935-1961. DOI: 10.1002/adma.201004692

[41] J. F. Wager, *Transparent electronics: Schottky barrier and heterojunction considerations*, Thin Solid Films **516** (2008) 1755-1764. DOI: 10.1016/j.tsf.2007.06.164

[42] C. H. Chen, S. J. Chang, Y. K. Su, G. C. Chi, J. Y. Chi, C. A. Chang, J. K. Sheu, and J. F. Chen, *GaN metal-semiconductor-metal ultraviolet photodetectors with transparent indium-tin-oxide Schottky contacts*, Photon. Technol. Lett. **13** (2001) 848-850. DOI: 10.1109/68.935824

[43] T-Y. Oh, S. W. Jeong, S. Chang, K. Choi, H. J. Ha, and B. K. Ju, *The silicon Schottky diode on flexible substrates by transfer method*, Appl. Phys. Lett. **102** (2013) 021106. DOI: 10.1063/1.4776685

[44] Y. Li, and C.-H. Hwang, *Nanoscale Transistors*, Comprehensive Nanoscience and Technology **4.17** (2011) 489-560. DOI: 10.1016/B978-0-12-374396-1.00139-2

[45] R. V. Seidel, A. P. Graham, J. Kretz, B. Rajasekharan, G. S. Duesberg, M. Liebau, E. Unger, F. Kreupl, and W. Hoenlein, *Sub-20 nm Short Channel Carbon Nanotube Transistors*, Nano Lett. **5** (2005) 147-150. DOI: 10.1021/nl048312d

[46] M. N. Shkunov, W. Zhang, C. Bailey, B. Fleming, M. Giles, M. Heeney, I. Love, D. Sparrowe, S. Tierney, I. McCulloch, M. M. Nielsen, D. W. Breiby, and O. Bunk, *Self-assembled liquid crystalline solution processable semiconductors*, Proc. SPIE **5464** (2004) 60. DOI: 10.1117/12.545729

[47] K. Gilleo, *Rheology and Surface Chemistry for Screen Printing*, Screen Printing Magazine (1989).

[48] K. Woo, D. Kim, J. S. Kim, S. Lim, and J. Moon *Ink-Jet Printing of Cu-Ag-Based Highly Conductive Tracks on a Transparent Substrate*, Langmuir **25** (2009) 429-433. DOI: 10.1021/la802182y

[49] M. Mastropietro, *Cost Effective Patterning of Conductors Utilizing Silver Nanoparticle Inks with Traditional Printing Processes*, Lope-C proceedings (2011).

[50] J. R. Panda, and R. S. Kshetrimayum, *A printed 2.4 GHz/5.8 GHz dual-band monopole antenna with a protruding stub in the ground plane for WLAN and RFID applications*, Pr. Electromagn. Res., **117** (2011) 425-434. DOI: 10.2528/PIER11051301

[51] V. Lakafosis, A. Rida, R. Vyas, L. Yang, S. Nikolaou, and M. M. Tentzeris, *Progress Towards the First Wireless Sensor Networks Consisting of Inkjet-Printed, Paper-Based RFID-Enabled Sensor Tags*, Proc. of the IEEE **98** (2010) 1601-1609. DOI: 10.1109/JPROC.2010.2049622

[52] F. N. Ishikawa, H.-K. Chang, K. Ryu, P.-C. Chen, A. Badmaev, L. G. De Arco, G. Shen, and C. Zhou, *Transparent Electronics Based on Transfer Printed Aligned Carbon Nanotubes on Rigid and Flexible Substrates*, ACS Nano, **3** (2009) 73-79. DOI: 10.1021/nn800434d

[53] S. Günes, H. Neugebauer, and N. S. Sariciftci, *Conjugated Polymer-Based Organic Solar Cells*, Chem. Rev. **107** (2007) 1324-1338. DOI: 10.1021/cr050149z

[54] H. Yan, Z. Chen, Y. Zheng, C. Newman, J. R. Quinn, F. Dötz, M. Kastler, and A. Facchetti, *A high-mobility electron-transporting polymer for printed transistors*, Nature **457** (2009) 679-686. DOI: 10.1038/nature07727

[55] Z. Bao, J. A. Rogers, and H. E. Katz, *Printable organic and polymeric semiconducting materials and devices*, J. Mater. Chem. **9** (1999) 1895-1904. DOI: 10.1039/A902652E

[56] V. Subramanian, P. C. Chang, J. B. Lee, S. E. Molesa, and S. K. Volkman, *Printed organic transistors for ultra-low-cost RFID applications*, IEEE T. Compon. Pack. T. **28** (2005) 742 - 747. DOI: 10.1109/TCAPT.2005.859672

[57] K. Reuter, H. Kempa, N. Brandt, M. Bartzsch, A.C. Huebler, *Influence of process parameters on the electrical properties of offset printed conductive polymer layers*, Prog.Org. Coat. **58** (2007) 312-315. DOI: 10.1016/j.porgcoat.2007.01.004

[58] V. Subramanian, J.B Chang,A. de la Fuente Vornbrock, D. C. Huang, L. Jagannathan, F. Liao, B. Mattis, S. Molesa, D. R. Redinger, D. Soltman, S. K. Volkman, and Z. Qintao, *Printed electronics for low-cost electronic systems: Technology status and application development*, 34th European Solid-State Circuits Conference (2008) 17-24. DOI: 10.1109/ESSCIRC.2008.4681785

[59] D. Tilles, *Natural variations in isotopic abundances of silicon*, J. Geophys. Res. **66** (1961) 3003-3013. DOI: 10.1029/JZ066i009p03003

[60] R. Martonák, D. Donadio, A. R. Oganov, and M. Parrinello, *Crystal structure transformations in SiO2 from classical and ab initio metadynamics*, Nat. Mat. **5** (2006) 623-626. DOI: 10.1038/nmat1696

[61] Prof. Dr. K. Wüst, *Naturwissenschaftliche und technische Grundlagen (NTG, Modul MN1008) Ergänzungsskript*, (2011).

[62] W. Kowalsky, *Dielektrische Werkstoffe der Elektronik und Photonik*, Teubner Studienbücher Physik (German Edition), B.G. Teubner Verlag, (1994).

[63] Poster presentation "Crystalline Silicon", www.microchemicals.eu, Microchemicals GmbH (2012), accessed 2013-07-09.

[64] E. Kaxiras, *Effect of surface reconstruction on stability and reactivity of Si clusters*, Phys. Ref. Lett. **64** (1990) 551-554. DOI: 10.1103/PhysRevLett.64.551

[65] P. Woditscha, W. Koch, *Solar grade silicon feedstock supply for PV industry*, Sol. Energ. Mat. Sol. C. **72** (2002) 11-26. DOI: 10.1016/S0927-0248(01)00146-5

[66] T. Nohira, K. Yasuda, and Y. Ito, *Pinpoint and bulk electrochemical reduction of insulating silicon dioxide to silicon*, Nat. Mat. **2** (2003) 397-401. DOI: 10.1038/nmat900

[67] N. Yuge1, M. Abe, K. Hanazawa, H. Baba, N. Nakamura, Y. Kato, Y. Sakaguchi, S. Hiwasa, and F. Aratani, *Purification of Metallurgical Grade Silicon up to Solar Grade*, Prog. Photovolt: Res. Appl. **9** (2001) 203-209. DOI: 10.1002/pip.372

[68] Berta Domènech, J. Bastos-Arrieta, A. Alonso, J. Macanás, M. Muñoz, and D. N. Muraviev, *Bifunctional Polymer-Metal Nanocomposite Ion Exchange Materials*, Chapter 3, INTech Books, Ion Exchange Technologies, Editor Ayben Kilislioğlu, (2012).

[69] L. Mazzola, *Commercializing nanotechnology*, Nat. Biotechnol. **21** (2003) 1137-1143. DOI: 10.1038/nbt1003-1137

[70] A. T. Heitsch, V. A. Akhavan, and B. A. Korgel, *Rapid SFLS Synthesis of Si Nanowires Using Trisilane with In situ Alkyl-Amine Passivation*, Chem. Mater. **23** (2011) 2697–2699 DOI: 10.1021/cm2007704

[71] R. K. Baldwin, K. A. Pettigrew, J. C. Garno, P. P. Power, G.-Y. Liu, and S M. Kauzlarich *Room Temperature Solution Synthesis of Alkyl-Capped Tetrahedral Shaped Silicon Nanocrystals*, J. Am. Chem. Soc. **124** (2002) 1150-1151 DOI: 10.1021/ja017170b

[72] C.-S. Yang, R. A. Bley, S. M. Kauzlarich, H. W. H. Lee, and G. R. Delgado, *Synthesis of Alkyl-Terminated Silicon Nanoclusters by a Solution Route*, J. Am. Chem. Soc. **121** (1999) 5191-5195 DOI: 10.1021/ja9828509

[73] J. D. Holmes, K. J. Ziegler, R. C. Doty, L. E. Pell, K. P. Johnston, and B. A. Korgel *Highly Luminescent Silicon Nanocrystals with Discrete Optical Transitions*, J. Am. Chem. Soc. **123** (2001) 3743-3748 DOI: 10.1021/ja002956f

[74] V. C. Holmberg, T. D. Bogart, A. M. Chockla, C. M. Hessel, and B. A. Korgel *Optical Properties of Silicon and Germanium Nanowire Fabric*, J. Phys. Chem. **116** (2012) 22486-22491 DOI: 10.1021/jp308231w

[75] R. A. Bley, S. M. Kauzlarich, J. E. Davis, and H. W. H. Lee, *Characterization of Silicon Nanoparticles Prepared from Porous Silicon*, Chem. Mater. **8** (1996) 1881-1888. DOI: 10.1021/cm950608k

[76] M.R. Scriba, D.T. Britton, and M. Härting, *Electrically active, doped monocrystalline silicon nanoparticles produced by hot wire thermal catalytic pyrolysis*, Thin Solid Films **519** (2011) 4491-4494. DOI: 10.1016/j.tsf.2011.01.330

[77] A.A. Onischuk, A.I. Levykin, V.P. Strunin, M.A. Ushakova, R.I. Samoilova, K.K. Sabelfeld, V.N. Panfilov *Aerosol formation under heterogenous/homogenous thermal decomposition of silane: experiment and numerical modeling*, J. Aeros. Sci. **31** (2000) 879-906 DOI: 10.1016/S0021-8502(99)00562-5

[78] A. S. Edelstein, and R. C. Cammarata, *Nanomaterials: Synthesis, properties and applications* Taylor and Francis Group (1996)

[79] M.R. Scriba, D.T. Britton, and M. Härting, *Electrically active, doped monocrystalline silicon nanoparticles produced by hot wire thermal catalytic pyrolysis*, Thin Solid Films **519** (2011) 4491-4494. DOI: 10.1016/j.tsf.2011.01.330

[80] P. Baláž, *High energy milling*, Mechanochemistry in Nanoscience and Minerals Engineering, Springer (2008).

[81] S. Sato, and M. T. Swihart, *Propionic-Acid-Terminated Silicon Nanoparticles: Synthesis and Optical Characterization*, Chem. Mater. **18** (2006) 4083-4088 DOI: 10.1021/cm060750t

[82] X. Li, and P. W. Bohn, *Metal-assisted chemical etching in HF/H2O2 produces porous silicon*, Appl. Phys. Lett. **77** (2000) 2572-2574 DOI: 10.1063/1.1319191

[83] X. Li, *Metal assisted chemical etching for high aspect ratio nanostructures: A review of characteristics and applications in photovoltaics*, Curr. Opin. in Soid. St. M. **16** (2012) 71-81 DOI: 10.1016/j.cossms.2011.11.002

[84] C. Chartier, S. Bastide, and C.. Levy-Clement, *Metal-assisted chemical etching of silicon in HF–H2O2*, Electroch. Acta **53** (2008) 5509-5516 DOI: 10.1016/j.electacta.2008.03.009

[85] T. Hadjersi, N. Gabouze, N. Yamamoto, C. Benazzouz, and H. Cherag *Blue luminescence from porous layers produced by metal-assistedchemicaletchingonlow-dopedsilicon*, Vacuum **80** (2005) 366-370 DOI: 10.1016/j.vacuum.2005.06.013

[86] S. Schwyn, E. Garwin, A. Schmidt-Ott, *Aerosol genera- tion by spark discharge*, J. Aerosol. Sci. **19** (1988) 639-642 DOI: 10.1016/0021-8502(88)90215-7

[87] V. A. Vons, L. C. P. M. de Smet, D. Munao, A. Evirgen, E. M. Kelder, and A. Schmidt-Ott *Silicon nanoparticles produced by spark discharge*, J. Nanopart. Res. **13** (2011) 4867-4879 DOI: 10.1007/s11051-011-0466-0

[88] N. S. Tabrizi, Q. Xu, N. M. van der Pers, U. Lafont, A. Schmidt-Ott, *Synthesis of mixed metallic nanoparticles by spark discharge.*, J. Nanopart. Res. **11** (2009) 1209-1218 DOI: 10.1021/cm950608k

[89] B. H. Kear, and P. R. Strutt, *Chemical processing and applications for nanostructured materials*, Nanostruc. Mat. **6** (1995) 227-236 DOI: 10.1016/0965-9773(95)00046-1

[90] I. Umezu, H. Minami, H. Senoo, and A. Sugimura, *Synthesis of photoluminescent colloidal silicon nanoparticles by pulsed laser ablation in liquids*, J. Phys.: Conf. Ser. **59** (2007) 392–395 DOI: 10.1088/1742-6596/59/1/083

[91] T. Yoshida, S. Takeyama, Y. Yamada, and K. Mutoh, *Nanometer-sized silicon crystallites prepared by excimer laser ablation in constant pressure inert gas*, Appl. Phys. Lett. **68** (1996) 1772-1774 DOI: 10.1063/1.116662

[92] D.L. Zhang, *Processing of advanced materials using high-energy mechanical milling*, Prog. Mater. Sci. **49** (2004) 537-560. DOI: 10.1016/S0079-6425(03)00034-3

[93] D. K. Rai, G. Beaucage, E. O. Jonah, D. T. Britton, S. Sukumaran, S. Chopra, G. Goro Gonfa, and M. Härting, *Quantitative investigations of aggregate systems*, J. Chem. Phys. **137** (2012) 044311. DOI: 10.1063/1.4737947

[94] C. L. De Castro, and B. S. Mitchell, *Nanoparticles from Mechanical Attrition*, Chapter 1, American Scientific Publishers (2002).

[95] E. O. Jonah, D. T. Britton, P. Beaucage, D. K. Rai, G. Beaucage, B. Magunje, J. Ilavsky, M. R. Scriba, and M. Härting, *Topological investigation of electronic silicon nanoparticulate aggregates using ultra-small-angle X-ray scattering*, J. Nanopart. Res. **14** (2012) 14:1249. DOI: 10.1007/s11051-012-1249-y

[96] H. C. Ko, A. J. Baca, and J. A. Rogers, *Bulk Quantities of Single-Crystal Silicon Micro-/Nanoribbons Generated from Bulk Wafers*, Nano Letters **6** (2006) 2318-2324 DOI: 10.1021/nl061846p

[97] S. Mack, M. A. Meitl, A. J. Baca, Z.-T. Zhu, and J. A. Rogers, *Mechanically flexible thin-film transistors that use ultrathin ribbons of silicon derived from bulk wafers*, Appl. Phys. Lett. **88** (2006) 213101 DOI: 10.1063/1.2206688

[98] C. W. Mueller, and P. H. Robinson, *Grown-Film Silicon Transistors on Sapphire*, Proc. IEEE **52** (1964) 1487-1490. DOI: 10.1109/PROC.1964.3436

[99] E. C. Garnett, W. Liang, and P. Yang, *Growth and Electrical Characteristics of Platinum-Nanoparticle- Catalyzed Silicon Nanowires* Adv. Mater. **19** (2007) 2946-2950. DOI: 10.1002/adma.200700288

[100] G. Qin, H.-C. Yuan, H. Yang, W. Zhou, and Z. Ma, *High-performance flexible thin-film transistors fabricated using print-transferrable polycrystalline silicon membranes on a plastic substrate*, Semicond. Sci. Technol. **26** (2011) 025005. DOI: 10.1088/0268-1242/26/2/025005

[101] D. Karshtedt, J. Rockenberger, F. Zürcher, B. Ridley, and E. Scher, *Silicon polymers, methods of polymerizing silicon compounds, and methods of forming thin films from such silicon polymers*, US Patent 8 461284 B2 (2013). Google patents accessed 2014-06-22

[102] *Semiconductor sales to grow in 2008*, Electronics **5** (2007) 6-7. accessed 2014-06-23

[103] T. Shimoda, and T. Masuda, *Liquid silicon and its application in electronics*, Jap. J. Appl. Phys. **53** (2014) 02BA01. DOI: 10.7567/JJAP.53.02BA01

[104] T. Shimoda, Y. Matsuki, M. Furusawa, T. Aoki, I. Yudasaka, H. Tanaka, H. Iwasawa, D. Wang, M. Miyasaka, and Y. Takeuchi, *Solution-processed silicon films and transistors*, Nature **440** (2006) 783-786. DOI: 10.1038/nature04613

[105] S. D. Brotherton, *Polycrystallinesiliconthinfilm I transistors*, Semicond. Sci. Technol. **10** (1995) 721-738. DOI: 10.1088/0268-1242/10/6/001

[106] NanoGram Corporation press release, *NanoGram's ambient printed nanosilicon achieves mobility of 2cm2/Vs* Printed electronics World accessed 2014-06-21

[107] T. Tsuzuki, and P. G. McCormick, *Mechanochemical synthesis of nanoparticles* J. Mat. Sci., **39** (2004) 5143-5146. DOI: 10.1023/B:JMSC.0000039199.56155.f9

[108] E. A. Odo, *Synthesis, Characterisation and Device Application of Silicon Nanoparticles produced by Mechanical Attrition*, Ph.D. thesis, University of Cape Town (2009).

[109] B. Magunje, *Charge Transport in Printed Silicon Nanoparticle Networks*, Ph.D. thesis, University of Cape Town (2012).

[110] E. O. Jonah, *The topology and electrical properties of nanoparticle networks*, Ph.D. thesis, University of Cape Town (2013).

[111] A. P. Godse, and U. A. Bakshi, *Electronic Circuits -I*, Technical Publications, First Edition, *Rectifiers and Multipliers*, page 8-2 (2009)

[112] F. Thuselt, Physik der Halbleiterbauelemente (German edition), 1st edition Springer (2005)

[113] J. Lutz, Halbleiter-Leistungsbauelemente (German edition), 2nd edition, Springer Vieweg (2012)

[114] R. Paul, Halbleiterdioden Grundlagen und Anwendung (German edition), Verlag Technik Berlin. (1976)

[115] R. L-Y. Sah, R. N. Noyce, and W. Shockley, *Carrier Generation and Recombination in P-N Junctions and P-N Junction Characteristics*, P. IRE , **45** (1957) 1228-1243. DOI: 10.1109/JRPROC.1957.278528

[116] R. T. Paynter, *Introductory Electronic Devices and Circuits*, Pearson Education, 7th Edition, chapter 5 (2005).

[117] H. D. Young, and R. A. Freedman, University Physics, 10th edition, Addison-Wesley publishing company (1999).

[118] J. H. Werner, *Schottky Barrier and pn-Junction I/V plots - Small Signal Evaluation*, Appl. Phys. A **47** (1988) 291-300. DOI: 10.1007/BF00615935

[119] C. R. Crowell, *A simplified self-consistent model for image force and interface charge in Schottky barriers*, J. Vac. Sci. Technol. **11** (1974) 951-957. DOI: 10.1116/1.1318712

[120] V.L. Rideout, and C.R. Crowell, *Effects of image force and tunneling on current transport in metal-semiconductor (Schottky barrier) contacts*, Solid-State. Electron. **13** (1970) 993–1009. DOI: 10.1016/0038-1101(70)90097-3

[121] C.R. Crowell, and S.M. Sze, *Current transport in metal-semiconductor barriers*, Solid-State. Electron. **9** (1966) 1035-1048. DOI: 10.1016/0038-1101(66)90127-4

[122] F.A. Padovani, and R. Stratton, *Field and thermionic-field emission in Schottky barriers*, Solid-State. Electron. **9** (1966) 695–707. DOI: 10.1016/0038-1101(66)90097-9

[123] J. H. Werner, and H. H. Güttler, *Barrier inhomogeneities at Schottky contacts*, J. Appl. Phys **69** (1991) 1522-1533. DOI: 10.1063/1.347243

[124] Ş. Altındal, İ. Yücedağ, and A. Tataroğlu, *Analysis of surface states and series resistance in Au/n-Si Schottky diodes with insulator layer using current–voltage and admittance–voltage characteristics*, Vacuum **84** (2010) 363-368. DOI: 10.1016/j.vacuum.2009.07.003

[125] M. E. Aydin, K. Akkiliç, and T. Kiliçoğlu, *The importance of the series resistance in calculating the characteristic parameters of the Schottky contacts*, Appl. Surf. Sci. **253** (2006) 1304-1309. DOI: 10.1016/j.apsusc.2006.02.001

[126] K. Mohanata, and A. J. Pal, *Diode Junctions in Single ZnO Nanowires as Half-Wave Rectifiers*, J. Phys. Chem. C **113** (2009) 18047-18052. DOI: 10.1021/jp906161w

[127] D. M. Taylor, and H. L. Holmes, *Electrical characterization of the rectifying contact between aluminium and electrodeposited poly(3-methylthiophene)*, J. Phys. D **28** (1995) 2554-2568. DOI: 10.1088/0022-3727/28/12/025

[128] Z. Ahmad, and H. Sayyad, *Extraction of electronic parameters of Schottky diode based on an organic semiconductor methyl-red*, Physica E **41** (2009) 631-634. DOI: 10.1016/j.physe.2008.08.068

[129] F. Wahab, M.H. Sayyad, D. N. Khan, M. Tahir, F. Aziz, M. Shahid, M. A. Munawar, and J. A. Chaudry, *Electrical characterization of cobalt phthalocyanine/p-silicon heterojunction*, Mat. Sci. Semicon. Proc. **26** (2014) 101-106. DOI: 10.1016/j.mssp.2014.04.014

[130] S. K. Cheung, and N. W. Cheung, *Extraction of Schottky diode parameters from forward current-voltage characteristics*, Appl. Phys. Lett. **49** (1986) 85-87. DOI: 10.1063/1.97359

[131] C. Herring, and M. H. Nichols, *Thermionic Emission*, Rev. Mod. Phys. **21** (1949) 185-271. DOI: 10.1103/RevModPhys.21.185

[132] H. Norde, *A modified forward I-V plot for Schottky diodes with high series resistance*, J. Appl. Phys. **50** (1979) 5052-5053. DOI: 10.1063/1.325607

[133] V. Aubry, and F. Meyer, *Schottky diodes with high series resistance: Linitation of forward I-V methods*, J. Appl. Phys. **76** (1994) 7973-7984. DOI: 10.1063/1.357909

[134] H. H. Wieder, *Surface fermi level of III-V compound semiconductor-dielectric interfaces*, Surface Science **132** (1983) 390-405. DOI: 10.1016/0039-6028(83)90549-6

[135] J. L. Freeouf, and J. M. Woodall, *Schottky barriers: An effective work function model*, Appl. Phys. Let. **39** (1981) 727-729. DOI: 10.1063/1.92863

[136] R. T. Tung, *Chemical Bonding and Fermi Level Pinning at Metal-Semiconductor Interfaces*, Phys. Rev. Lett. **84** (2000) 6078-6081. DOI: 10.1103/PhysRevLett.84.6078

[137] J. Tersoff, *Theory of semiconductor heterojunctions: The role of quantum dipoles*, Phys. Rev. B, **30** (1984) 4874-4877. DOI: 10.1103/PhysRevB.30.4874

[138] S. G. Louie, and M. L. Cohen, *Electronic structure of a metal-semiconductor interface*, Phys. Rev. B, **13** (1976) 2461-2469. DOI: 10.1103/PhysRevB.13.2461

[139] J. Sturm, C. C. Wu, D. Marcy, and T. R. Hebner, *Fabrication of organic semiconductor devices using ink jet printing*, US Patent 6,087,196 (2000) Google patents accessed 2013-12-10

[140] T. N. Jackson, *Organic Semiconductors: Beyond Moore's Law*, Nat. Mat. **4** (2005) 581-582. DOI: 10.1038/nmat1444

[141] D. Kim, Y. Jeong, C. Y. Koo, K. Song, and J. Moon, *Thin Film Transistors with Ink-Jet Printed Amorphous Oxide Semiconductors*, Jpn. J. Appl. Phys. **49** (2010) 05EB06. DOI: 10.1143/JJAP.49.05EB06

[142] K. Nomura, H. Ohta, K. Ueda, T. Kamiya, M. Hirano, and H. Hosono, *Thin-Film Transistor Fabricated in Single-Crystalline Transparent Oxide Semiconductor*, Science **300** (2003) 1269-1272. DOI: 10.1126/science.1083212

[143] U. Männl, C. van den Berg, B. Magunje, M. Härting, D.T. Britton, S. Jones, M. J. van Staden, and M. R. Scriba, *Nanoparticle composites for printed electronics*, Nanotechnology **25** (2014) 094004. DOI: 10.1088/0957-4484/25/9/094004

[144] H.-W. Lin, C.-P. Chang, W.-H. Hwu, and M.-D. Ger, *The rheological behaviors of screen-printing pastes*, J. Mater. Process. Technol. **197** (2008) 284-291. DOI: 10.1016/j.jmatprotec.2007.06.067

[145] R. Fijan, M. Basile, S. Šostar-Turk, E. Žagar, M. Žigon, and R. Lapasin, *A study of rheological and molecular weight properties of recycled polysaccharides used as thickeners in textile printing*, Carbohyd. Polym. **76** (2009) 8-16. DOI: 10.1016/j.carbpol.2008.09.027

[146] The Gwent Group, U.K http://gwent.org/, accessed 2013-10-07

[147] K.E. MacArthur, T.J. Pennycook, E. Okunishi, A.J. D'Alfonso, N.R. Lugg, L.J. Allen, and P.D. Nellist, *Probe integrated scattering cross sections in the analysis of atomic resolution HAADF STEM images*, Ultramicroscopy **133** (2013) 109-119. DOI: 10.1016/j.ultramic.2013.07.002

[148] NCEM National Center for electron microscopy, http://ncem.lbl.gov/frames/TEAM0.5.htm, accessed 2013-07-02

[149] D. B. Williams, and C. B. Carter, *Transmission Electron Microscopy Part 1: Basics*, Springer Science+Business Media (2009).

[150] U. Dahnen, R. Erni, V. Radmilovic, C. Ksielowski, M.-D. Rossell, and P. Denes, *Background, status and future of the Transmission Electron Aberration-corrected Microscope project*, Phil. Trans. R. Soc. A **367** (2009) 3795-3808. DOI: 10.1098/rsta.2009.0094

[151] S. M. Bruemmer, L. A. Charlot, and B. W. Arey, *Sensitization Development in Austenitic Stainless Steel: Correlation Between STEM-EDS and EPR Measurements*, Corrosion **44** (1998) 328-333. DOI: 10.5006/1.3583945

[152] S. M. Schwarz, B. W. Kempshall, L. A. Giannuzzi, and M. R. McCartney, *Avoiding the Curtaining Effect: Backside Milling by FIB INLO*, Microcs. Microanal. **9** (2003) 116-117. DOI: 10.1017/S1431927603441044

[153] R. Hillenbrand, *Nahfeldoptische Amplituden- und Phasenkontrastmikroskopie zur nanoskopischen Abbildung von Materialkontrast und optisch resonanten Partikeln*, Ph.D. thesis, technical university Munich (2001).

[154] E. H. Synge, *XXXVIII. Suggested method for extending microscopic resolution into the ultramicroscopic region*, Philosophical Magazine Series 7, **6** (1928) 356-362. DOI: 10.1080/14786440808564615

[155] D. W. Pohl, S. Denk, and M. Lanz, *Optical stethoscopy: Image recording with resolution* $\lambda/20$, App. Phys. Lett. **44** (1984) 651-653. DOI: 10.1063/1.94865

[156] A. Lewis, M. Isaacson, A. Harootunian, and A. Muray, *Development of a 500* Å *spatial resolution light microscope: I. light is efficiently transmitted through* $\lambda/16$ *diameter apertures*, Ultramicroscopy **13** (1984) 227-232. DOI: 10.1016/0304-3991(84)90201-8

[157] J. Wessel, *Surface-enhanced optical microscopy*, J. Opt. Soc. Am. B **2** (1985) 1538-1541. DOI: 10.1364/JOSAB.2.001538

[158] A. Huber, *Nanoscale surface-polariton spectroscopy by mid- and far-infrared near-field microscopy*, Selected Topics of Semiconductor Physics and Technology, Ph.D. thesis, technical university Munich (2010).

[159] D. J. Griffith, *Introduction to electrodynamics*, Prentice Hall 3rd edition (1999).

[160] L. Novotny and B. Hecht, Principles of Nano-Optics, Cambridge University Press; 2nd edition (2012).

[161] T. Taubner, *Infrarotspektroskopie im Nahfeld einer Tastspitze*, Ph.D. thesis, technical university Munich (2005).

[162] A. A. Tseng, *Recent developments in nanofabrication using scanning near-field optical microscope lithography*, Opt. Laser Technol. **39** (2007) 514-526. DOI: 10.1016/j.optlastec.2005.11.002

[163] B. Knoll, and F. Keilmann, *Electromagnetic field in the cut-off reginme of tapered metallic waveguides*, Opt. Commun. **162** (1999) 177-181. DOI: 10.1016/S0030-4018(99)00094-2

[164] T. Taubner, R. Hillenbrand, and F. Keilmann, *Performance of visible and midinfrared scattering-type near field optical microscopes*, J. Microsc. **210** (2003) 311-314. DOI: 10.1046/j.1365-2818.2003.01164.x

[165] B. Knoll, and F. Keilmann, *Near-field probing of vibrational absorption for chemical microscopy*, Nature **399** (1999) 134-137. DOI: 10.1038/20154

[166] F. Zenhauser, Y. Martin, and H. K. Wickramasinghe, *Scanning interferometric apertureless microscopy: optical imaging at 10* Å *resolution*, Science **269** (1995) 1083-1085. DOI: 10.1126/science.269.5227.1083

[167] R. Hillenbrand, and F. Keilmann, *Material-specific mapping of metal / semiconductor / dielectric nanosystems at 10nm resolution by back-scattering near-field optical microscopy*, App. Phys. Let. **80** (2002) 25-27. DOI: 10.1063/1.1428767

[168] A. J. Huber, A. Ziegler, T. Köck, and R. Hillenbrand, *Infrared nanoscopy of strained semiconductors*, Nat. Nanotechnol. **4** (2009) 153-157 DOI: 10.1038/NNANO.2008.399

[169] F. Keilmann, and R. Hillenbrand, *Near-field microscopy by elastic light scattering from a tip*, Phil. Trans. R Soc. London A **362** (2004) 787-805. DOI: 10.1098/rsta.2003.1347

[170] A. Cvitkovic, N. Ocelic, and R. Hillenbrand, *Analytical model for quantitative prediction of materials contrasts in scattering-type near-field optical microscopy*, Opt. Exp. **15** (2007) 8550-8565. DOI: 10.1364/OE.15.008550

[171] N. Ocelic, *Quantitative near-field phonon-polariton spectroscopy*, Ph.D. thesis, Technical University Munich (2007).

[172] K. Kneipp, H. Kneipp, I. Itzkan, R. R. Dasari, and M. S. Feld, *Ultrasensitive Chemical Analysis by Raman Spectroscopy*, Chem. Rev. **99** (1999) 2957-2975. DOI: 10.1021/cr980133r

[173] E. F. Pettersen, T. D. Goddard, C. C. Huang, G. S. Couch, D. M. Greenblatt, E. C. Meng, and T. E. Ferrin, *UCSF Chimera–a visualization system for exploratory research and analysis*, J. Comput. Chem. **25** (2004) 1605-1612. DOI: 10.1002/jcc.20084

[174] M. F. Sanner, A. J. Olson, and J.-C. Spehner, *Reduced surface: An efficient way to compute molecular surfaces*, Biopolymers **38** (1996) 305–320. DOI: 10.1002/(SICI)1097-0282(199603)38:3<305::AID-BIP4>3.0.CO;2-Y

[175] A. P. Alivisatos, *Semiconductor Clusters, Nanocrystals, and Quantum Dots*, Science **271** (1996) 933-937. DOI: 10.1126/science.271.5251.933

[176] T.-Y. Kim, N.-M. Park, K.-H. Kim, G. Y. Sung, Y.-W. Ok, T.-Y. Seong, and C.-J. Choi, *Quantum confinement effect of silicon nanocrystals in situ grown in silicon nitride films*, Appl. Phys. Lett. **85** (2004) 5355-5357. DOI: 10.1063/1.1814429

[177] R. Erni, M. D. Rossell, C. Kisielowski, and U. Dahmen, *Atomic-Resolution Imaging with a Sub-50-pm Electron Probe*, Phy. Rev. Lett. **102** (2009) 096101. DOI: 10.1103/PhysRevLett.102.096101

[178] C. Kisielowski, B. Freitag, M. Bischoff, H. van Lin, S. Lazar, G. Knippels, P. Tiemeijer, M. van der Stam, S. von Harrach, M. Stekelenburg, M. Haider, S. Uhlemann, H. Müller, P. Hartel, B. Kabius, D. Miller, I. Petrov, E.A. Olson, T. Donchev, E.A. Kenik, A.R. Lupini, J. Bentley, S.J. Pennycook, I.M. Anderson, A.M. Minor, A.K. Schmid, T. Duden, V. Radmilovic, Q.M. Ramasse, M. Watanabe, R. Erni, E.A. Stach, P. Denes, and U. Dahmen, *Detection of Single Atoms and Buried Defects in Three Dimensions by Aberration-Corrected Electron Microscope with 0.5-Å Information Limit*, Microsc. Microanal. **14** (2008) 469-477. DOI: 10.1017/S1431927608080902

[179] K. Hirose, H. Nohira, K. Azuma, and T. Hattori, *Photoelectron spectroscopy studies of SiO_2/Si interfaces*, Prog. Surf. Sci **82** (2007) 3-54. DOI: 10.1016/j.progsurf.2006.10.001

[180] F. L. Galeener, and J. C. Mikkelsen Jr., *Vibrational dynamics in ^{18}O-substituted vitreous SiO_2*, Phys. Rev. B **23** (1981) 5527-5530. DOI: 10.1103/PhysRevB.23.5527

[181] C. Meier, S. Lüttjohann, V. G. Kravets, H. Nienhaus, A. Lorke, and H. Wiggers, *Raman properties of silicon nanoparticles*, Physica E **32** (2006) 155-158. DOI: 10.1016/j.physe.2005.12.030

[182] J. E. Smith, Jr., M. H. Brodsky, B. L. Crowder, M. I. Nathan, and A. Pinczuk, *Raman Spectra of Amorphous Si and Related Tetrahedrally Bonded Semiconductors*, Phys. Rev. Lett. **26** (1971) 642-646. DOI: 10.1103/PhysRevLett.26.642

[183] R. Alben, J. E. Smith, Jr., M. H. Brodsky, and D. Weaire, *Theory of Infrared and Raman Spectra of Amorphous Si and Ge*, Phys. Rev. Lett. **30** (1973) 1141–1144. DOI: 10.1103/PhysRevLett.30.1141

[184] A. Huber, D. Kazantsev, F. Keilmann, J. Wittborn, and R. Hillenbrand, *Simultaneous infrared material recognition and conductivity mapping by nanoscale near-field microscopy*, Adv. Mater. **19** (2007) 2209–2212. DOI: 10.1002/adma.200602303

[185] R. F. Schmitsdorf, T.U. Kampen, and W. Mönch, *Correlation between barrier height and interface structure of View the Ag/Si (111) source Schottky diodes*, Surf. Sci. **324** (1995) 249-256. DOI: 10.1016/0039-6028(94)00791-8

[186] F. Guinea, J. Sachez-Dehesa, and F. Flores, *Schottky barrier formation. I. Abrupt metal-semiconductor junctions*, J. Phys. C: Solid State Phys., **16** (1983) 6499-6512. DOI: 10.1088/0022-3719/16/33/021

[187] P. Chattopadhyay, *Effect of localized states on the current-voltage characteristics of metal-semiconductor contacts with thin interfacial layer*, Solid-State Electron. **37** (1994) 1759-1762. DOI: 10.1016/0038-1101(94)90223-2

[188] J. M. Shannon, *Control of Schottky barrier height using highly doped surface layers*, Solid-State Electron. **19** (1976) 537-543. DOI: 10.1016/0038-1101(76)90019-8

[189] A. Odo, *Synthesis, Characterisation and Device Application of Silicon Nanoparticles produced by Mechanical Attrition*, Ph.D. thesis, University of Cape Town (2009).

[190] G. G. Gonfa, *Hall Effect in Printed Nanoparticulate Silicon Networks*, Ph.D. thesis, University of Cape Town (2009).